MICROWAVE REMOTE SENSING TECHNIQUES FOR VAPOR, LIQUID AND ICE PARAMETERS

by

Li Li

A dissertation submitted in partial fulfillment
of the requirements for the degree of

Doctor of Philosophy

University of Washington

1995

Approved by _____
(Chairperson of Supervisory Committee)

_____

_____

Program Authorized
to Offer Degree ELECTRICAL ENGINEERING

Date 5/31/95

In presenting this dissertation in partial fulfillment of the requirements for the Doctoral degree at the University of Washington, I agree that the Library shall make its copies freely available for inspection. I further agree that extensive copying of this dissertation is allowable only for scholarly purposes, consistent with "fair use" as prescribed in the U.S. Copyright Law. Requests for copying or reproduction of this dissertation may be referred to University Microfilms, 1490 Eisenhower Place, P.O. Box 975, Ann Arbor, Michigan 48106, to whom the author has granted "the right to reproduce and sell (a) copies of the manuscript in microform and/or (b) printed copies of the manuscript made from microform."

Signature 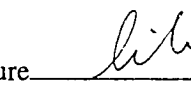

Date May 3, 1995

University of Washington

Abstract

MICROWAVE REMOTE SENSING TECHNIQUES FOR VAPOR, LIQUID AND ICE PARAMETERS

by *Li Li*

Chairperson of Supervisory Committee: Professor Chi H. Chan
Department of Electrical Engineering

The objective of this dissertation is to develop a comprehensive physical inverse model for microwave remote sensing of atmospheric components. This novel approach provides a rigorous basis for understanding and extracting the physical information content of radiometer and/or radar measurements of the atmospheric media. To this end, a comprehensive parametric radiative transfer model (forward model) is developed first to simulate microwave and millimeter-wave radiation of atmosphere as a function of vertical distributions of water vapor, oxygen, liquid and ice clouds. Radiosonde data and NOAA ground-based radiometer observations were used to calibrate and validate this model.

This forward model is then used to examine the sensitivity of downwelling microwave radiation to realistic variations of environments and to evaluate the information content carried in the ground-based radiometer observations. Based on these studies, a physical inversion approach is designed using Artificial Neural Network (ANN) inversion techniques. Both explicit and iterative inverse methods are used to study the non-uniqueness and non-convexness of the inversion on synthetic data. For real data analysis, this physical inverse approach is applied to model NOAA's two- and three-channel ground-based radiometers (20.6, 31.65 and 90 GHz). The new physical inverse model is able to retrieve vertically integrated water vapor, cloud liquid water and ice water content simultaneously. Excellent model validations on water vapor and liquid water path retrievals were obtained based on radiosonde observations and NOAA's operational statistical models.

A combined iterative radar/radiometer method is further developed to vertically profile cloud microphysics by examining the relationship between radar reflectivity and cloud

microphysics. The combined model use retrievals from radiometer as initial guess and search iteratively for desired microphysical profiles which are consistent with radar measurements. Case studies of liquid clouds found that this radar/radiometer technique agrees very well with aircraft in situ measurement of liquid drop size spectra. It was also found that the combined method agrees reasonablely well with other published studies on empirical relationships between radar reflectivity and ice or liquid cloud parameters.

The predominant feature of a physical inverse model developed in this dissertation is that it can easily handle the non-linearity of radiative transfer and address the non-uniqueness of inversion. Besides, the physical model does not depend on in situ measurements and is thus site-independent. In principle, different remote sensor observations and climatological statistics can be incorporated into the inversion model.

TABLE OF CONTENTS

LIST OF FIGURES

LIST OF TABLES

ACKNOWLEDGMENTS

I would like to express my gratitude to Drs. Chi Chan, Leung Tsang, Jothiram Vivekanandan, Conway Leovy, Jeng-Neng Hwang and Akira Ishimaru, not only for serve my committee and their assistance on the completion of this research, but also for their help to define the standard of excellence against which I will always measure my own work. I am especially indebted to Drs. Chi Chan and Leung Tsang, for their teaching, support and encouragement, their scientific counsel and friendship. I am also indebted to Dr. Jothiram Viveknandan, my supervisor at the National Center for Atmospheric Research(NCAR), for his guidance, support and encouragement throughout the course of the research.

Dr. Marcia Politovich of NCAR should be recoginzed for her organizing the validation of combined radar/radiometer method using aircraft in situ measurements, and for providing me with the results of aircraft data analysis. She also deserves my deep appreciation for her counsel on cloud microphysics.

Many other scientists from outside the University of Washington provided invaluable discussion and/or assistance. Of these, I particularly wish to thank Drs. Ed R. Westwater, Yong Han and Jack Snider from NOAA/ETL, and Drs. Roy Rasmussen, Wayne Adams and Zhongqi Jing from NCAR. Dr. M. Spencer provided the quality controlled NOAA radiometer data. Drs. R. Reinking and R. Kropfli provided the NOAA K-band radar data.

I would like to thank Mr. Dan Davis, a fellow graduate student, for making his Neural Network package available to me and for his valuable assistance in its use. Special thanks go to my friends Phillip Phu, Kyung Pak, Zhengxiao Chen, Shu-hsiang Lou, Bob Kipp, Todd Elson, Charlie Le, Chuck Mandt and Chi Ming Lam for their valuable discussions and assistance. Above all, I am especially indebted to my cousin, Kent T-Y Wong, M.D., who has always been an unfailing source of trust and support. I am indebted to my parents, Yichun Huang and

Benmao Li, and my uncle, Richard T-S Wong, for their support and sacrifices to further my education. I am also indebted to my wife, Shaoqin Liang, for her loving care, understanding, and encouragement, which provided me with the strength and motivation to go the distance.

This research is sponsored in part by the *National Science Foundation* through an Interagency Agreement in response to requirements and funding by the *Federal Aviation Administration*'s Aviation Weather Development Program. The views expressed are those of the authors and do not necessarily represent the official policy or position of the U.S. Government.

DEDICATION

To my cousin, Kent T-Y Wong, M.D., for teaching me the value of an education and providing the support to pursue one.

Chapter 1

INTRODUCTION

1.1 Microwave remote sensing and atmospheric media

With the advent of microwave and millimeter wave radiometers, passive remote sensing of clouds and precipitation has become an indispensable tool in a variety of applications such as global climate change, meteorological and oceanographic studies. Radiometers are widely used in a number of major field experiments such as the Tropical Ocean-Global Atmosphere (TOGA) and Tropical Rainfall Measuring Mission (TRMM). Unlike infrared and optical remote sensing, Microwave radiation can penetrate precipitation system and responds directly to physical entities such as water vapor, cloud liquid water and ice particles. Kummerow [28] has also demonstrated that microwave radiometer alone can provide some information about the precipitation structures.

Quantitative retrieval of water vapor, liquid water, ice water and structures of cloud and precipitation is important to studies such as the earth's radiation budget, latent heating distribution, and microphysical processes of winter and summer clouds. As an example, latent heat distribution has the potential of modifying the immediate environment, global circulation and atmospheric stability [29]. Recent studies also found that precipitation patterns of tropical hurricane structure is related to the hurricane development in terms of intensification and decay. A reliable rainfall retrieval algorithm, if it can be developed, will surely be helpful in the accurate forecasting of the track and intensities of hurricanes [78].

Emission and scattering characteristics of hydrometeors depend on frequency. Thus, a multifrequency radiometer has the capability of profiling cloud microphysics. In addition to frequency characteristics, the non-spherical nature of hydrometeors also gives rise to polarized brightness temperature. Hence a combination of the multi-frequency and multi-polarization radiometer technique promises improved understanding of cloud microphysics. A better understanding of cloud microphysics leads to accurate quantification of ice and liquid water path.

Raindrops, cloud liquid droplets and melting ice are the major source of radiation. Also, the emission from background such as land and ocean surfaces plays a major role at lower frequencies. At higher frequencies(above 85GHz), the scattering due to ice in cloud marks the effects due to land and ocean surfaces and reduces the upwelling brightness temperatures. Thus emission and scattering phenomena correspond to liquid and ice phase respectively.

Radiation field emerging from cloud systems represents scattering and extinction of emitted radiation through the regions of liquid and frozen hydrometeors. Scattering, emission and extinction characteristics depend on microphysics of hydrometeors such as, size, shape, orientation and composition(dielectric constant). Hydrometors microphysics depend on cloud type, geographical location and time of the year.

For the purpose of microwave remote sensing, hydrometeors can be classified into a few distinct categories [12]:

1. Small liquid droplets of radius less than $50\mu m$, typical of nonprecipitating cumulus and stratus clouds, fog and haze [47].

2. Liquid precipitation, of radius between $50\mu m - 5mm$. Due to viscous forces, these hydrometeors are slightly oblate in shape. Few sizes greater than 1mm.

3. Frozen particles of dimension less than ~1mm. These particles in cirrus, anvil clouds such as needles, plates, or dendrite fall in their winter category.

4. Frozen particles (snow, hail or graupel) of size between 1mm and 10mm. These hydrometeors generally consist of a combination of ice phase and entrained regions of air.

Among different hydrometeors, liquid droplets exhibit strong emission characteristics at microwave frequencies. On the contrary, frozen hydrometeors such as ice crystals are characterized by albedo close to unity with very little emission. In the case of non-spherical hydrometeors, the emerging radiation might be polarized due to scattering and emission process. However, cloud droplets provide plentiful unpolarized radiation, thereby reducing any polarization difference in brightness temperatures.

Most of the hydrometeors are nonspherical dielectric particles. Different methods have been used to study their scattering and absorption behavior for the electromagnetic

waves. Such methods include T-Matrix method [65] [72], integral equation method [62] and Digitized Green's function method (DGF) [13]. Because DGF can be used to calculate the scattering by dielectric particles of arbitrary shape and arbitrary optical structure, it is widely used in the modeling of microwave radiative transfer in winter clouds.

1.2 A review of forward and inverse models

The main objective of passive microwave remote sensing is to extract microphysical information. Depending on the frequency of operation and radiation characteristics of the atmosphere, various techniques are used to infer microphysical information using radiometer measurements. In principle, the development of retrieval algorithms consists of several phases. First phase is the construction of cloud models which incpoporate reliable assumptions about atmospheric and cloud structures relevant to the radiative transfer model. Cloud models are always problem-dependent due to high spatial variability of clouds. The second phase is to study the quantitative response of microwave emission and scattering characteristics to changes in the cloud microphysics or the scene being observed by the remote sensor. This is known as the forward radiative transfer problem. Finally, a retrieval (or inverse) algorithm is developed based on the simulations and observations of the forward problem.

There are basically three approaches to developing forward radiative transfer models: the iterative method, the discrete ordinate-eigenanalysis method, and the invariant imbedding method [65] [24]. The iterative method gives a closed form solution and physical interpretation of emission and scattering processes; but it can be used only for situations where emission is dominant or cloud optical depth is thin. The discrete ordinate-eigenanalysis and invariant imbedding techniques are mathematically rigorous and can be used for a general albedo and optical depths, which invoive multiple scattering. The discrete ordinate-eigenanalysis method is applicable for homogeneous temperature profiles. For media with inhomogeneous temperature profiles, the invariant imbedding method is appropriate. All three approaches are applied extensively in both active and passive microwave remote sensing areas. For passive sensing of atmosphere, it is important to deal with vertical profiles of atmospheric media, and perhaps nonspherical shapes of hydrometeors. We refer to radiative transfer models which deal with vertical profiles of atmosphere as a comprehensive forward model.

Existing quantitative precipitation retrieval algorithms for passive microwave remote

sensing can be divided into two basic categories: statistical and physical algorithms. The majority of the statistical algorithms are based on linear (or multilinear) statistical regression of brightness temperatures against "in-situ" observations or forward model simulations of variables to be retrieved. This approach is optimal only for linear problems. However, there are non-linearities in both the forward physical models and in the statistical relationships between various environmental parameters. To deal with the nonlinearities, some of the algorithms have been used to include quadratic terms or a piecewise scheme, but no satisfactory improvement has been obtained so far.

Physical algorithms attempt to retrieve microphysics in a 'rigorous' way. The majority of the physical algorithms are based on more or less oversimplified forward models, which represent the relationship between brightness temperatures and environmental variables. Physical algorithms seek to invert microphysical quantities mathematically using a set of algebraic expressions which relate to brightness temperatures. It is obvious that the physical model is optimal only if the forward model is accurate and the inversion is unique (explicit inversion). In the event that the forward model depends on more independent variables than the number of measurements, the explicit inversion will suffer the many-to-one mapping. In such a case, iterative inversion is usually used with additional constraints such as statistical information; e.g., climatological statistics. Iterative inversion might avoid many-to-one mapping but it does not guarantee convergence to the right solution even with additional constraints.

Physical and statistical algorithms solve inverse scattering problems from different perspectives, and none is generally superior over the other. Pure statistical algorithms completely ignore physical insight. Also physical algorithms are not capable of solving the problem in an optimal way.

Recently, there have been an increasing interest in using an artificial neural network to retrieve geophysical information from passive microwave remote sensing measurements [6] [61] [23]. Neural networks can handle the non-linearity inhibited in remote sensing problems. It is also relatively easier for neural networks to incorporate auxiliary information into retrieval algorithms. To find an accurate and comprehensive retrieval algorithm, which is obviously very desirable, we applied an approach that combines comprehensive forward emission and scattering algorithms with neural network inversion techniques. In the following chapters, we first outline the solutions to the radiative transfer process, and then describe a procedure of developing a comprehensive physical inverse model for passvie

remote sensing of atmospheric components, especially for detection and estimation of supercooled water and aircraft icing forecasting in winter clouds.

1.3 WISP and combined remote sensor techniques

The Wintet Icing and Storms Project (WISP) is an ongoing study to improve the forecasting of icing conditions for the aviation community [49]. The major objectives of the experiment are detection, estimation and forecasting of supercooled liquid water (SLW). The existence of SLW in winter clouds is known to cause icing hazards to aircraft. Icing is defined as the accretion of SLW droplets onto aircraft surfaces, and it continues to be one of the primary causes of aviation accidents, especially in winter weather situations. The problem of icing detection is that of identification of SLW in environments favorable for icing. SLW forms during lifting where the ambient air temperatures are below 0°C [46].

Several techniques have been proposed for the detection of SLW. Direct remote detection of SLW is almost impossible using conventional S-, C-, X- and K-band radar due to a negligible backscattering cross section of cloud droplets (diameters less than 35 microns). Furthermore, co-existence of SLW with ice leads to masking by ice scattering. Microwave radiometers can remotely estimate the path-integrated SLW, but cannot by themselves provide spatial distribution. Dual-wavelength radar techniques (X- and K-band) may be able to estimate spatial distribution of attenuation which is proportional to SLW.

Combined modeling of multiparameter radar and microwave radiometer signals from precipitating clouds has been investigated to enhance microphysical retrieval using radiometer observations [11]. Microphysical parameters, such as vertical structure, shape, orientation, number concentration and bulk density are important for both multiparameter radar and passive microwave radiometry. Using the vertical structure and type of ice hydrometeors obtained from multiparameter radar, one can reduce the uncertainty in microphysical input to microwave radiative transfer models, hence the number of assumptions for retrieval relationships. As an example, in analysis of data from COHMEX experiment, single-scattering properties of each 0.5-km-thick layer were estimated from CP-2 multiparameter radar measurements for subsequent input into a radiative transfer model [71]. Because of the sensitivity of scattering to the change in frequency, brightness temperatures at different frequencies are studied and compared. Correlations were found between liquid water path and brightness temperatures at lower frequency, 18GHz; and ice

optical thinkness and brightness temperature at high frequency, 85GHz. It was also noted that brightness temperature 37-85GHz T_b depends essentially on the ice optical thinkness or ice water path if the effect of cloud liquid water is excluded.

Combined sensor techniques have also been developed and tested on winter storms to retrieve water vapor and liquid profile [58]. In this method, a number of sensors are used to provide information on cloud and thermodynamic conditions. For example, liquid water content measurements by research aircraft are averaged to get a "simple" liquid water profile shape. A temperature profile is obtained from Radio Acoustic Sounding System (RASS); the cloud height is detected by a ceilometer and the total liquid and vapor path are measured by radiometer. All these measurements are used to generate "first-guess" profiles for the radiative transfer model to calculate brightness temperatures. If the calculated brightness temperatures do not agree with measured ones within 2 K, the water vapor profile is tuned until the computed and measured brightness temperatures agree. Therefore, this technique vertically distributes the total cloud liquid path measurements of the radiometer. Although the experimental results are "encouraging", a number of key issues are not taken into account. First, is the retrieved profile a unique solution? If not, how far is it from the true solution? Second, linear statistical retrieval algorithms of ground-based radiometry breaks down in the presence of scattering. One objective of this research is to improve and enhance the multifrequency radiometer retrieval techniques of vapor, ice and cloud water using a neural network based approach. These techniques are applicable to ground-based and space borne instruments

1.4 Research objective

The major objective of this dissertation is to develop a comprehensive physical inverse model for microwave remote sensing of atmospheric components. This novel approach provides a rigorous basis for understanding and extracting the physical information content of radiometer and/or radar measurements of the atmospheric media. In chapter 2, the solutions of vector radiative transfer equation are derived using first-order iterative method, discrete ordinate-eigenanalysis method and invariant imbedding method. The validity of the solution is obtained by comparing three different method against each other, and against perviously published results.

Chapter 3 apply the solutions of radiative transfer in chapter 2 to the modeling of ground-based radiometer. a comprehensive parametric radiative transfer model (forward model)

is developed first to simulate microwave and millimeter-wave radiation of atmosphere as a function of vertical distributions of water vapor, oxygen, liquid and ice clouds. Radiosonde data and NOAA ground-based radiometer observations were used to calibrate and validate this model. This forward model is then used to examine the sensitivity of downwelling microwave radiation to realistic variations of environments and to evaluate the information content carried in the ground-based radiometer observations. Based on these studies, a physical inversion approach is designed using Artificial Neural Network (ANN) inversion techniques. Both explicit and iterative inverse methods are used to study the non-uniqueness and non-convexness of the inversion on synthetic data. For real data analysis, this physical inverse approach is applied to model NOAA's two- and three-channel ground-based radiometers (20.6, 31.65 and 90 GHz). The new physical inverse model is able to retrieve vertically integrated water vapor, cloud liquid water and ice water content simultaneously. Excellent model validations on water vapor and liquid water path retrievals were obtained based on radiosonde observations and NOAA's operational statistical models.

A combined iterative radar/radiometer method is further developed in Chapter 4 by examining the relationship between radar reflectivity and cloud microphysics. The combined model use retrievals from radiometer as initial guess and search iteratively for desired microphysical profiles which are consistent with radar measurements. Case studies of liquid clouds found that this radar/radiometer technique agrees very well with aircraft in situ measurement of liquid drop size spectra. It was also found that the combined method agree reasonablely well with other published studies on empirical relationships between radar reflectivity and ice or liquid cloud parameters.

The predominant feature of a physical inverse model developed in this dissertation is that it can easily handle the non-linearity of radiative transfer and address the non-uniqueness of inversion. Besides, the physical model does not depend on in situ measurements and is thus site-independent. In principle, different remote sensor observations and climatological statistics can be incorporated into the inversion model.

Chapter 2

THE SOLUTION OF VECTOR RADIATIVE TRANSFER THEORY

2.1 Theoretical Model Developments

The microwave emissivity and scattering of atmospheric media are in general polarization dependent, thus there can be a major difference between the vertical polarized emission and horizontal polarized emission resulting in distinct different brightness temperatures (T_B). The vertically and horizontally polarized T_B are the first two parameters in modified Stokes vector. The third and fourth Stokes parameters represent the real and imaginary components of correlation between first two Stokes parameters. All four stokes parameters can be measured to obtain complete polarimetric information of the emitted radiation. Unlike in active remote sensing, the third(U) and fourth(V) Stokes parameters have usually been neglected in passive remote sensing of atmosphere. However, it has been reported that they could be nonzero under some situations [66] [32]. In this report, we will study all four Stokes parameters based on the vector radiative transfer theory. U and V parameter values are zero in the case of azimuthal symmetry in radiative transfer formulation. We model the winter cloud as a single or multiple layers, of liquid water droplets and ice particles over ocean or land surfaces.

Three techniques will be used to solve the radiative transfer equations: the iterative method, the discrete ordinate-eigenanalysis method and the method of invariant imbedding. The iterative method gives a closed form solution and physical insight into the emission and scattering processes, but it can be used only for cases of small albedo, i.e., scattering is dominated by absorption. The discrete ordinate-eigenanalysis and invariant imbedding techniques are mathematically rigorous and they can be used for a general albedo and optical depths. Discrete ordinate-eigenanalysis method is applicable only for homogeneous temperature profile. For media with inhomogeneous temperature profiles, the invariant imbedding method is appropriate.

2.1.1 *Iterative Method*

The iterative method is suitable for clouds with thin optical depth or emission domination. Unlike in radar remote sensing where source term is define only in backscattering direction, passive remote sensing consider emission in all directions. Hence it is more difficult to get higher order iterative solutions for passive remote sensing than for active cases. The zero-order solution for spheroids has been studied in [66], but the first-order solution was formulated only for a layer of spheres [65]. To simplify mathematical formulations, all existing iterative methods assume homogeneous temperature (source) profiles.

The first-order iterative solution for arbitrary shaped discrete scatterers is useful in many applications. Except for particles with large albedo, higher order scattering terms usually decay very fast. In this case, the first order solution is very accurate. On the other hand, even for highly scattering ice crystals, if the optical depth of clouds is very small, it is suggested that higher order scattering would also become insignificant [9]. An example is cirrus clouds. In winter cloud, large albedo ice crystals are mixed with small albedo liquid water droplets. Higher order scattering can be investigated by comparing the first-order iterative solution with the full-scattering one. Besides, one important feature of the first-order iterative method is that it is in closed form.

To derive the zero-and first-order solution, let's consider a collection of sparsely distributed nonspherical particles with permittivity ϵ_s and temperature profile $T(z)$ overlying a homogeneous half space of temperature T_2 and permittivity ϵ_2 as shown in Figure 2.1.

The vector radiative transfer equation in region 1 is of the fellowing form [65]

$$\begin{aligned}\cos\theta\frac{d\overline{I}(\theta,z)}{dz} &= -\overline{\overline{K_e}}(\theta)\overline{I}(\theta,z)+\overline{F}(\theta)CT(z)\\ &+ \int_0^{2\pi}d\phi'\int_0^{\pi}d\theta'\sin\theta'\overline{\overline{P}}(\theta,\phi;\theta',\phi')\bullet\overline{I}(\theta',z)\end{aligned}\tag{2.1}$$

Where $\overline{\overline{K_e}}$ is a 4×4 extinction matrix; $\overline{F}(\theta)$ is the emission vector generally with 4 nonzero elements, and $\overline{\overline{P}}(\theta,\phi;\theta',\phi')$ is the 4×4 phase matrix denoting scattering from direction (θ,ϕ) into direction (θ',ϕ').

Theoretically, the temperature profile $T(z)$ can be in any form for the iterative method. In this thesis, we use a linear profile since it is commonly used in cloud modeling. If the physical temperatures are T_0 and T_1 at top and bottom of the cloud, respectively, then $T(z)$ is given by

$$T(z) = az + b \tag{2.2}$$

where $a = \frac{T_0 - T_1}{d}$, $b = T_0$ and d is the physical thickness of the cloud.

We denote the Stokes vector of upwelling radiance as $\overline{I}(\theta, z)$ and downwelling radiance as $\overline{I}(\pi - \theta, z)$ with $0 \leq \theta \leq \frac{\pi}{2}$. Then the boundary conditions can be written in the following form, at $z = 0$

$$\overline{I}(\pi - \theta, \phi, z = 0) = 0 \tag{2.3}$$

and at $z = -d$

$$\overline{I}(\theta, z = -d) = \overline{\overline{R}}(\theta) \bullet \overline{I}(\pi - \theta, z = -d) + \overline{W}(\theta) C T_2 \tag{2.4}$$

where $\overline{\overline{R}}$ is the 4×4 reflectivity matrix and $\overline{W}(\theta)$ is the transmission vector [65],

$$\left(\overline{\overline{R}} \right) = \begin{pmatrix} |R_v(\theta)|^2 & 0 & 0 & 0 \\ 0 & |R_h(\theta)|^2 & 0 & 0 \\ 0 & 0 & Re(R_v(\theta)R_h^*) & -Im(R_v(\theta)R_h^*) \\ 0 & 0 & -Im(R_v(\theta)R_h^*) & Re(R_v(\theta)R_h^*) \end{pmatrix} \tag{2.5}$$

$$\left(\overline{W} \right) = \begin{pmatrix} 1 - |R_v(\theta)|^2 \\ 1 - |R_h(\theta)|^2 \\ 0 \\ 0 \end{pmatrix} \tag{2.6}$$

where $R_v(\theta)$ and $R_h(\theta)$ are reflection coefficients for vertically and horizontally polarized waves.

$$R_v(\theta) = \frac{\epsilon_2 \cos\theta - (\epsilon\epsilon_2 - \epsilon^2 \sin^2\theta)^{\frac{1}{2}}}{\epsilon_2 \cos\theta + (\epsilon\epsilon_2 - \epsilon^2 \sin^2\theta)^{\frac{1}{2}}} \tag{2.7}$$

$$R_h(\theta) = \frac{\epsilon \cos\theta - (\epsilon\epsilon_2 - \epsilon^2 \sin^2\theta)^{\frac{1}{2}}}{\epsilon \cos\theta + (\epsilon\epsilon_2 - \epsilon^2 \sin^2\theta)^{\frac{1}{2}}} \tag{2.8}$$

C is the proportionality constant between radiance and brightness temperature.

The solution of equation(1) can be expressed in terms of eigenvalues and eigenmatrix of the coherent wave propagation,

$$\overline{\overline{E}}(\theta) \bullet \overline{\overline{\beta}}(\theta) = \overline{\overline{K_e}}(\theta) \bullet \overline{\overline{E}}(\theta) \tag{2.9}$$

where $\overline{\overline{\beta}}(\theta)$ is a 4×4 diagonal matrix $\overline{\overline{\beta}} = diag[\beta_i]$, and β_i is the i^{th} eigenvalue of the coherent wave propagation. Matrix $\overline{\overline{E}}$ is the 4×4 corresponding eigenmatrix of extinction matrix [65].

Using eigenvalues and eigenmatrix of the extinction matrix, the solution of equation(1) can be expressed analytically. By matching those solutions with boundary conditions, the complete multiple scattering solution can be written in the following integral equation form, for the upward direction,

$$\begin{aligned}
\overline{I}(\theta, z) &= \overline{\overline{E}}(\theta)\overline{\overline{D}}[-\beta(\theta)(z+d)\sec\theta]\overline{\overline{E}}^{-1}\overline{\overline{R}}(\theta) \\
&\quad \overline{\overline{E}}(\pi-\theta)\overline{\overline{D_1}}(\pi-\theta, d)\overline{\overline{E}}^{-1}(\pi-\theta)\overline{\overline{F}}(\pi-\theta)\sec\theta \\
&+ \overline{\overline{E}}(\theta)\overline{\overline{D}}[-\beta(\theta)(d+z)\sec\theta]\overline{\overline{E}}^{-1}(\theta)\overline{W}(\theta)CT_2 \\
&+ \overline{\overline{E}}(\theta)\overline{\overline{D}}_2(\theta, z, d)\overline{\overline{E}}^{-1}(\theta)\overline{F}(\theta)\sec\theta \\
&+ \overline{\overline{E}}(\theta)\overline{\overline{D}}[-\beta(\theta)(d+z)\sec\theta]\overline{\overline{E}}^{-1}(\theta)\overline{\overline{R}}(\theta)\overline{\overline{E}}(\pi-\theta) \\
&\quad \bullet \int_{-d}^{0} dz'\overline{\overline{D}}[-\beta(\pi-\theta)(z'+d)\sec\theta]\overline{\overline{E}}^{-1}(\pi-\theta) \\
&\quad \bullet \int_{2\pi} d\Omega'[\overline{\overline{P}}(\theta, \phi; \theta', \phi')\overline{I}(\theta', z') + \overline{\overline{P}}(\theta, \phi; \pi-\theta', \phi')\overline{I}(\pi-\theta', z')]\sec\theta \\
&+ \int_{-d}^{z} dz'\overline{\overline{E}}(\theta)\overline{\overline{D}}[\beta(\theta)(z'-z)\sec\theta]\overline{\overline{E}}^{-1}(\theta) \\
&\quad \bullet \int_{2\pi} d\Omega'[\overline{\overline{P}}(\theta, \phi; \theta', \phi')\overline{I}(\theta', z') + \overline{\overline{P}}(\theta, \phi; \pi-\theta', \phi')\overline{I}(\pi-\theta', z')]\sec\theta
\end{aligned} \tag{2.10}$$

where $\overline{\overline{D}} = diag[\exp(\beta_i(\theta)z\sec\theta)]$ is the propagation factor; $\overline{\overline{D}}_1$ and $\overline{\overline{D}}_2$ are nonlinear propagation factors; The expression for diagonal matrices $\overline{\overline{D}}_1$ and $\overline{\overline{D}}_2$ are

$$\begin{aligned}
\overline{\overline{D}}_1(\pi-\theta, d) &= diag[\frac{T_1 - T_0\exp^{-\beta_i(\pi-\theta)d\sec\theta}}{\beta_i(\pi-\theta)\sec\theta} \\
&+ a\frac{1-\exp^{-\beta_i(\pi-\theta)d\sec\theta}}{\beta_i^2(\pi-\theta)\sec^2\theta}]C.
\end{aligned} \tag{2.11}$$

and

$$\overline{\overline{D}}_2(\theta,0,d) = diag[\frac{T_1 - T_0\exp^{-\beta_i(\theta)d\sec\theta}}{\beta_i(\theta)\sec\theta} - a\frac{1-\exp^{-\beta_i(\theta)d\sec\theta}}{\beta_i^2(\theta)\sec^2\theta}]C \quad (2.12)$$

If we neglect the last two integral terms in equation (10), we then get the zero-order solution $\overline{I}^0(\theta,z)$ which is combination of the first three terms in equation(10). The last two terms are scattering related which are perturbations to the zero-order solution for weak scattering problems. It is to be noted that the zero-order solution is emission from ground and cumulative emission from hydrometeors attenuated by both absorption and scattering, so higher order contributions are always positive. As we can see from equation (10), the higher order solution is the zero-order solution plus two scattering terms.

The brightness temperature Stokes vector from the top of atmosphere in direction (θ) is

$$\overline{T}_B(\theta) = \frac{1}{C}\overline{I}(\theta, z=0) \quad (2.13)$$

The three component of zero-order solution $\overline{I}^0(\theta,z)$ can be physically interpreted as follows:

1. Emission from the whole layer(downward emission) reflected by the boundary at $z=-d$, then propagated through the layer.

2. Lower-boundary-emission propagated through the layer.

3. Acumulating upward emission from a layer at and subsequent, then propagation through the rest of the layer.

These three terms are illustrated in Figure 2.2 (a) through (c)

Similarly, we have a complete solution for downward direction,

$$\begin{aligned}\overline{I}(\pi-\theta,z) &= \overline{\overline{E}}(\pi-\theta)\overline{\overline{D_3}}(\pi-\theta,z,d)\overline{\overline{E}}^{-1}(\pi-\theta)\overline{F}(\pi-\theta)\sec\theta \\ &+ \overline{\overline{E}}(\pi-\theta)\int_z^0 dz'\overline{\overline{D}}[\beta(\pi-\theta)(z-z')\sec\theta]\overline{\overline{E}}^{-1}(\pi-\theta) \\ &\bullet \int_{2\pi} d\Omega'[\overline{\overline{P}}(\pi-\theta,\phi;\theta',\phi')\overline{I}(\theta',z') + \overline{\overline{P}}(\pi-\theta,\phi;\pi-\theta',\phi')\overline{I}(\pi-\theta',z')] \quad (2.14)\end{aligned}$$

The zero-order solution for downward going Stokes $\overline{I}^0(\pi-\theta,z)$ is given by the first terms in equation (14) and illustrated in Figure 2.2 (f).

The first-order solution can be obtained by iterating the zero-order solution $\overline{I}^0(\theta,z)$ and $\overline{I}^0(\pi-\theta,z)$ in equation(10) and using Gaussian Quadrature integral formula. The resulting first-order solution is,

$$\begin{aligned}\overline{I}^{(1)}(\theta,0) &= \overline{I}^{(0)}(\theta,0)\\ &+ \overline{\overline{E}}(\theta)\overline{\overline{D}}[-\beta(\theta)d\sec\theta]\overline{\overline{E}}^{-1}(\theta)\overline{\overline{R}}(\theta)\overline{\overline{E}}(\pi-\theta)\\ &\quad \overline{\overline{D}}[-\beta(\pi-\theta,)d\sec\theta]\overline{N_1}^{(1)}\sec\theta\\ &+ \overline{\overline{E}}(\theta)\overline{N_2}^{(1)}\sec\theta \qquad (2.15)\end{aligned}$$

where

$$\begin{aligned}\overline{N_1}^{(1)} &= 2\pi\sum_{j=1}^{N} a_j[\overline{\overline{Q_{21}(-\mu,\mu_j)H_1(-\mu,\mu_j)}}\overline{L}(\mu_j,d)\\ &+ \overline{\overline{Q_{21}(-\mu,\mu_j)H_2(-\mu,\mu_j)}}\overline{G}(\mu_j)/\mu_j\\ &+ \overline{\overline{Q_{22}(-\mu,-\mu_j)H_3(-\mu,-\mu_j)}}\overline{G}(-\mu_j)/\mu_j \qquad (2.16)\end{aligned}$$

and

$$\begin{aligned}\overline{N_2}^{(1)} &= 2\pi\sum_{j=1}^{N} a_j[\overline{\overline{Q_{11}(\mu,\mu_j)H_4(\mu,\mu_j)}}\overline{L}(\mu_j,d)\\ &+ \overline{\overline{Q_{11}(\mu,\mu_j)H_5(\mu,\mu_j)}}\overline{G}(\mu_j)/\mu_j\\ &+ \overline{\overline{Q_{12}(\mu,-\mu_j)H_6(\mu,-\mu_j)}}\overline{G}(-\mu_j)/\mu_j \qquad (2.17)\end{aligned}$$

where $\mu_j = \cos\theta_j$, θ_j and a_j are the i^{th} Gaussian quadrature angle and its corresponding weight.

$$\overline{G}(\mu_j) = \overline{\overline{E}}^{-1}(\mu_j)\overline{F}(\mu_j) \qquad (2.18)$$

$$\begin{aligned}\overline{L}(\mu_j,d) &= \overline{\overline{E}}^{-1}(\mu_j)\overline{R}(\mu_j)\overline{\overline{E}}(-\mu_j)\overline{\overline{D_1}}(-\mu_j,d)\overline{\overline{E}}^{-1}(\mu_j)\overline{F}(\mu_j)/\mu_j\\ &+ \overline{\overline{E}}^{-1}(\mu_j)\overline{W}(\mu_j)CT_2 \qquad (2.19)\end{aligned}$$

$\overline{\overline{Q_{ij}}}$ and $\overline{\overline{H_n}}$ are 4×4 matrices; $\overline{\overline{QH}}$ is a matrix operation defined by

$$\overline{\overline{QH}} = [Q_{ij}H_{ij}] \tag{2.20}$$

For passive remote sensing, if the media are statistically azimuthally symmetric, all ϕ harmonics of phase matrix, except zero-order, will be averaged out.
$\overline{\overline{Q}}$ matrices are given by

$$\overline{\overline{Q_{11}(\mu,\mu_j)}} = \overline{\overline{E}}^{-1}(\mu)\overline{\overline{P}}(\mu,\mu_j)\overline{\overline{E}}(\mu_j) \tag{2.21}$$

$$\overline{\overline{Q_{12}(\mu,-\mu_j)}} = \overline{\overline{E}}^{-1}(\mu)\overline{\overline{P}}(\mu,-\mu_j)\overline{\overline{E}}(-\mu_j) \tag{2.22}$$

$$\overline{\overline{Q_{21}(-\mu,\mu_j)}} = \overline{\overline{E}}^{-1}(-\mu)\overline{\overline{P}}(-\mu,\mu_j)\overline{\overline{E}}(\mu_j) \tag{2.23}$$

$$\overline{\overline{Q_{21}(-\mu,\mu_j)}} = \overline{\overline{E}}^{-1}(-\mu)\overline{\overline{P}}(-\mu,-\mu_j)\overline{\overline{E}}(-\mu_j) \tag{2.24}$$

where $\overline{\overline{P}}(\mu,\mu_j)$ is zero-order component of Fourier expansion in ϕ of the phase matrices.

The physical interpretation of two scattering terms in equation (11) is illustrated in Figure 2.2 (*d*) and (*e*). The first scattering term is accumulation of downward scattering reflected by the surface at $z = -d$, then propagates through the layer. The second scattering term is accumulation of upward scattering.

This first-order multiple scattering is different from conventioned single-scattering solutions. In the conventional single-scattering solutions, attenuation is not considered when the wave propagates through media. Boundary conditions and polarizations are also eliminated to simplify the problem. In the first-order single scattering solution, complete polarimetric information is preserved. However, if the optical depth of the layer is very small, this first-order solution reduces to the conventional single-scattering solution [64].

2.1.2 *Discrete ordinate-eigenanalysis method*

The discrete ordinate-eigenanalysis method has been used in active remote sensing of a layer of nonspherical particles (ellipsoids) overlying Fresnel or Lambertian surfaces. This method can be used to find the full multiple-scattering solution of the vector radiative transfer equation. In this section, we derive a discrete ordinate-eigenanalysis approach for polarimetric passive remote sensing of a single layer of arbitrarily shaped particles overlying a ocean or land surface; then we will extend this approach for multiple layer structures.

Let's begin with equation(1) and Figure 2.1 again. Using Fourier Series of Stokes vectors, phase matrix and emission vector in (1), and applying Fourier decomposition and Gaussian quadrature formula, we have

$$\begin{aligned} \mu_i \frac{d\bar{I}(\mu_i, z)}{dz} &= -\overline{\overline{K_e}}(\mu_i)\bar{I}(\mu_i, z) + C\bar{F}(\mu_i)T \\ &+ 2\pi \sum_{j=-N}^{N} a_j \overline{\overline{P}}(\mu_i, \mu_j)\bar{I}(\mu_i, z) \end{aligned} \tag{2.25}$$

where $-1 \leq \mu_i \leq 1$ and $a_{-j} = a_j$.

Equation (25) can be rewritten in matrix form,

$$\begin{aligned} [\overline{\overline{\mu}}]\frac{d}{dz}[\bar{I}(\mu_i, z)] &= -[\overline{\overline{K_e}}(\mu_i)][\bar{I}(\mu_i, z)] + C[\bar{F}(\mu_i)]T \\ &+ 2\pi[\overline{\overline{P}}][\overline{\overline{a}}][\bar{I}(\mu_i, z)] \end{aligned} \tag{2.26}$$

where $[\overline{\overline{\mu}}]$ and $[\overline{\overline{a}}]$ are a $N \times 1$ diagonal matrices,

$$[\overline{\overline{\mu}}] = diag[\mu_1, \mu_1, \mu_1, \mu_1; \ldots; \mu_N, \mu_N, \mu_N, \mu_N; \mu_{-1}, \mu_{-1}, \mu_{-1}, \mu_{-1}; \ldots; \mu_{-N}, \mu_{-N}, \mu_{-N}, \mu_{-N}] \tag{2.27}$$

$$[\overline{\overline{a}}] = diag[a_1, a_1, a_1, a_1, \ldots, a_N, a_n, a_N, a_N; a_{-1}, a_{-1}, a_{-1}, a_{-1}, \ldots, a_{-N}, a_{-N}, a_{-N}, a_{-N}] \tag{2.28}$$

$[\bar{I}]$ is a column vector,

$$[\overline{I}] = [\overline{I}(\mu_1, z), \ldots, \overline{I}(\mu_N, z); \overline{I}(\mu_{-1}, z), \ldots, \overline{I}(\mu_{-N}, z)]^T \tag{2.29}$$

and

$$[\overline{\overline{K_e}}] = diag[\overline{\overline{K_e}}(\mu_i)] \tag{2.30}$$

$$\left(\overline{\overline{P}} \right) = \begin{pmatrix} \overline{\overline{P}}(\mu_1,\mu_1) & \ldots & \overline{\overline{P}}(\mu_1,\mu_N) & \overline{\overline{P}}(\mu_1,-\mu_1) & \ldots & \overline{\overline{P}}(\mu_1,-\mu_N) \\ \vdots & \vdots & \vdots & \vdots & & \\ \overline{\overline{P}}(\mu_N,\mu_1) & \ldots & \overline{\overline{P}}(\mu_N,\mu_N) & \overline{\overline{P}}(\mu_N,-\mu_1) & \ldots & \overline{\overline{P}}(\mu_N,-\mu_N) \\ \overline{\overline{P}}(-\mu_N,\mu_1) & \ldots & \overline{\overline{P}}(-\mu_1,\mu_N) & \overline{\overline{P}}(-\mu_1,-\mu_1) & \ldots & \overline{\overline{P}}(-\mu_1,-\mu_N) \\ \vdots & \vdots & \vdots & \vdots & & \\ \overline{\overline{P}}(-\mu_N,\mu_1) & \ldots & \overline{\overline{P}}(-\mu_N,\mu_N) & \overline{\overline{P}}(-\mu_N,-\mu_N) & \ldots & \overline{\overline{P}}(-\mu_N,-\mu_N) \end{pmatrix} \tag{2.31}$$

It is easy to verify that the particular solution to equation (26) is given by,

$$\left(\overline{I}_p \right) = \begin{pmatrix} T[\overline{I}_{ph}] \\ T[\overline{I}_{ph}] \end{pmatrix} \tag{2.32}$$

$[\overline{I}_{ph}]$ is a $4N \times 1$ column vector, $[\overline{I}_{ph}] = C[1,1,0,0;\ldots;1,1,0,0]$.

Seeking eigenvalues and eigenmatrix of equation(26), and separating the Stokes vector into upward going and downward going ones, we can express the general solution as

$$[\overline{I_u}] = \overline{\overline{\beta_u}}\overline{\overline{e^{\alpha\gamma}}} + [\overline{I}_{pu}]T \tag{2.33}$$

$$[\overline{I_d}] = \overline{\overline{\beta_d}}\overline{\overline{e^{\alpha\gamma}}} + [\overline{I}_{pd}]T \tag{2.34}$$

where $[\overline{I_u}]$ and $[\overline{I_d}]$ are upward and downward going Stokes vectors; $[\overline{\overline{\beta}}_u]$ and $[\overline{\overline{\beta}}_d]$ are their corresponding eigenmatrices, respectively. $\overline{\gamma}$ is an unknown coefficient vector.

The boundary condition at $z = -d$ can be written in matrix form,

$$[\overline{I}_u(z=-d)] = [\overline{\overline{R}}][\overline{I}_d(z=-d)] + C[\overline{W}]T_2 \tag{2.35}$$

where $[\overline{\overline{R}}]$ is reflectivity matrix, and $[\overline{W}]$ transmission vector.

For a Fresnel surface [63]

$$\left(\overline{\overline{[R]}} \right) = \begin{pmatrix} \overline{\overline{R}}(\mu_1) & & 0 \\ & \ddots & \\ 0 & & \overline{\overline{R}}(\mu_N) \end{pmatrix} \tag{2.36}$$

$$\left(\overline{[W]} \right) = \begin{pmatrix} \overline{W}(\mu_1) \\ \vdots \\ \overline{W}(\mu_N) \end{pmatrix} \tag{2.37}$$

$\overline{\overline{R}}(\mu_i)$ and $\overline{W}(\mu_i)$ are 4×4 reflection coefficient matrix and 4×1 transmission coefficient vector of planar dielectric interface, respectively.

For a lambertian surface the transmission vector $[\overline{W}]$ is in the same form as that of Fresnel surface; its reflectivity matrix is given by

$$\left(\overline{\overline{R}} \right) = (1 - e) \begin{pmatrix} \overline{\overline{a_1\mu_1}} & \cdots & \overline{\overline{a_N\mu_N}} \\ \vdots & \vdots & \vdots \\ \overline{\overline{a_1\mu_1}} & \cdots & \overline{\overline{a_N\mu_N}} \end{pmatrix} \tag{2.38}$$

where $\overline{\overline{a_i\mu_i}}$ is a diagonal matrix with ii^{th} element equal to $a_i\mu_i$; $\overline{W}(\mu_i) = e[1, 1, 0, 0]^T$; e is the emissivity of the surface.
At $z = 0$,

$$[\overline{I}_d(z = 0)] = 0 \tag{2.39}$$

Using the general solution in boundary conditions at $z = 0$ and $z = -d$, we have a set of matrix equation,

$$\begin{pmatrix} \overline{\overline{\beta}}_d & 0 \\ 0 & \overline{\overline{\beta}}_u - [\overline{\overline{R}}]\overline{\overline{\beta}}_d \end{pmatrix} \begin{pmatrix} \overline{\overline{1}} \\ \overline{\overline{e\alpha}}(-d) \end{pmatrix} \overline{\gamma} = \begin{pmatrix} -[\overline{I}_{ph}]T \\ CT_g[\overline{W}] + T_1(\overline{\overline{R}} - \overline{\overline{1}})[\overline{I}_{ph}]T \end{pmatrix} \tag{2.40}$$

where $\overline{\overline{1}}$ is unity matrix.

By solving this system of matrix equation, the upwelling temperatures is,

$$[\overline{I}_u] = \overline{\overline{\beta}}_u\overline{\gamma} + [\overline{I}_{pu}]T \tag{2.41}$$

The single-layer model can be easily extended to multiple layer structure as shown in Figure 2.3. In side each layer, we define vector radiative transfer equation; at bottom

($z = -d_M$) and top($z = 0$), boundary conditions are the same as those in single-layer model. At the boundary between s and $s+1$ layer($z = -ds$),

$$\overline{I}_{su} = \overline{I}_{(s+1)u} \tag{2.42}$$

$$\overline{I}_{sd} = \overline{I}_{(s+1)d} \tag{2.43}$$

Following a similar procedure as in one layer case, we get the system of matrix equation for multilayer case,

2.1.3 *Invariant Imbedding Method*

Invariant Imbedding method is a numerical approach for finding the solution to the radiative transfer equation [65]. It can be used for media with inhomogeneous temperature profiles. In this method, an arbitrary vertical structure is divided into a number of homogeneous layers. In each layer, the radiative transfer equation can be written in the form of interaction principle by making use of finite-difference and Gaussian quadrature integral formula. This is just like discrete ordinate-eigenanalysis method but the derivatives of Stokes vectors are approximated by finite-difference scheme. To integrate properties of all infinitesimal layers, the linear nature of the interaction principle is used repeatedly. The properties so obtained, which are in the form of the reflection and transmission matrices and emission source vectors of the whole medium, incorporate the boundary conditions of the transfer equations. In this way, the outgoing radiation and the radiation field inside the medium can be both obtained from the interaction principle.

2.1.4 *Single Scattering Analysis Using the DDA*

The discrete dipole approximation(DDA) is a flexible technique for the single scattering calculation of dielectric scatterers of arbitrary shape and arbitrary optical structure [13]. It's suitable to model ice crystals in the cloud. DDA method combine the incident, scattered and total field in an integral equation form by using dyadic Green's function. The scatterer is divided up into a number of discrete dipoles(cubes) whose size are much smaller than the wavelength. Then, the method of moment with delta testing is used to cast the integral equation into a linear system of equation that can be solved for the dipole moment of each

dipole for a given incident field. To enhance the accuracy of this algorithm, dielectric constants of dipole at scatterer edges are calculated according to the Lorentz-Lorenz mixing rule. From resulting dipole moments, the scattered far field, hence the extinction and phase matrices, can be calculated readily from far field approximations. To interface with radiative transfer models, the Fourier transform of the phase matrix is taken and outputed in terms of its Fourier coefficients.

2.2 Theoretical model validation

In this section, models which are developed in section 2.1 are tested against previous published results and against each other. For the convenience of comparison and analysis, we will use both (I, Q, U, V) stokes parameters and (I_v, I_h, U, V) modified Stokes parameters. They are simply related by $I_v = I + Q$ and $I_h = I - Q$. The DDA method is used to provide information needed by the vector radiative transfer models. Statistical azimuthal symmetry of the media is always assumed in all of the simulations, unless stated otherwise. The Gaussian quadrature formula is used to divide the radiation into 32 discrete streams in order to accurately represent the spatial variation of radiation.

We tested our zero- and first-order iterative models against the results presented by Tsang [66]. In [66], the zero-order iterative method is used for the passive remote sensing of a layer of small spheroids with homogeneous temperature profile overlying a Frensel surface. Since spheroids are very oblate, major axis 2a=5cm and minor axis 2c=0.5cm, they are divided up into 688 dipoles in DDA method to have their shape modeled accurately. The frequency is 1.225GHz. Other parameters for the layer in Figure 2.1 are $\epsilon_s = (16.5 + i0.5)\epsilon_0$, $\epsilon_2 = (15 + i2)\epsilon_0$, d=2.5 meters, T=300K, $T_2 = 300K$ and fractional volume of particles= 0.0055. This is a typical case found in passive microware remote sensing of forests and vegetation. Very good agreements are obtained between our zero-order solution and previously published ones [66](not presented here). We plot our zero- and first-order solutions in Figure 2.4 through Figure 2.6. Figure 2.4 shows zero- and first-order solution as a function of observation angles for both vertical and horizontal polarizations. The difference between these two solutions increases with observation angle, which is related to optical thickness of the path. In this specific case, the zero-order solution is a very good approximation. As we have shown in Figure 2.2, the first-order solution includes five terms, (a) reflected emission, (b) emission from ground, (c) direct emission from the layer, (d) diffusion (scattering) reflected by the surface, (e) diffusion

directly from the layer. Figure 2.5 and Figure 2.6 plot the first-order solutions and their five terms for vertical and horizontal polarizations, respectively. For vertical polarization, the brightness temperature is mainly due to the emission from the ground; for horizontal polarization, ground emission dominates the brightness temperature for $\theta \leq 70°$; beyond 70°, emission from the layer takes over. This difference is due to the polarimetric emission of the particles of oblate shape. It is to be noted that the reflected emission and diffusion are modulated by the angular dependence of the specular surface reflectivity; and that vertical polarized ones vanish at Brewster's angle.

First-order iterative results in Figure 2.4 are also tested against the discrete ordinate-eigenanalysis method in Figure 2.7. Excellent agreements are achieved. This indicates that first-order solutions are sufficient in this case.

A test between the eigenanalysis method and the invariant imbedding method is shown in Figure 2.8 through Figure 2.13. In this test, a layer of cirrus type cloud overlying a Lambertian surface is simulated. The cloud is made up of 1mm monodistribution of columns, which are modeled as cylinders of 1mm in length and 0.3075mm in diameter. The microwave frequency is 85GHz, one of current spaceborne radiometer channels. Ground and cloud temperature are set to be 300K and 225K, respectively. The refraction of ice crystals at 85GHz for a temperature of -60 degrees is interpolated from tables in [51]. Ice water content (IWC) of $0.1g/m^3$ is used in the cloud. The Stokes parameters I and Q are plotted to compare invariant imbedding and eigenanalysis method. In Figure 2.8 and Figure 2.9, emissivity of the land e=0.95 and the thickness of the layer d=1km; in Figure 2.10 and Figure 2.11, e=0.95 and d=5km; in Figure 2.12 and Figure 2.13, $e = 0.1$. Excellent agreements are obtained for all the cases.

Because of the insignificance of emission from cirrus clouds, the physical temperature of cirrus cloud is not important. When the optical depth is small, in Figure 2.8, the observed temperature I is basically the brightness temperature of the ground; when the optical depth becomes very large, the brightness temperature I is depressed greatly as shown in Figure 2.10. On the other hand, brightness temperature Q usually increases with optical depth, then decreases at very large optical depth. In Figure 2.12 and Figure 2.13, the brightness temperature are extremely low because the ground emission is depressed by using a small surface emissivity $e = 0.1$.

2.3 Model calculation at 89 and 150GHz

To understand the emission and scattering processes in the winter cloud, we have simulated passive remote sensing of winter cloud at 89GHz and 150GHz, two of current radiometers channels, by using the discrete ordinate-eigenanalysis models. The cloud is modeled as a layer of ice crystals with supercooled water overlying land or ocean surface with an emissivity of 0.9 and ground temperature 258K. Different combinations of ice water content (IWC) and supercooled liquid (SLW) content are used in these simulation.

Supercooled liquid water droplets can be modeled by Rayleigh scattering because of their very small diameters [43]. On the other hand, ice crystals have much larger sizes. Their shapes and size distributions have profound impacts on the passive remote sensing. The effect of different particle shapes on the emission from clouds has been studied in [11]. To focus us on the relationships among ice water content, liquid water content and brightness temperatures of the cloud, we assume that crystals are of only plate shapes and follow the power law size distribution $N = Ad^{-3}$, where$N$ is the number concentration and d is the maximum dimension of plates. A was chosen to normalize the ice mass concentration to a desired value. The size distribution is approximated by six discrete size with each representing an average of a size interval around it. Because of the nonlinearity of electromagnetic behavior of ice particles as a function of their maximum size, the average points and size intervals are chosen according to geometrical mean [9]. For example, Particles of size d_i is an average between $(\sqrt{d_{i-1}d_i}, \sqrt{d_i d_{i+1}})$, and the number concentration of size d_i particles is given by $N_i = \frac{A}{2d_i}(\frac{1}{d_{i-1}} - \frac{1}{d_{i+1}})$. The thickness and volume for each size are calculated according to $h = 0.0141d^{0.474}$ and $v_c = 9.17 \times 10^{-3}d^{2.475}$ [48]. A summation of all ice particles gives the total ice water content, $IWC = \rho \sum_i v_c(d_i)$, where $\rho = 0.92g/cm^3$ is the bulk density of ice crystals. The refraction index of ice plates at 89 and 150GHz are interpolated from tables in [51] for a temperature $-15°C$. See Table 2.1 for a parameter list for $IWC = 0.1g/m^3$.

Figure 2.14 to Figure 2.20 illustrate simulations at 150GHz. Figure 2.14 and Figure 2.15 show the brightness temperatures I and Q as a function of liquid water content or liquid water path observed at 54 degree zenith angle. Ice water content and liquid water content are changed from very low to very high values; 0.1 to $0.6g/m^3$, for both IWC and LWC. It can be see that brightness temperatures I and Q are well behaved as functions of IWC and LWC. A increase of IWC will darken I but brighten Q. On the other hand, different combination of LWC and IWC could give the same brightness temperature I, but

Table 2.1: Size distribution of ice clouds.

Max. Dimension (mm)	Min. Dimension (mm)	volume v_c (cm^3)	number concentration (m^{-3})
0.060	0.00124	2.906×10^{-8}	2.440×10^{5}
0.125	0.00177	1.787×10^{-7}	5.552×10^{4}
0.250	0.00245	9.937×10^{-7}	1.315×10^{4}
0.500	0.00341	5.525×10^{-6}	3.287×10^{3}
1.000	0.00473	3.072×10^{-5}	8.218×10^{2}
2.000	0.00658	1.708×10^{-4}	2.056×10^{2}

Frequency	Ice refraction index	Water refraction index
89GHz	(1.7828,0.00432)	(2.4552,1.05462)
150GHz	(1.7822,0.0048)	(2.2782,0.67406)

their corresponding Q may not be the same. This could provide a retrieval scheme for the total ice water content and liquid water content. The emission from liquid water droplets exhibits nonlinear characteristics; it increases rapidly with LWP at first, then becames saturated for large LWP.

In Figure 2.16 and Figure 2.17, IWC is fixed at $0.3g/m^3$ while LWC is changed. I and Q are plotted as a function of observation angle or ice water path. It is noted that brightness temperatures are very sensitive to LWC at lower liquid water content and large observation angles.

Because the extinction coefficients of ice particles usually change slowly with zenith angle, optical thickness of paths change quite linearly with liquid water path or ice water path, especially when the liquid water droplet has a absorption coefficient comparable or larger then the extinction coefficient of ice particles. In Figure 2.18 through Figure 2.20 ice water path and liquid water path are made equal by choosing $IWC = LWC = 0.3g/m^3$. Optical depths are plotted in Figure 2.18 as a function of ice water path or liquid water path for both vertical and horizontal polarizations. In Figure 2.19 and Figure 2.20, vertical and horizontal brightness temperatures are plotted vs their optical depths.

Simulations at $89GHz$ and their comparisons with those at 150 GHz are shown in Figure 2.21 to Figure 2.24. Results for 89 GHz are plotted in dash lines. As the graphs

Table 2.2: Optical characteristics of ice clouds.

Bulk density (g/cm^3)	Effective Permittivity	Extinction Coefficient (km^{-1})	albedo
0.92	$(1.7822, 4.80) \times 10^{-3}$	0.6051987	0.9602
0.50	$(1.3742, 1.91) \times 10^{-3}$	0.937797	0.9874
0.10	$(1.0694, 3.21) \times 10^{-4}$	0.302584	0.9780

show, there are some strong resemblances between 89 GHz and 150 GHz case. In Figure 2.21 and Figure 2.22, at both frequencies, brightness temperatures change smoothly with liquid water path for a fixed ice water content, although the slope at different frequency is usually different. In other words, correlations exist between liquid water path and brightness temperatures at both low and high frequencies. Strong relationships can also be found between ice water path and brightness temperatures in Figure 2.23 and Figure 2.24. All these make it difficult to accurately discriminate liquid water path from ice water path by using the conventional dual-frequency technique.

For all of the above simulations, we fixed the bulk density of ice crystals at $\rho = 0.92g/m^3$. In real clouds, ρ can change widely from 0.1 to $0.92g/m^3$. For example, high-density ice such as hail can be found in thunderstorms; low-density ice such as snowflake is often found in winter storms. Bulk density of ice has a strong influence on the electromagnetic behavior of ice layer. To study the impact of bulk density on the brightness temperatures, let's consider a layer of spherical ice particles with nonprecipitating liquid water droplets overlaying a land surface with an emissivity of 0.95 and a physical temperature of 273K. Ice particles follow the Gamma size distribution with mean diameter $d_0 = 1mm$ and ice water content $IWC = 0.3g/m^3$. Cloud thickness is 2km and cloud temperature 258K. The microwave frequency used was 150GHz. Three different ice bulk density ρ were chosen while the ice water content was kept the same. Mie scattering method was applied to perform the single scattering calculations. Some results are tabulated in Table 2.2.

Figure 2.25 plots the brightness temperature I observed at 54° zenith angle as a function of liquid water content for different ice bulk density(Q is always very small for spherical particles). As we can see from Figure 2.25, decreasing in ice bulk density will increase the

brightness temperature I due to the reduction of scattering by ice particles. The temperature difference for $\rho = 0.92$ and $0.1g/m^3$ can be as large as 55K. In other words, brightness temperature is sensitive to the bulk density of ice particles. This provides us an opportunity to retrieve bulk density of ice crystals; but, at the same time, makes the retrieval algorithm even more complicated. It is to be noted that the increment in brightness temperature becomes less with the increase of liquid water content. On the contrary, the brightness temperature changes more rapidly for low-density ice particles. However, this difference offers insufficient information to distinguish temperature brightenings introduced by liquid water from that by lower density of ice particles. Figure 2.26 plots brightness temperature vs ice water path.

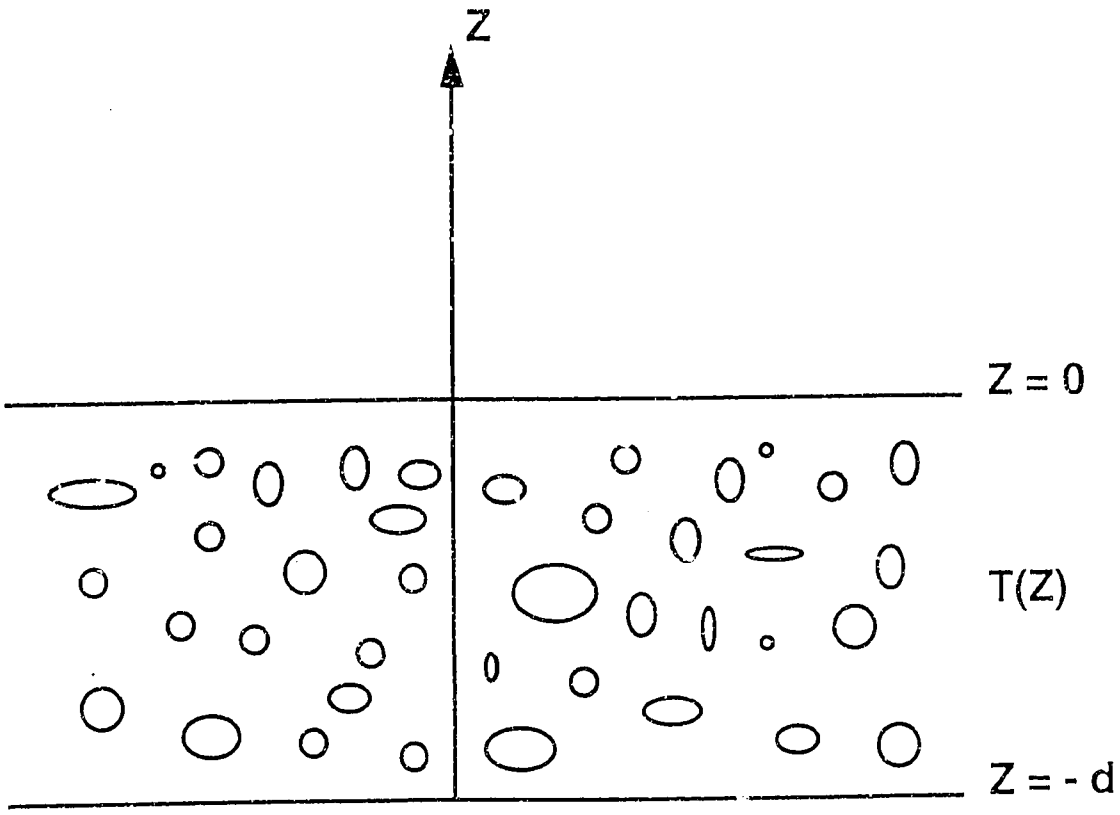

Figure 2.1: An incident plane wave impinging upon a layer of nonspherical particles overlying a homogeneous half space of permittivity ϵ_2.

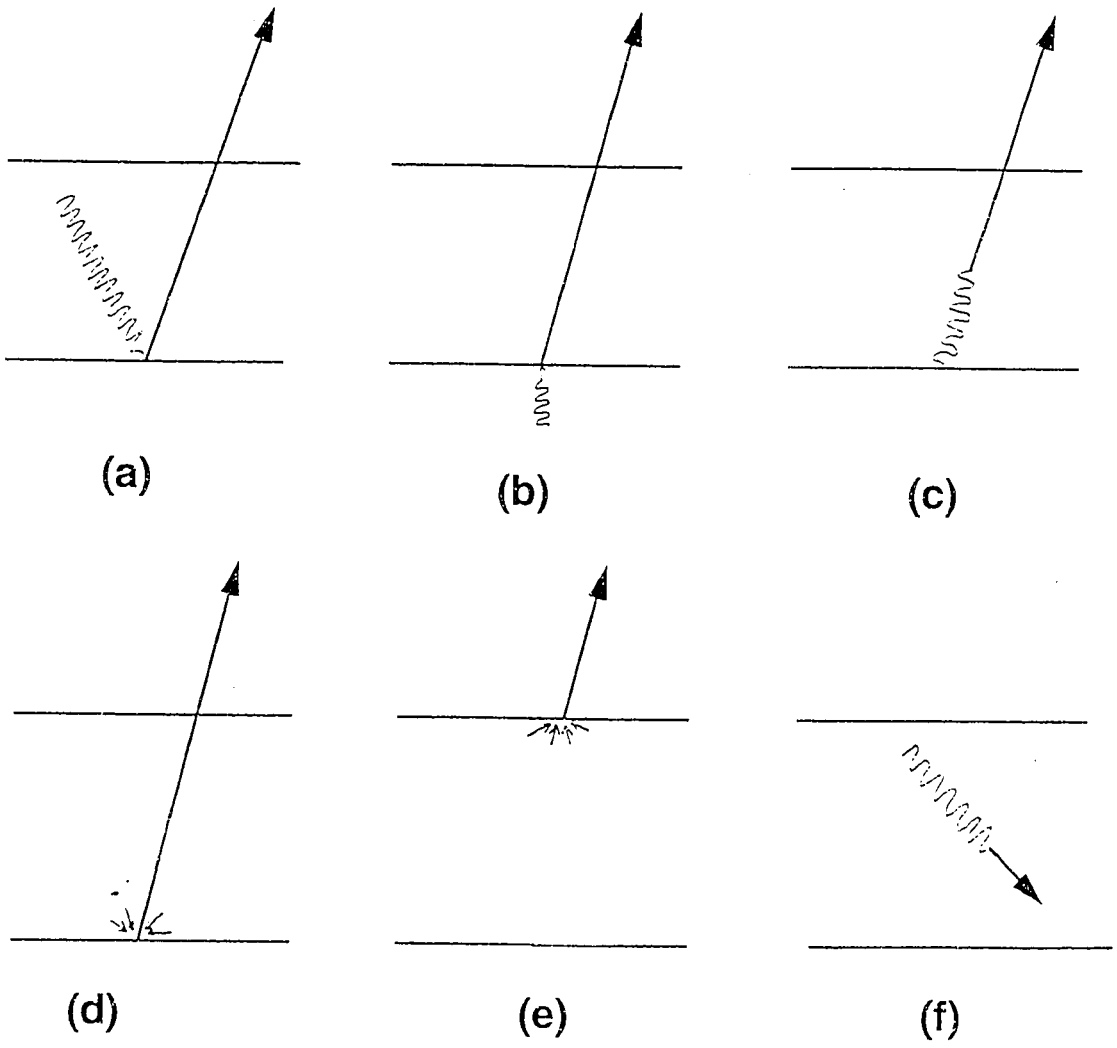

Figure 2.2: Components contributing to the first-order iterative solution of radiative transfer equations

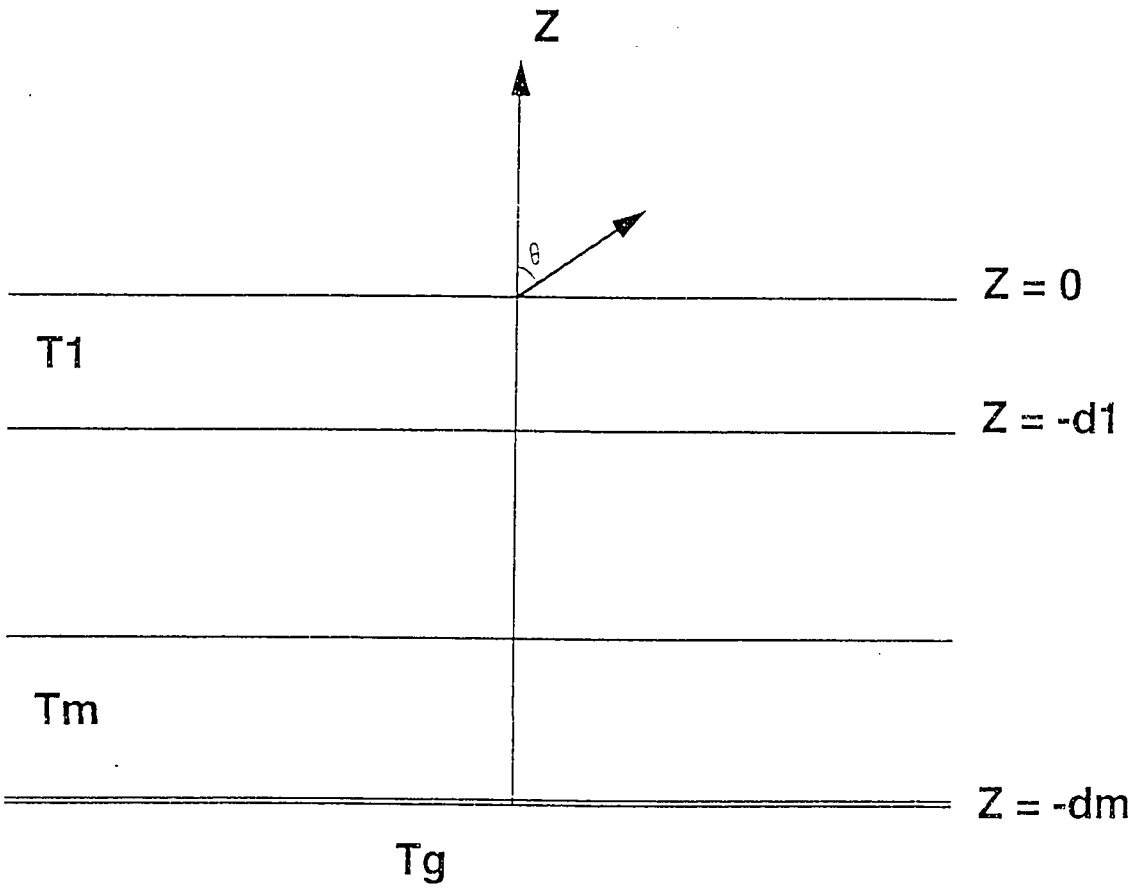

Figure 2.3: An incident plane wave impinging upon multilayer of nonspherical particles overlaying a homogeneous half space of permittivity ϵ_2.

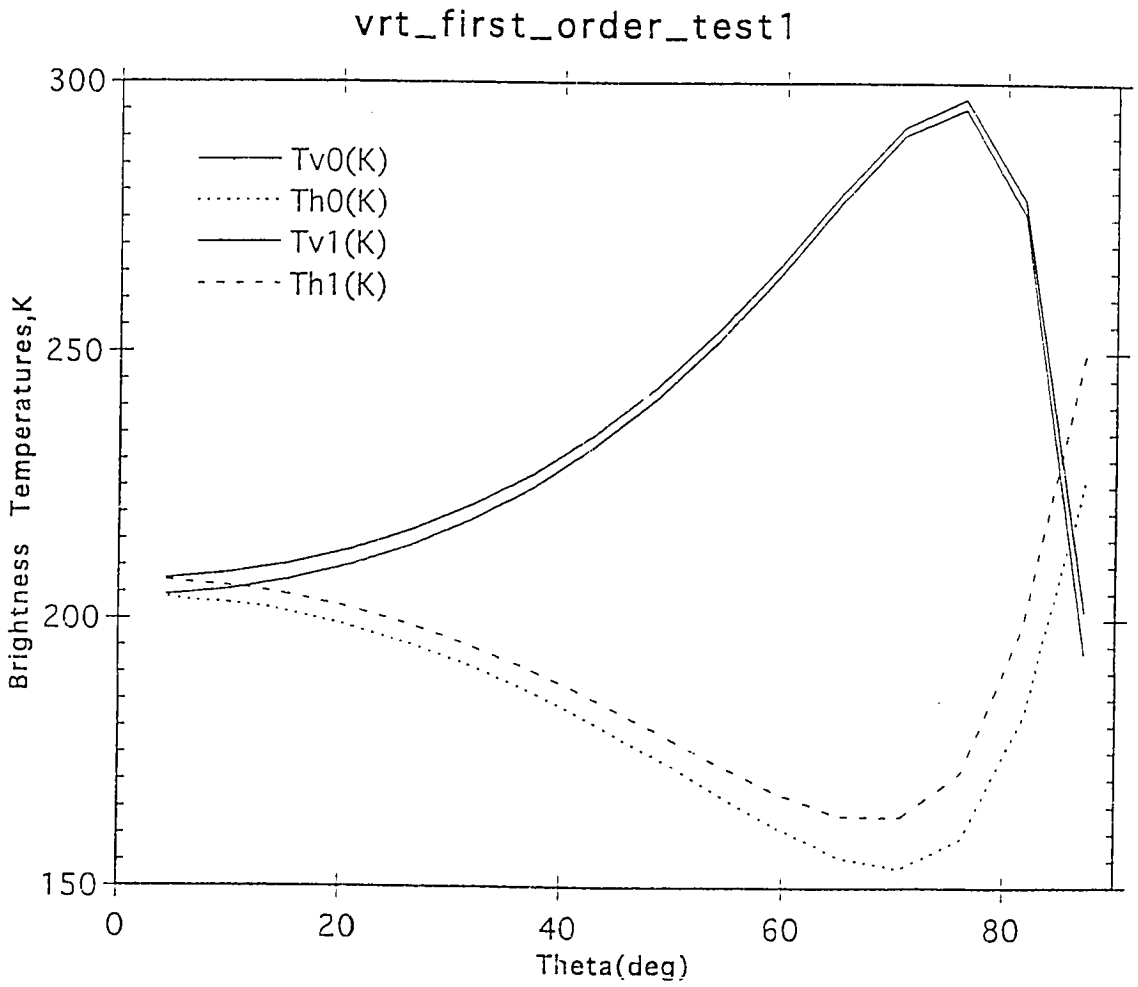

Figure 2.4: Zero- and first-order iterative solution of radiative transfer equations. Polarimetric brightness temperatures are plotted as a function of observation angle.

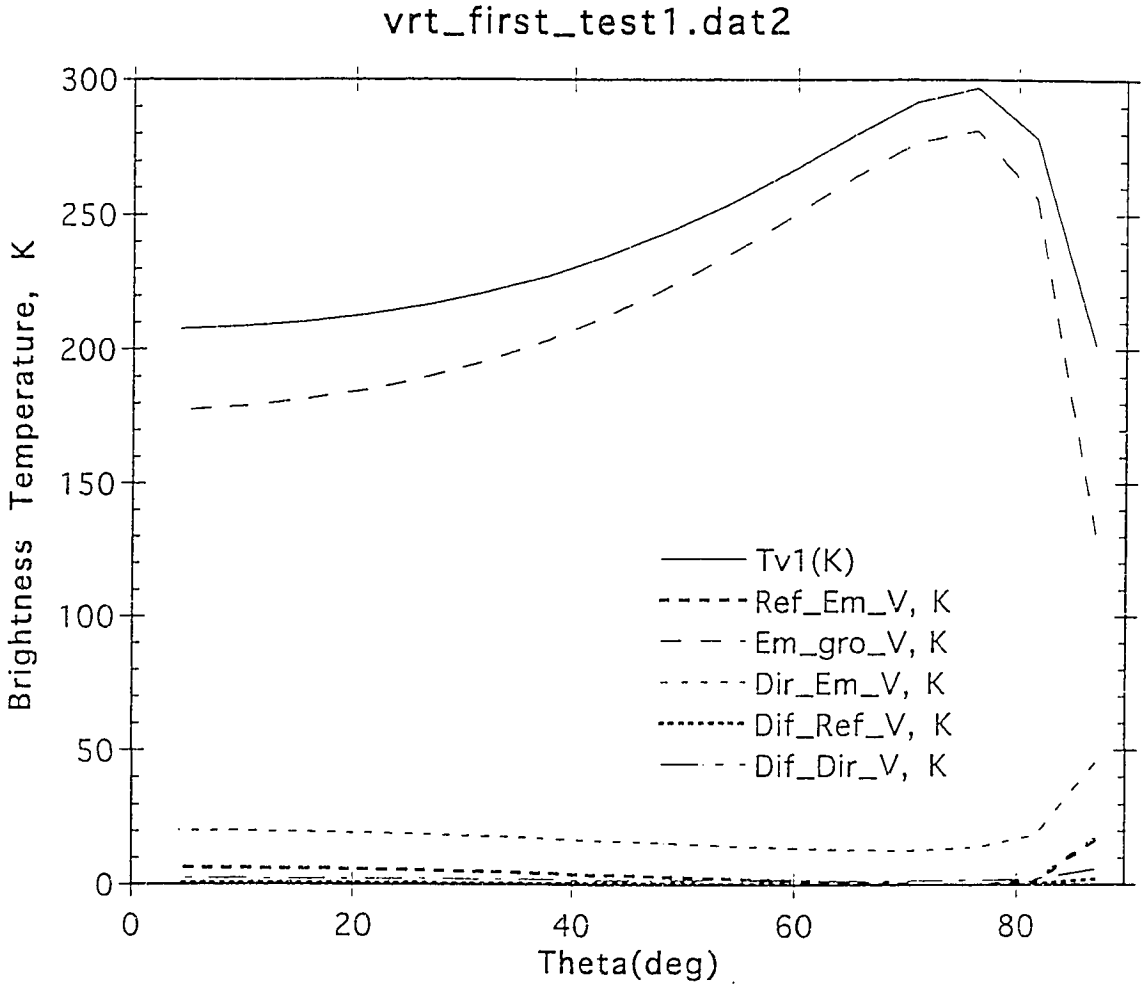

Figure 2.5: Five components of first-order iterative solutions as a function of observation angle: vertical polarization.

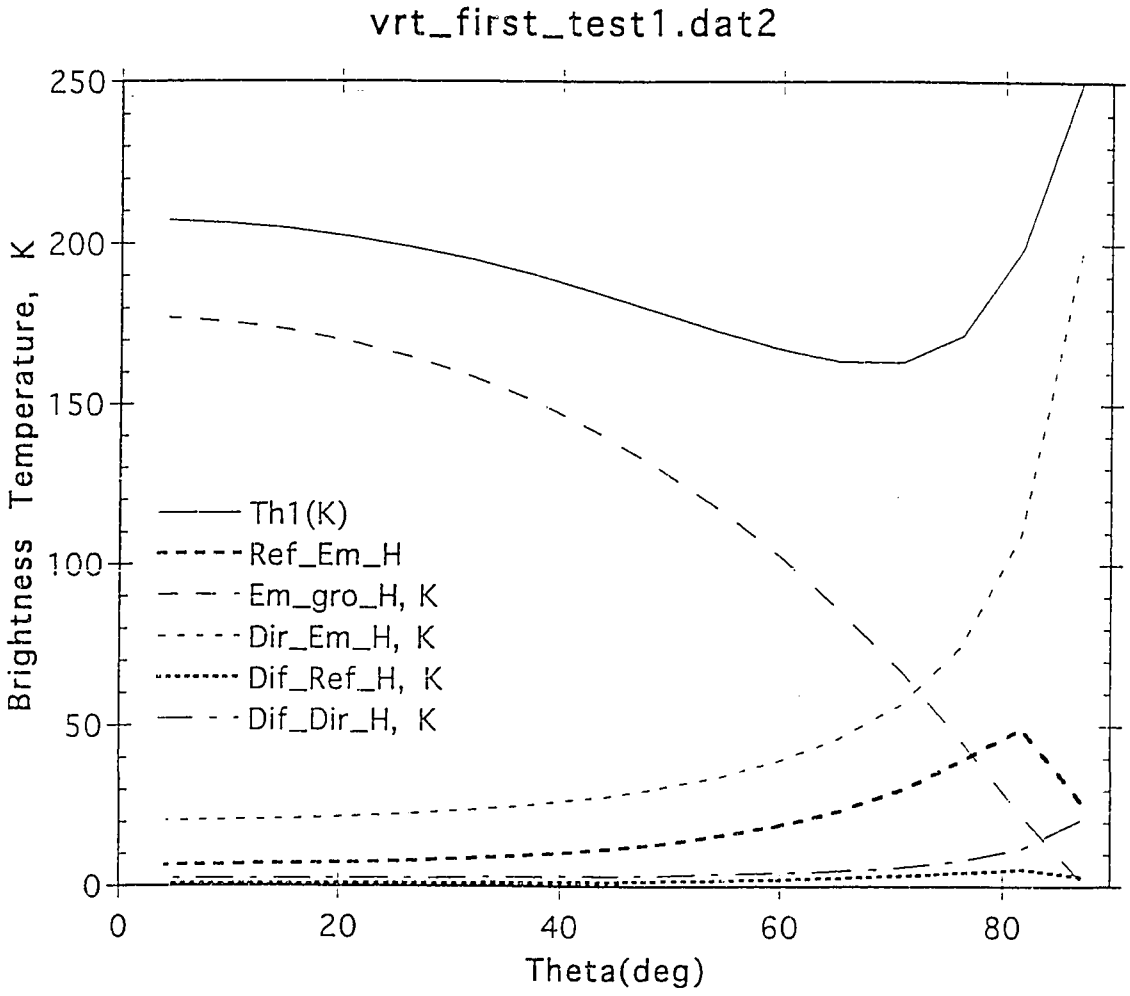

Figure 2.6: Five components of first-order iterative solutions as a function of observation angle: horizontal polarization.

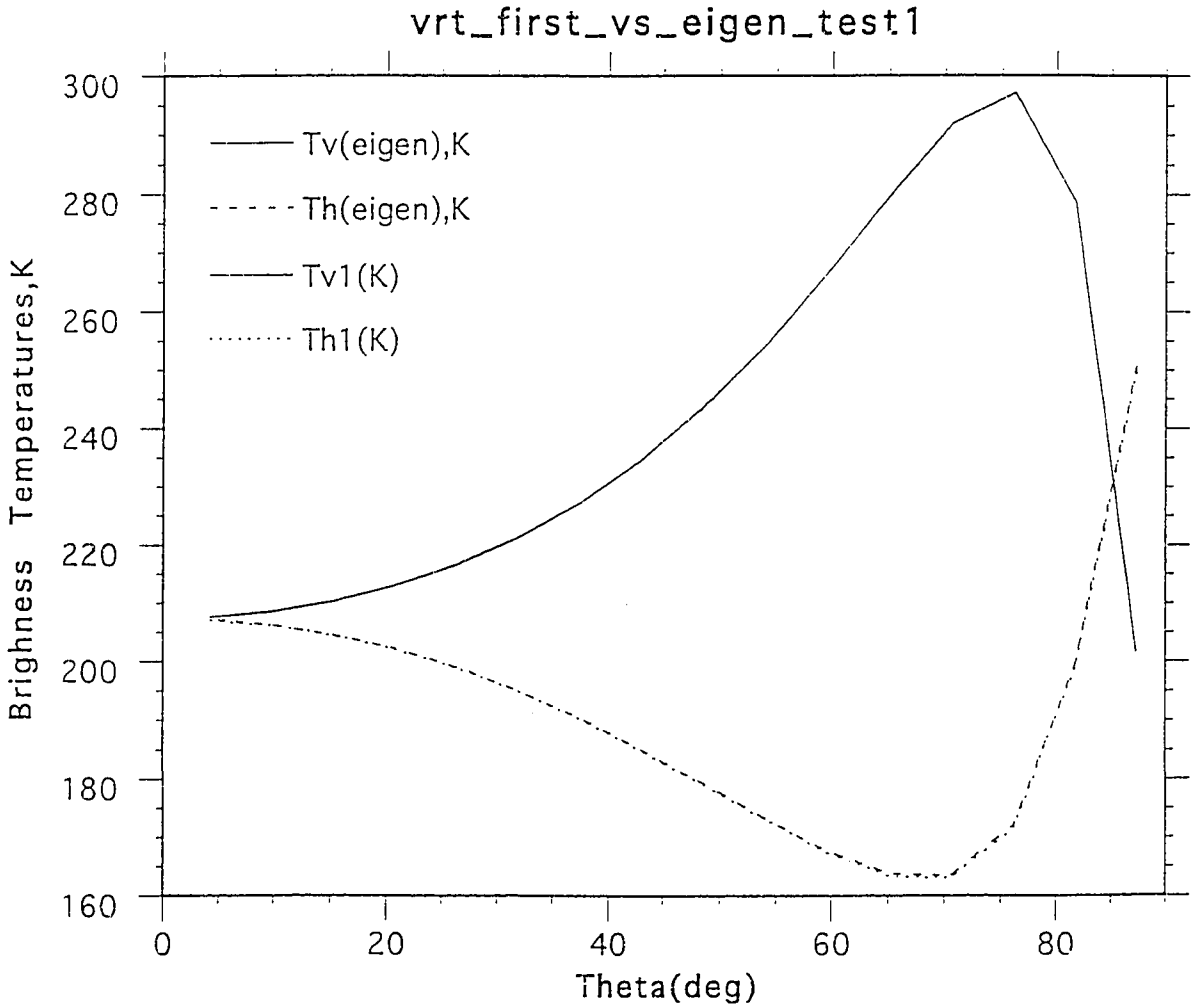

Figure 2.7: Comparison of brightness temperatures between first-order iterative method and eigenanalysis method on a layer of vegetation overlying a Frensel surface.

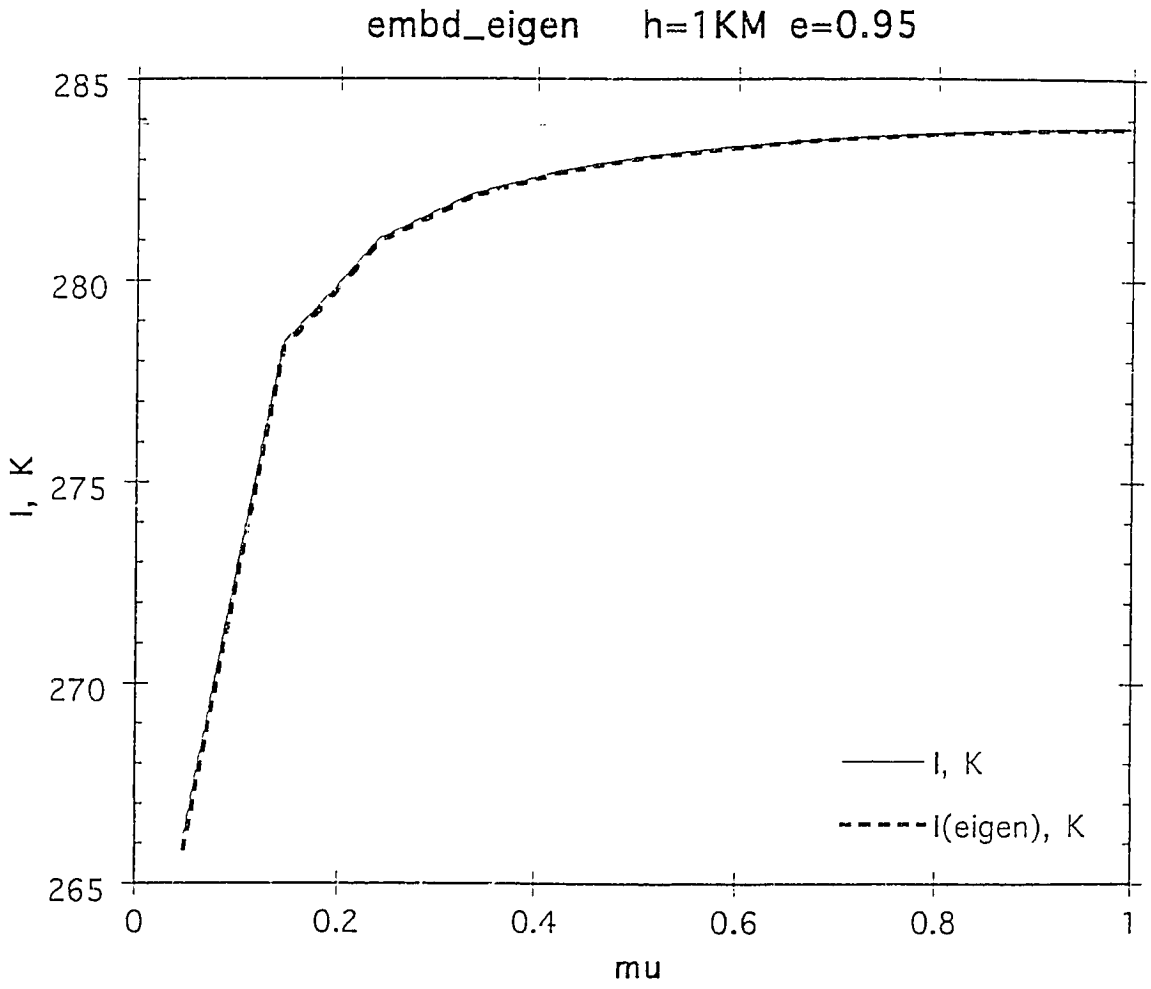

Figure 2.8: Comparison of brightness temperatures between eigenanalysis method and invariant embeding method on a layer of cirrus cloud overlying a Lambertian surface with emissivity of 0.95: brightness temperatures I.

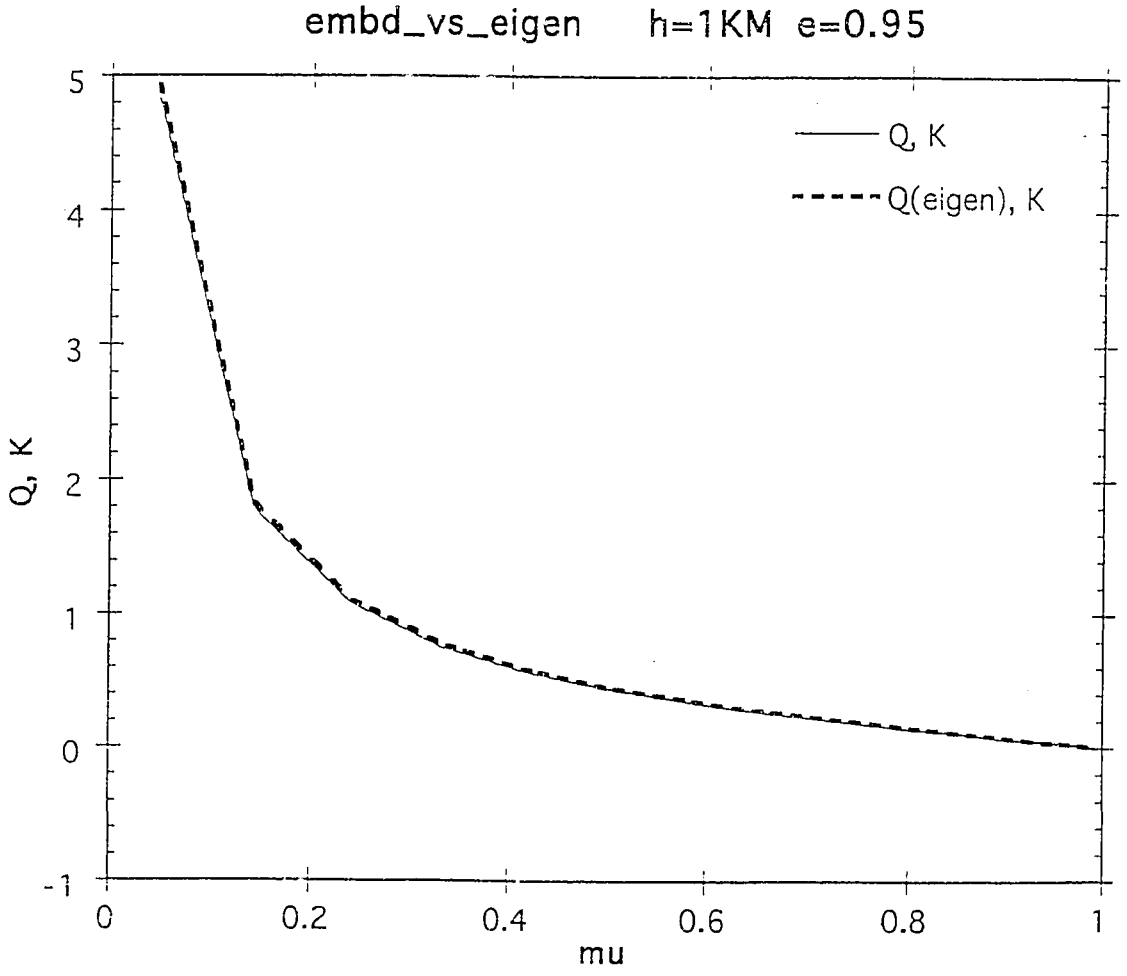

Figure 2.9: Comparison of brightness temperatures between eigenanalysis method and invariant embeding method on a layer of 1 Km cirrus cloud overlying a Lambertian surface with emissivity of 0.95: brightness temperatures Q.

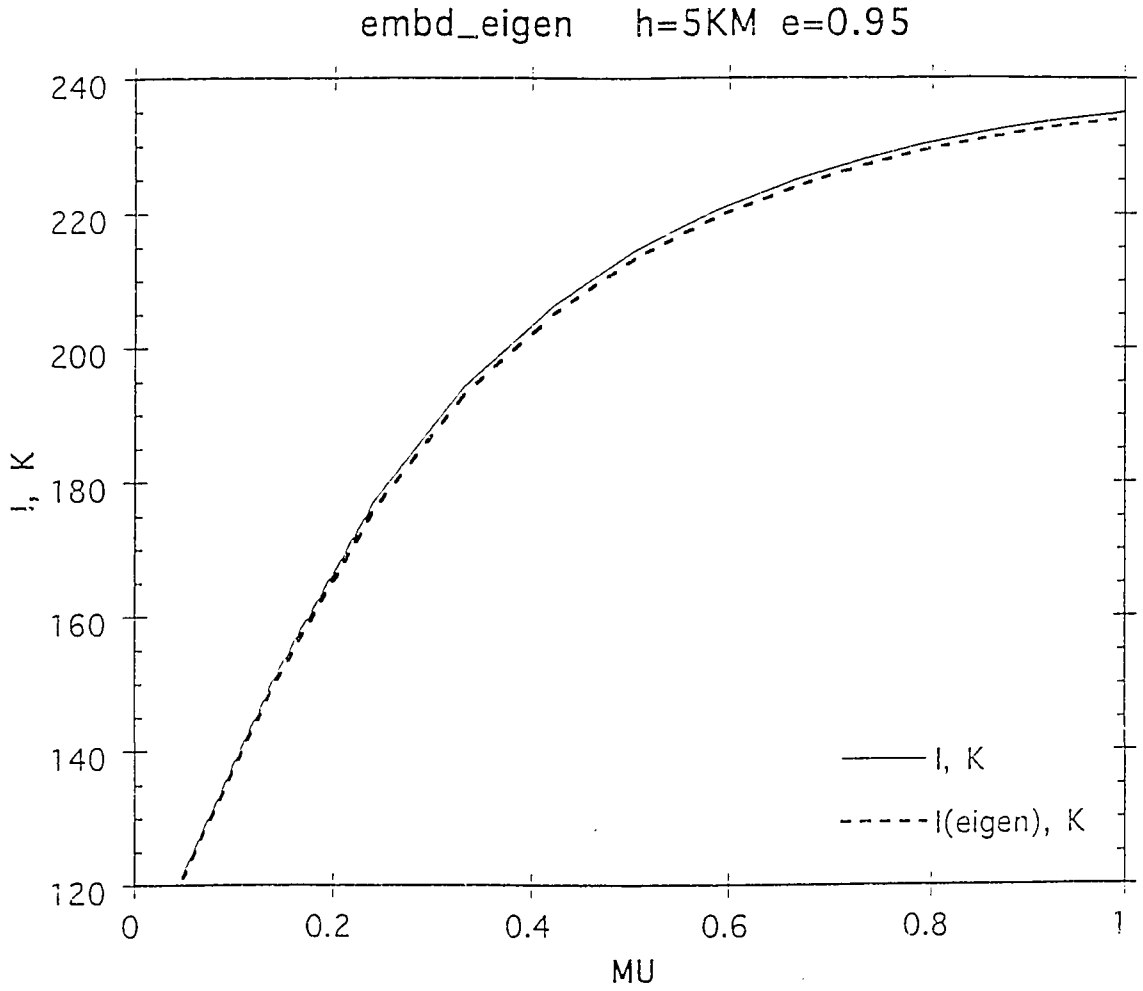

Figure 2.10: Same as Figure 2.8, but cloud depth is 5 Km.

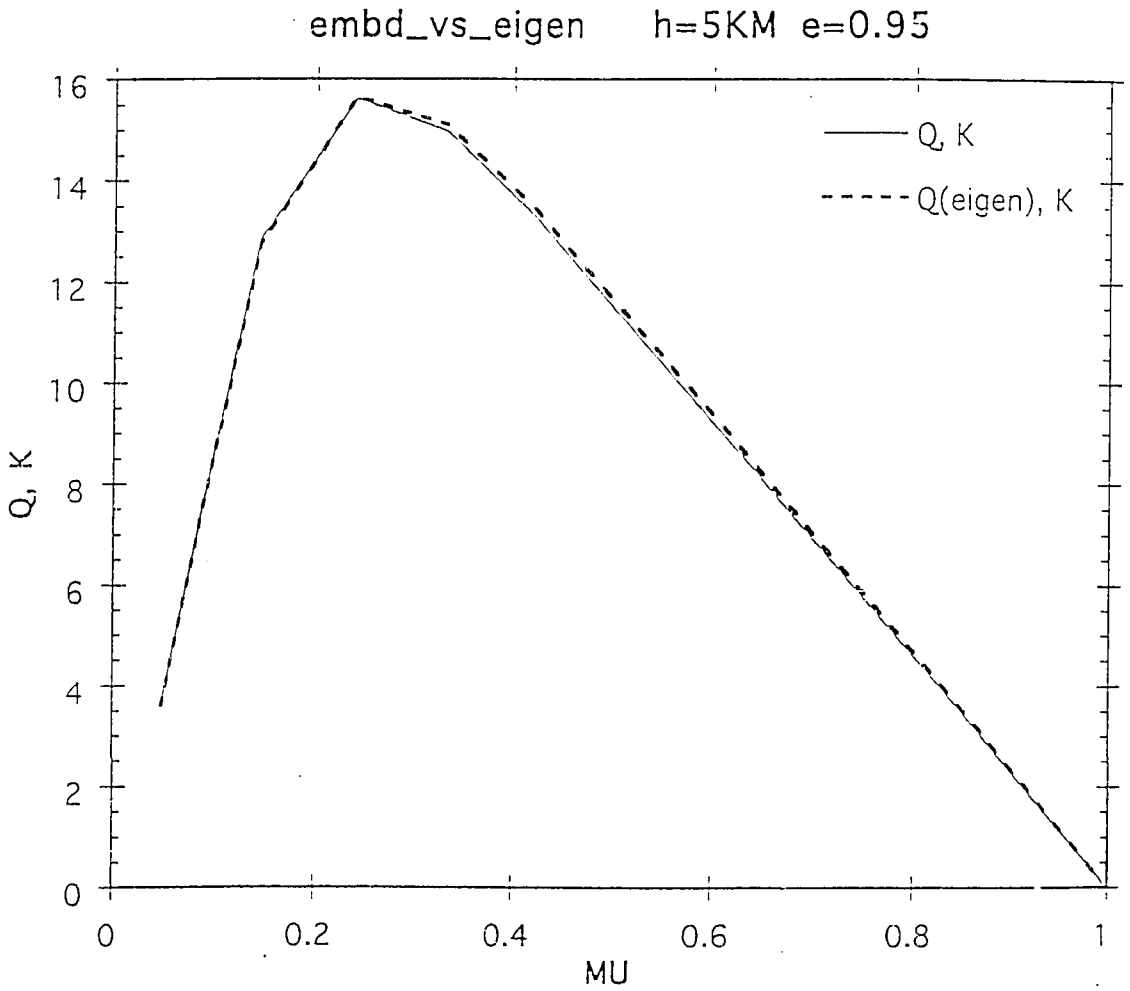

Figure 2.11: Same as Figure 2.9, but cloud depth is 5 Km.

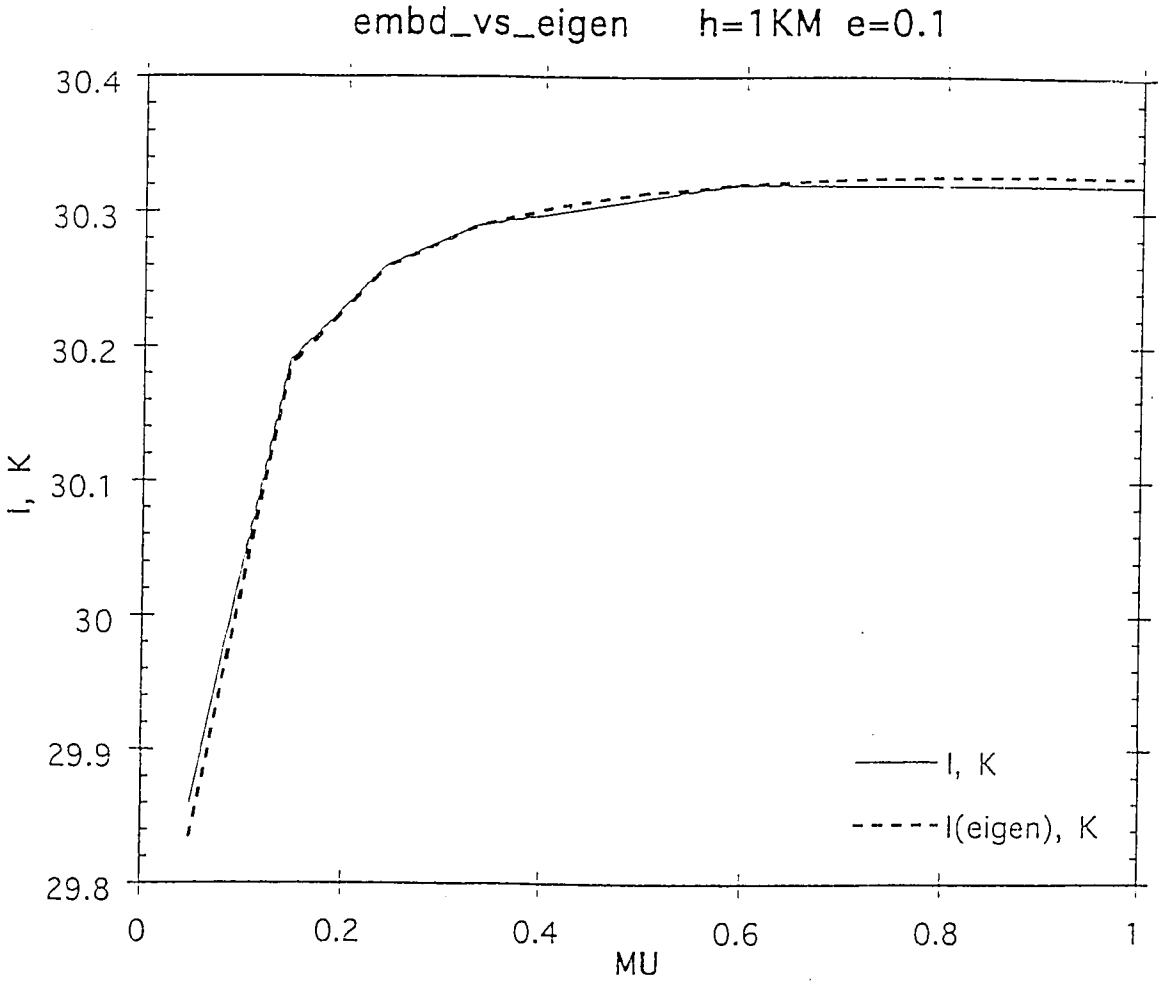

Figure 2.12: Same as Figure 2.8, but emissivity is 0.1.

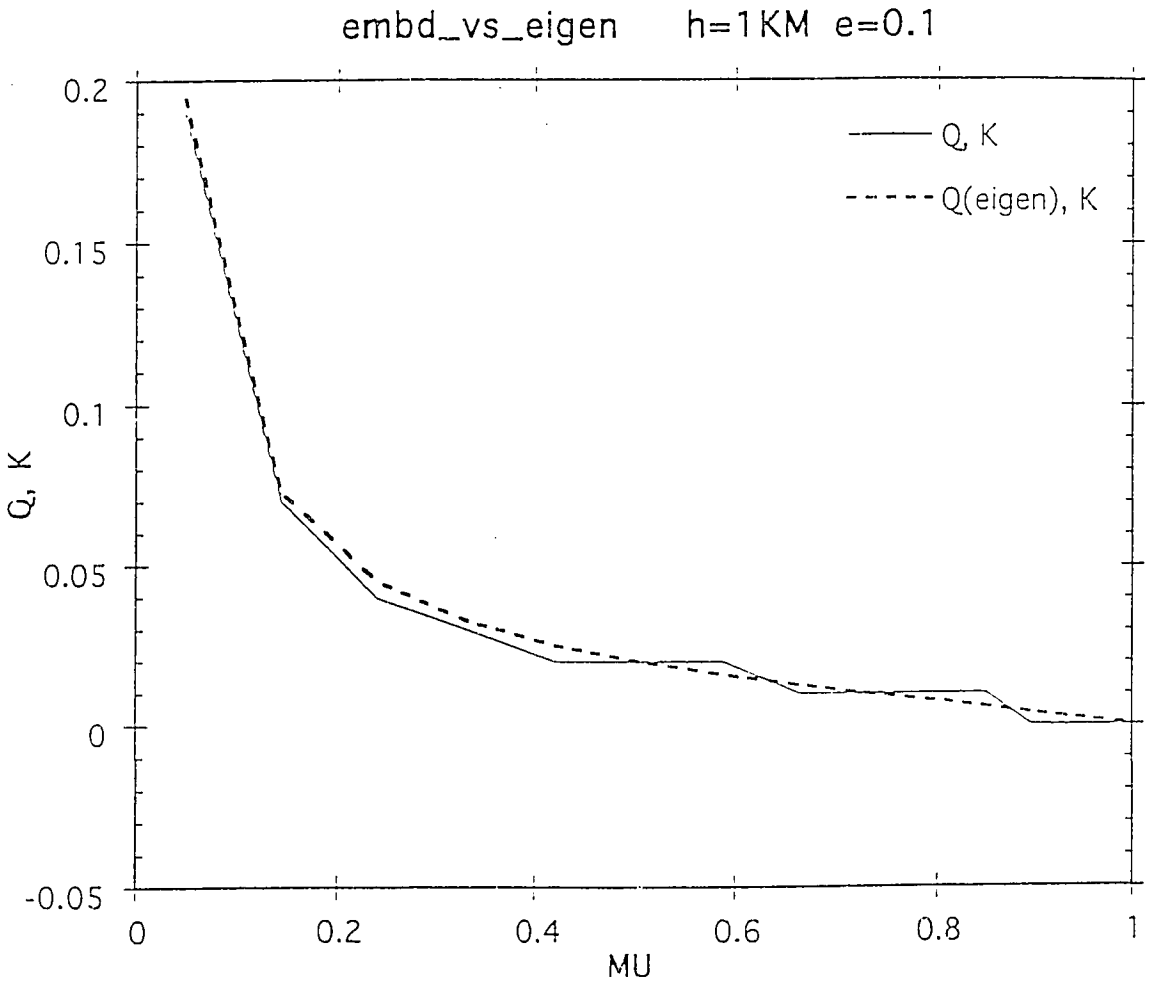

Figure 2.13: Same as Figure 2.9, but emissivity is 0.1.

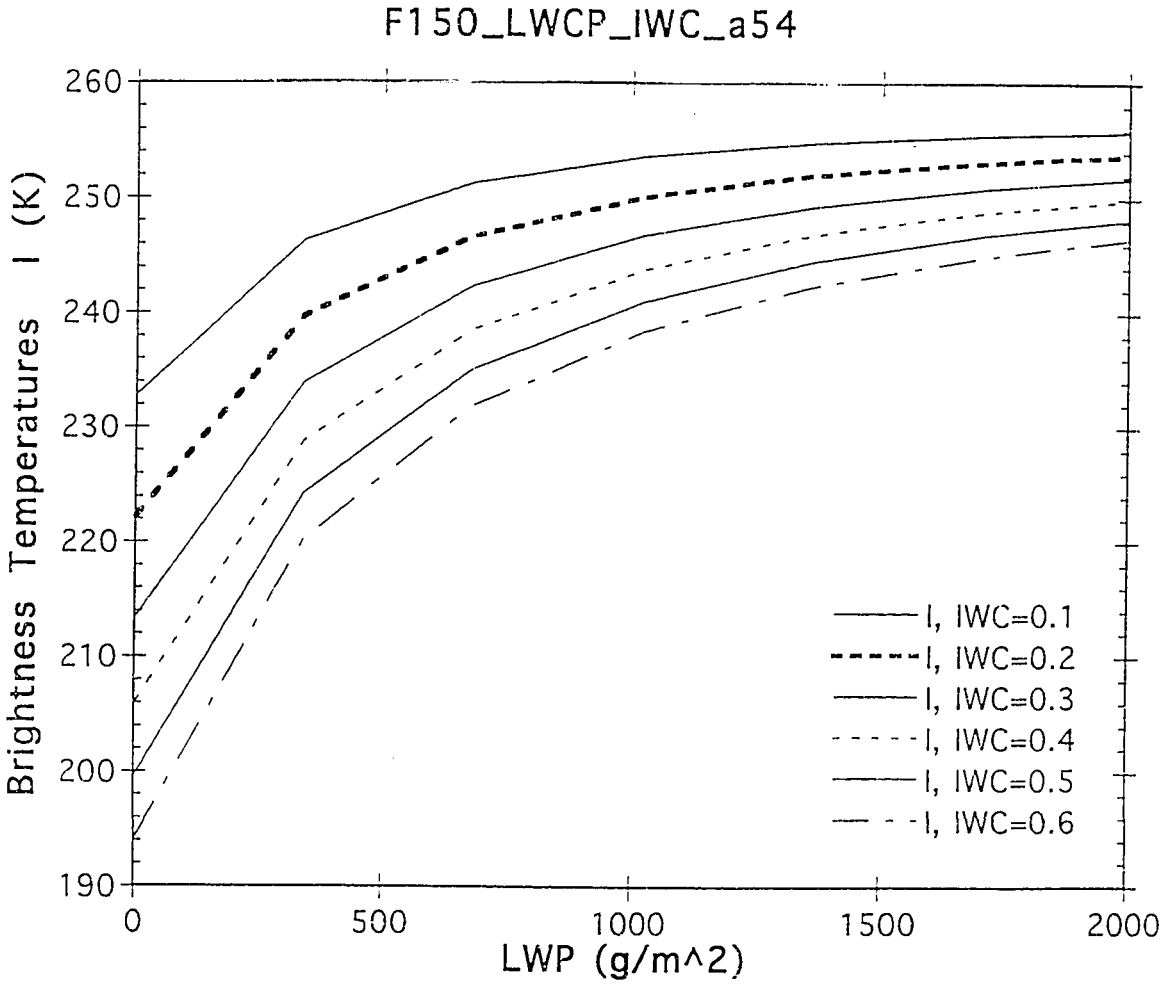

Figure 2.14: Brightness temperature I as a function of liquid water path (LWP) for some fixed ice water path (IWP) values.

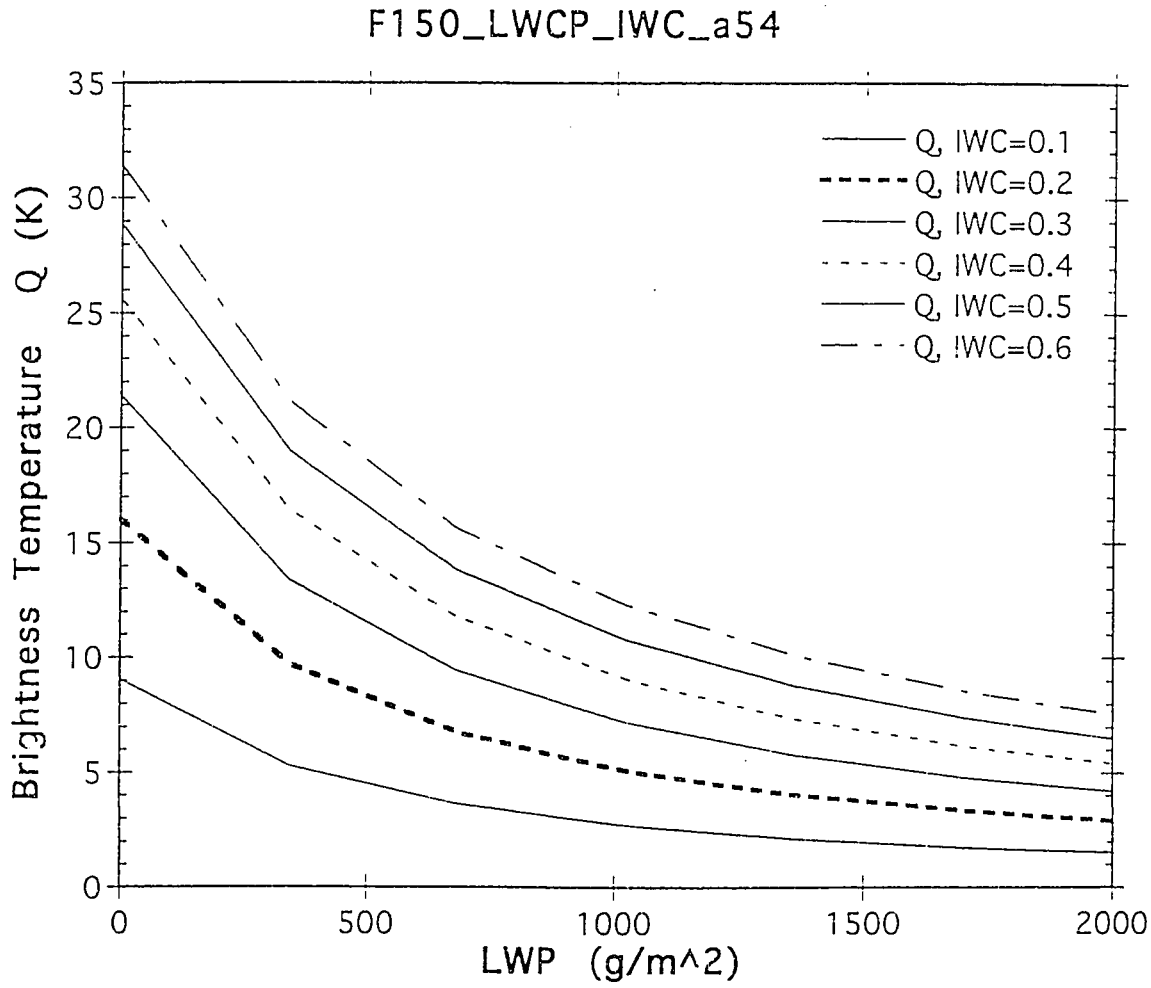

Figure 2.15: Brightness temperature Q as a function of liquid water path (LWP) for some fixed ice water path (IWP) values.

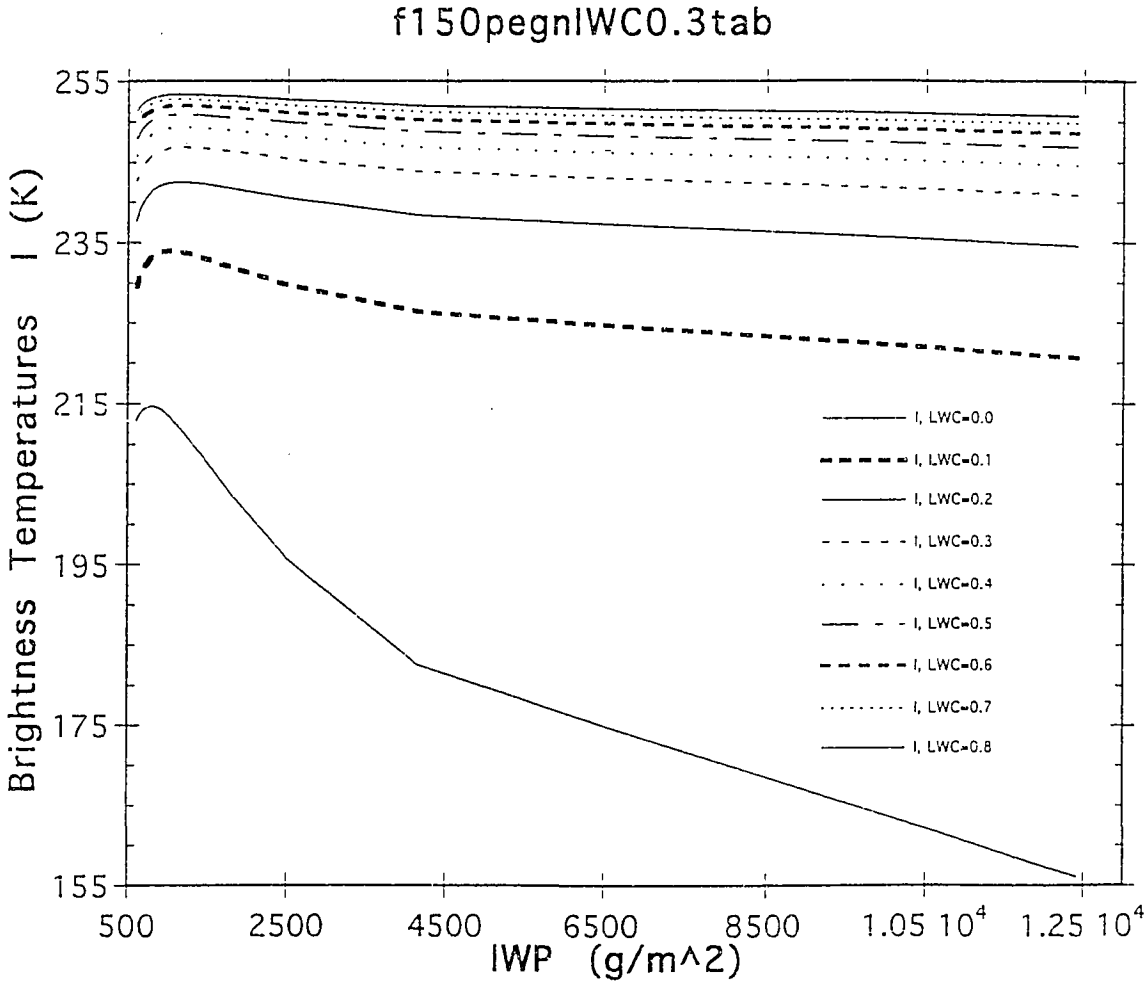

Figure 2.16: Brightness temperature I as a function of ice water path (IWP) for some fixed liquid water path (LWP) values.

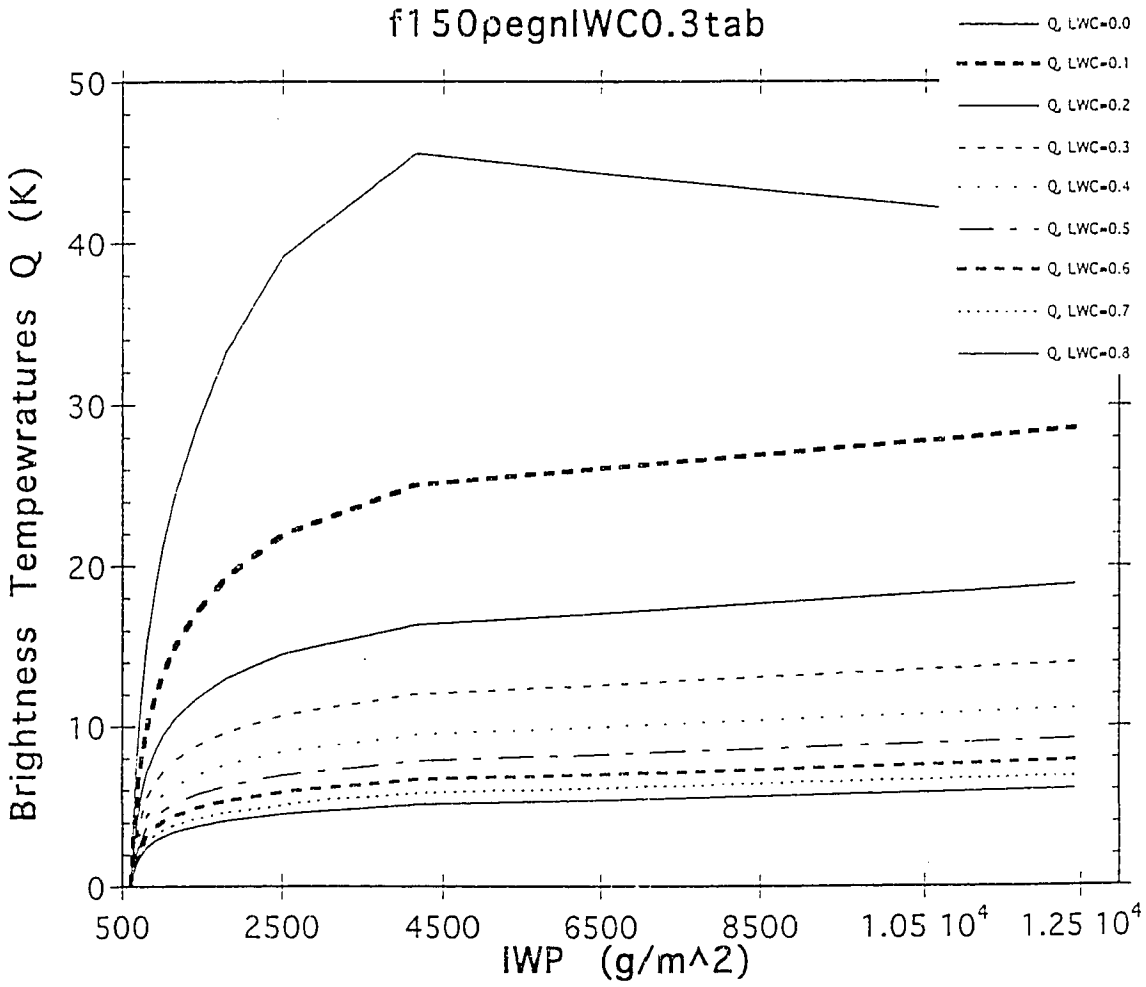

Figure 2.17: Brightness temperature Q as a function of ice water path (IWP) for some fixed liquid water path (LWP) values.

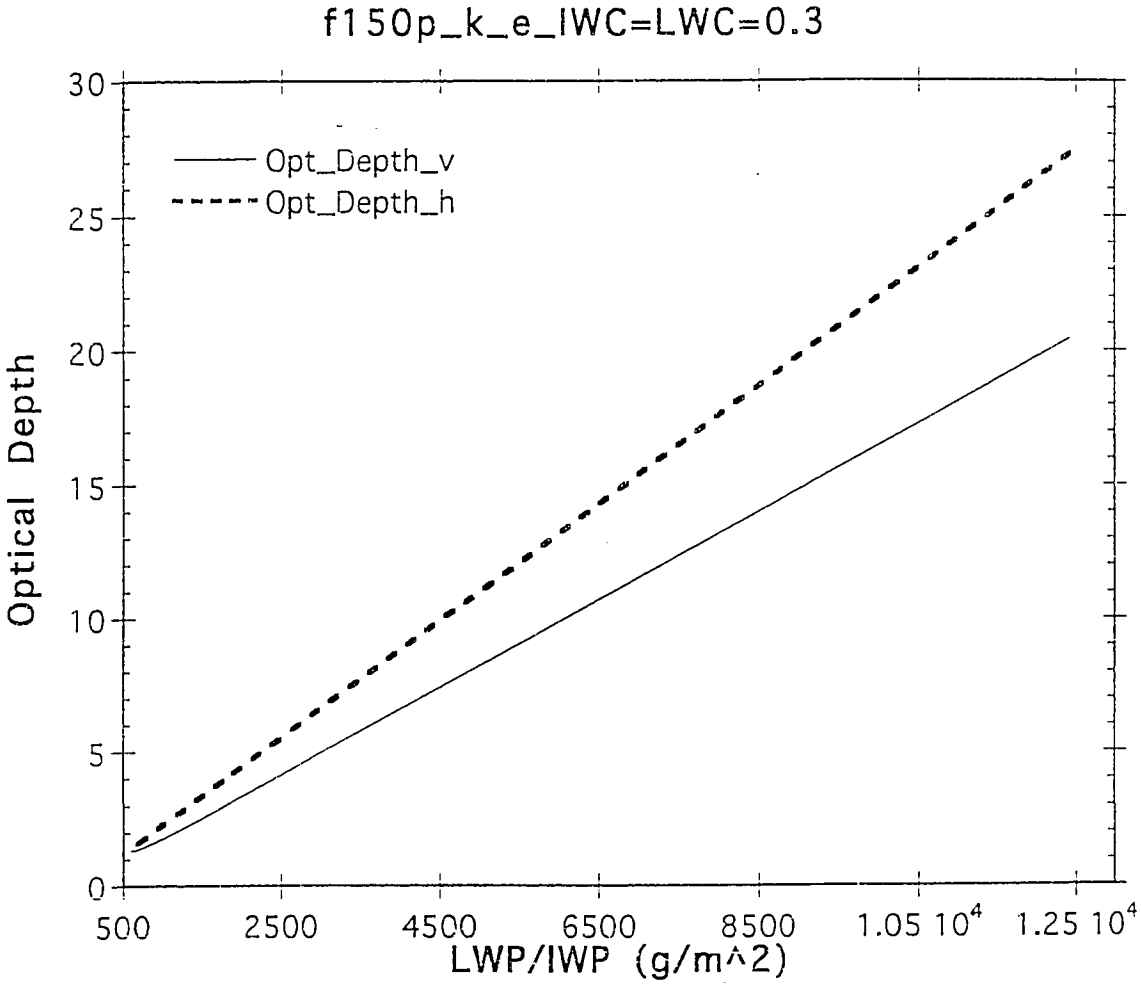

Figure 2.18: Optical depth as a function of LWP.

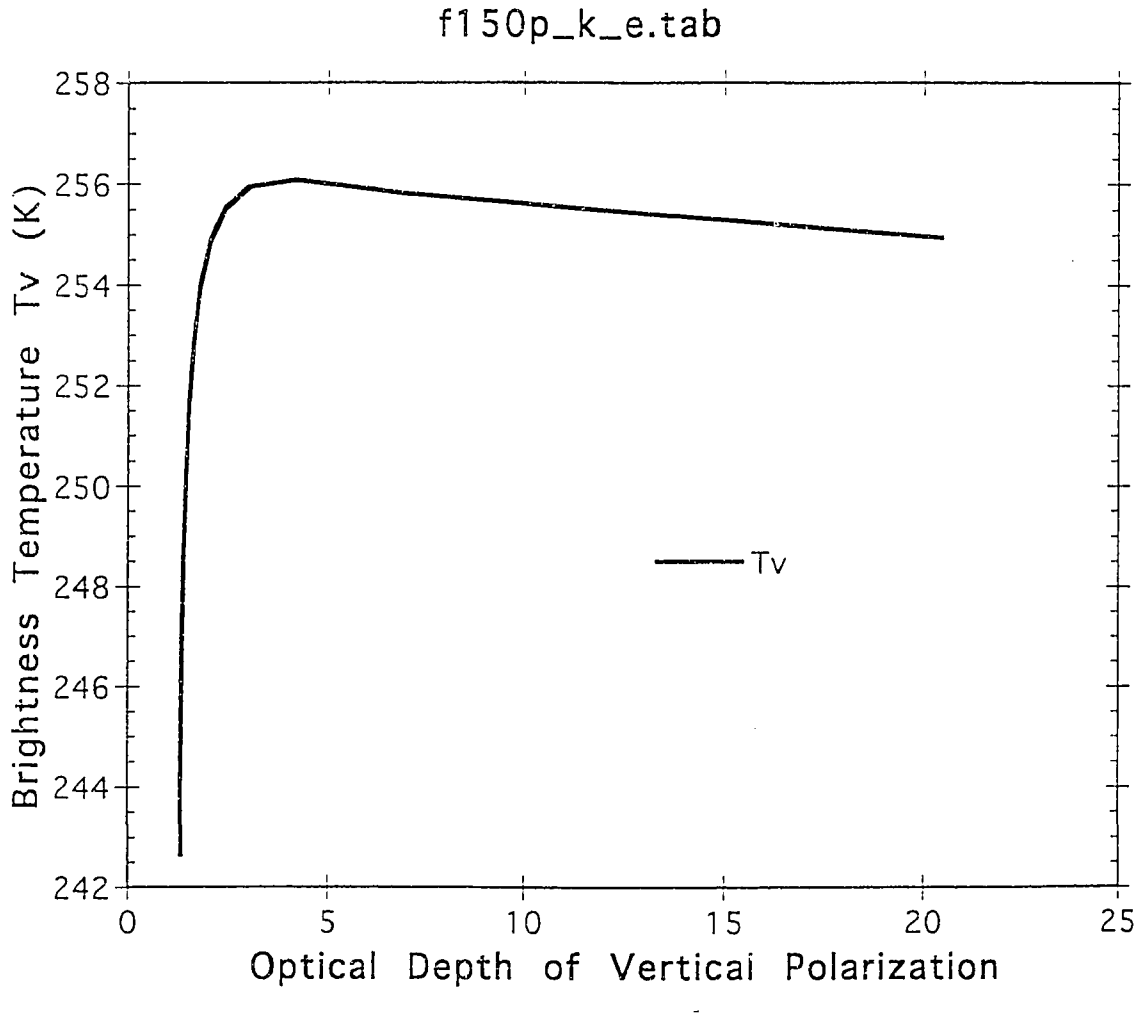

Figure 2.19: Vertically polarized brightness temperature as a function of optical depth.

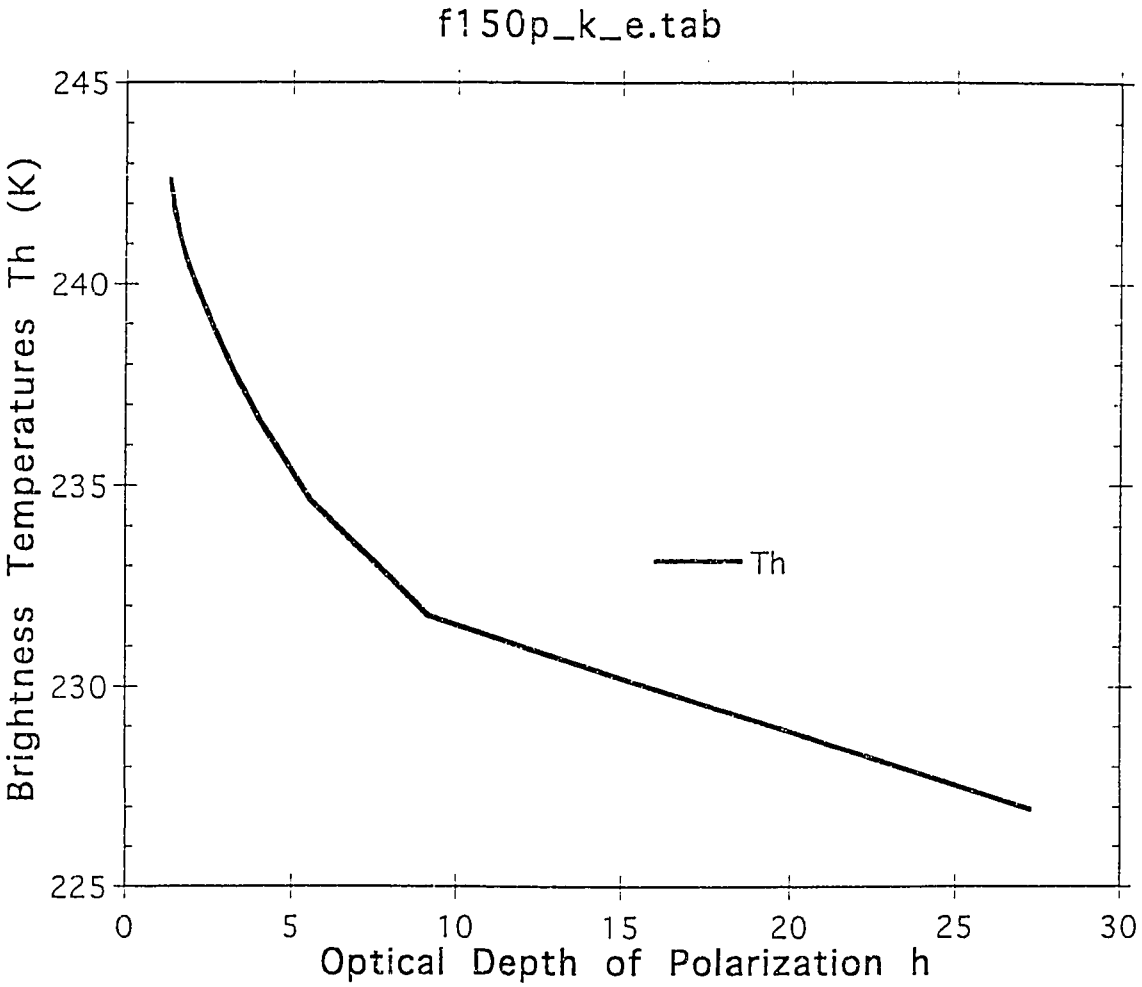

Figure 2.20: Horizontally polarized brightness temperature as a function of optical depth.

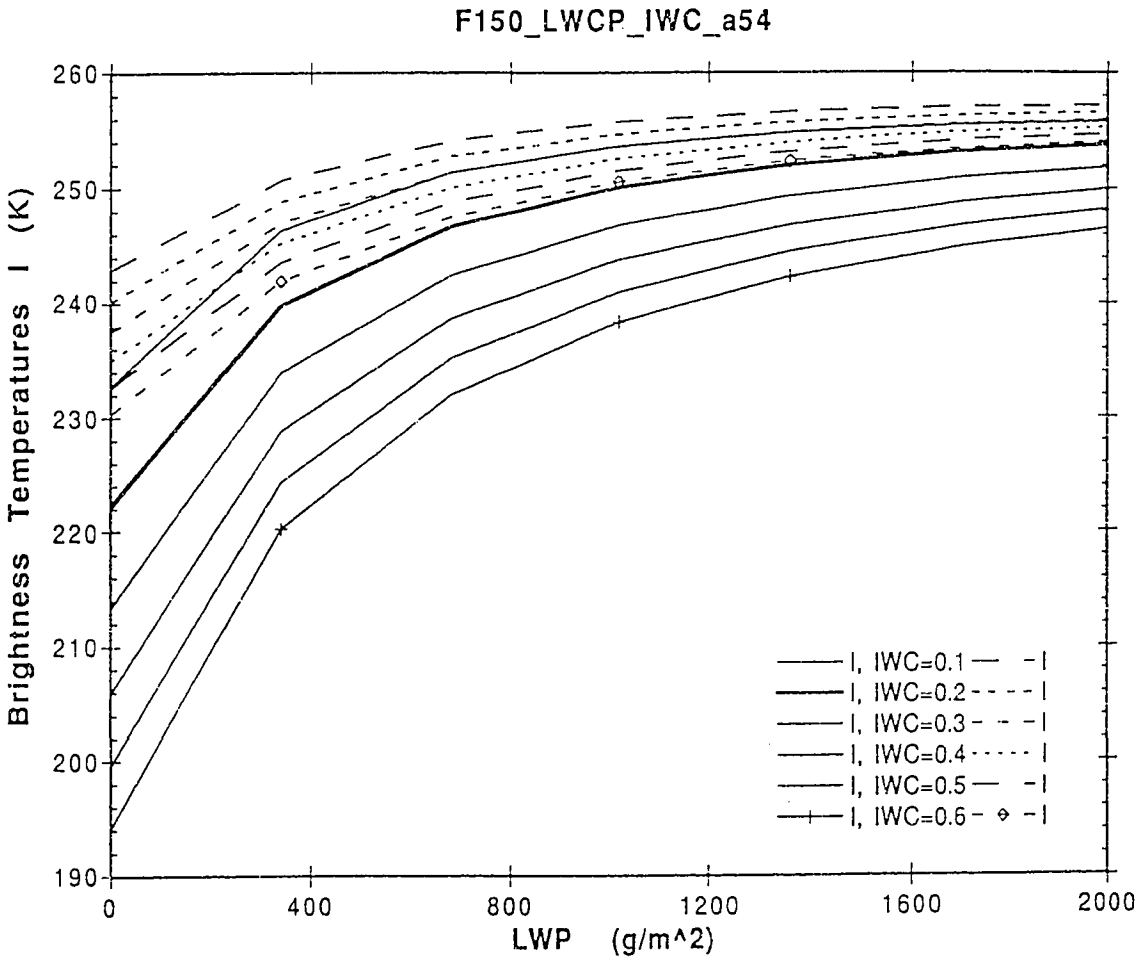

Figure 2.21: Brightness temperature I at 85 and 150 GHz as a function of liquid water path (LWP).

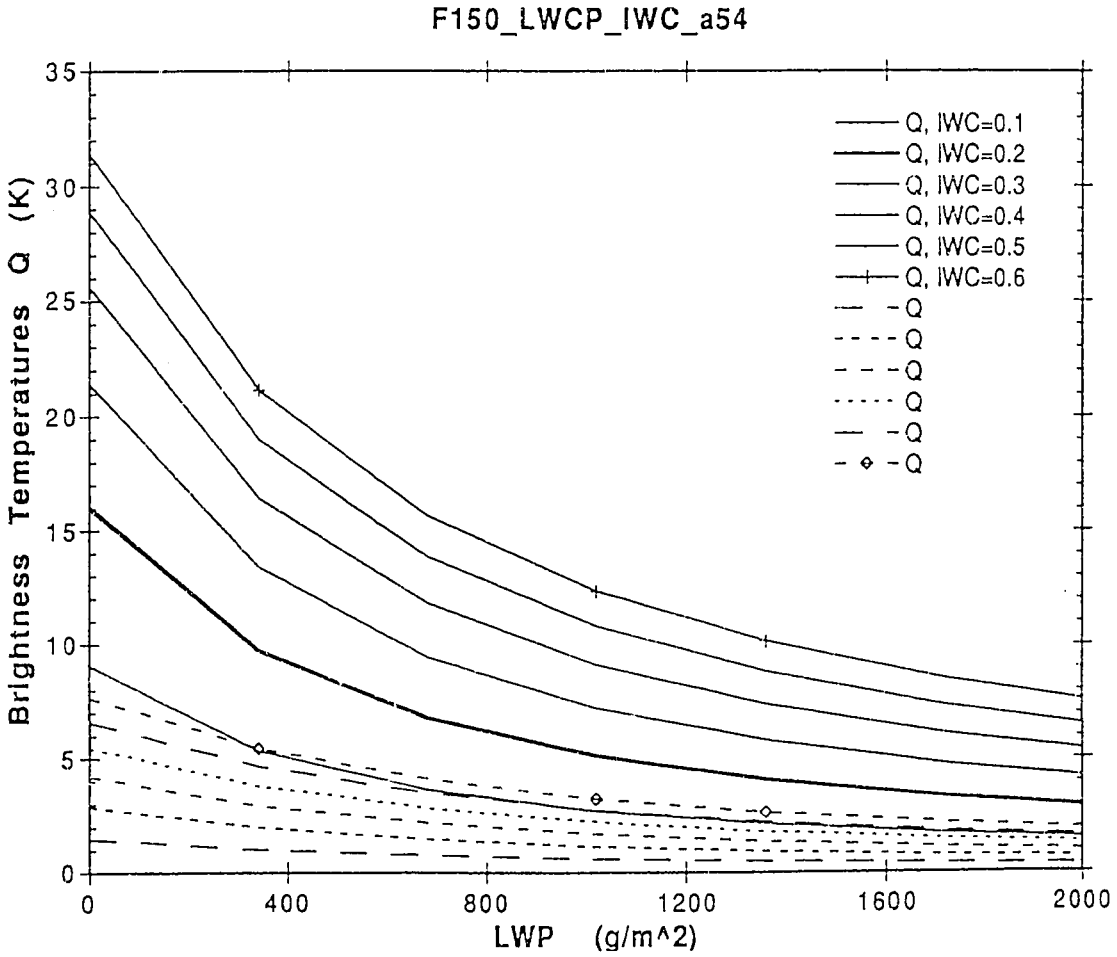

Figure 2.22: Brightness temperature Q at 85 and 150 GHz as a function of liquid water path (LWP).

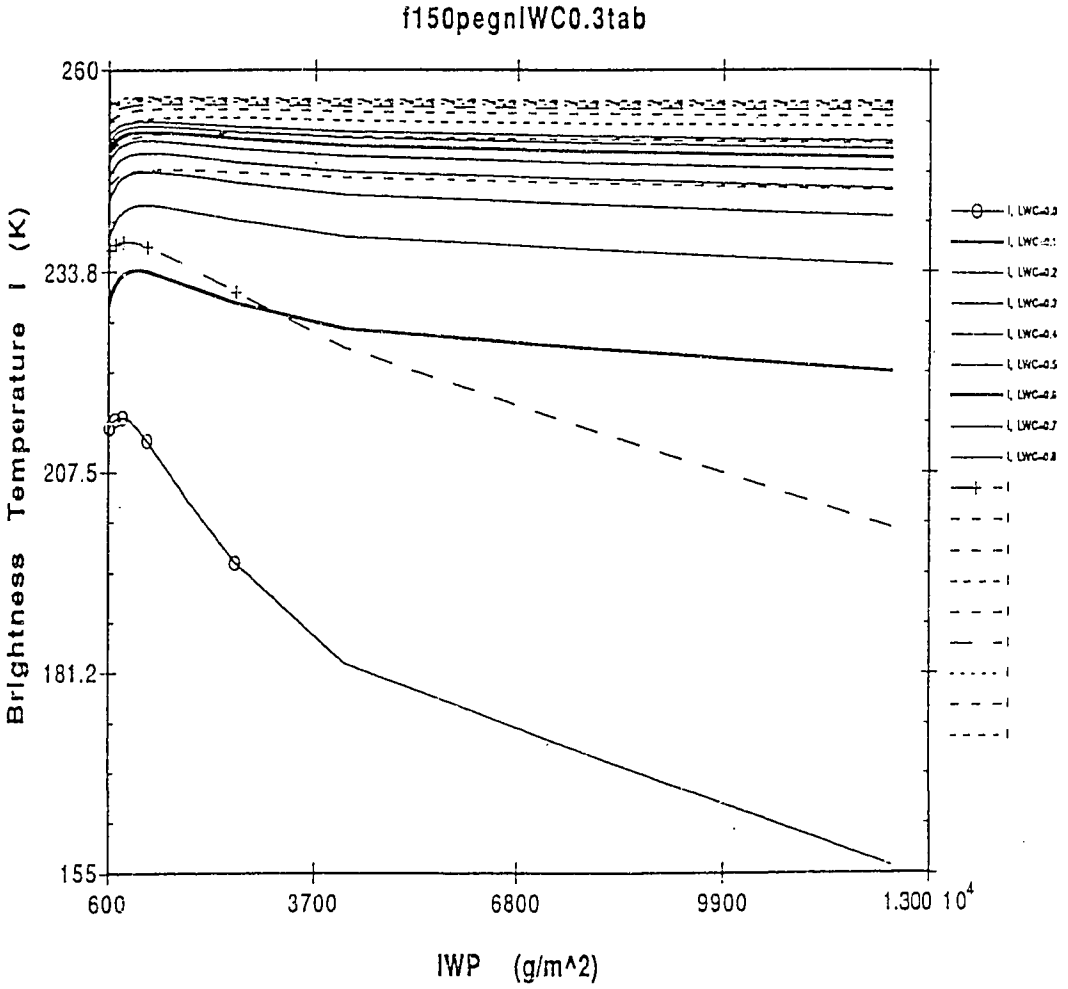

Figure 2.23: Brightness temperature I at 85 and 150 GHz as a function of ice water path (IWP).

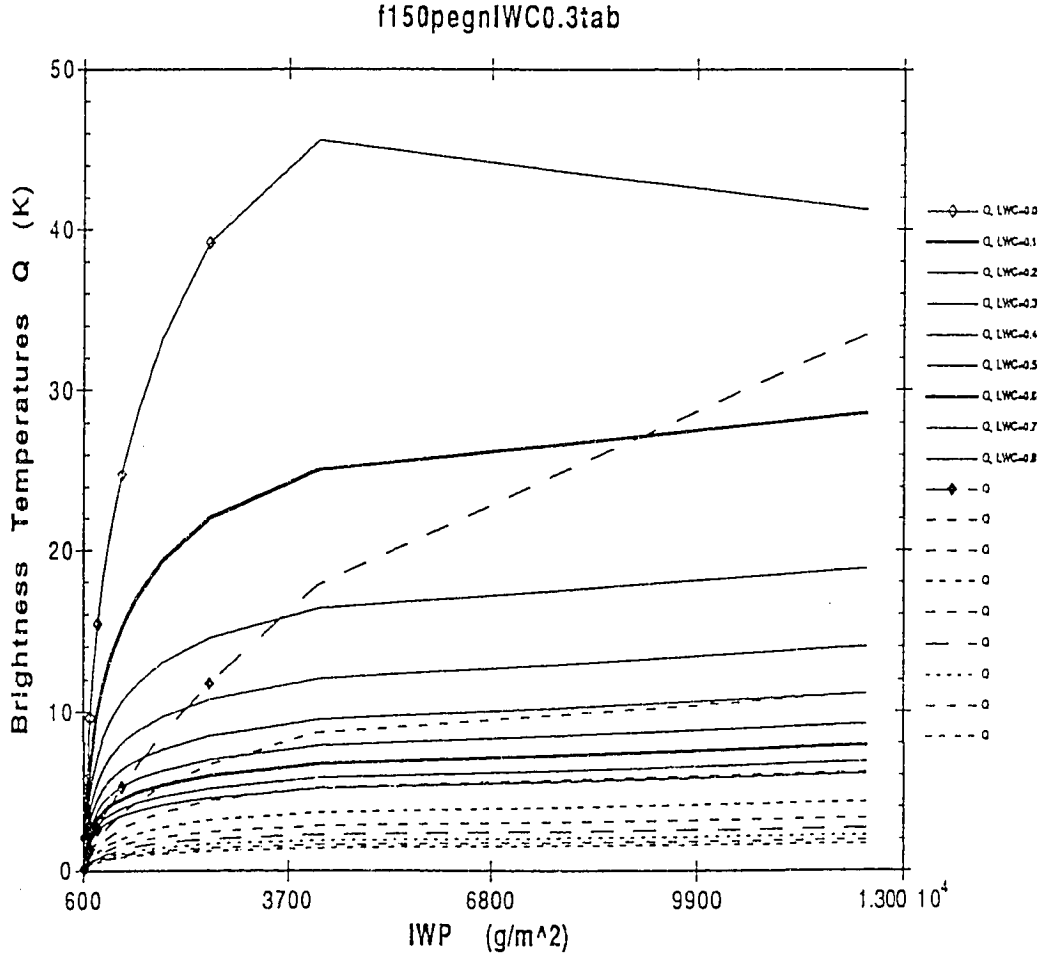

Figure 2.24: Brightness temperature Q at 85 and 150 GHz as a function of ice water path (IWP).

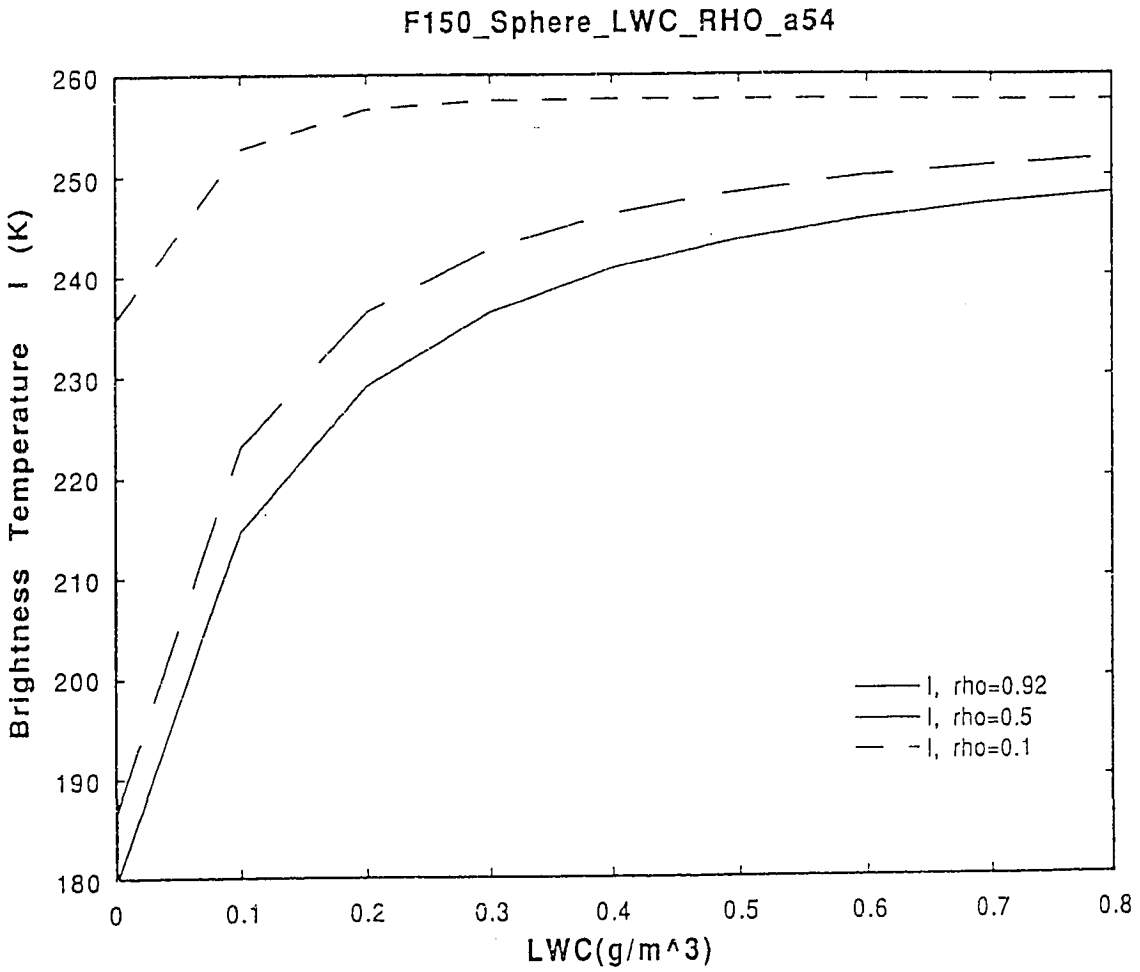

Figure 2.25: Brightness temperature I at 150 GHz as a function of liquid water path for different bulk density ρ.

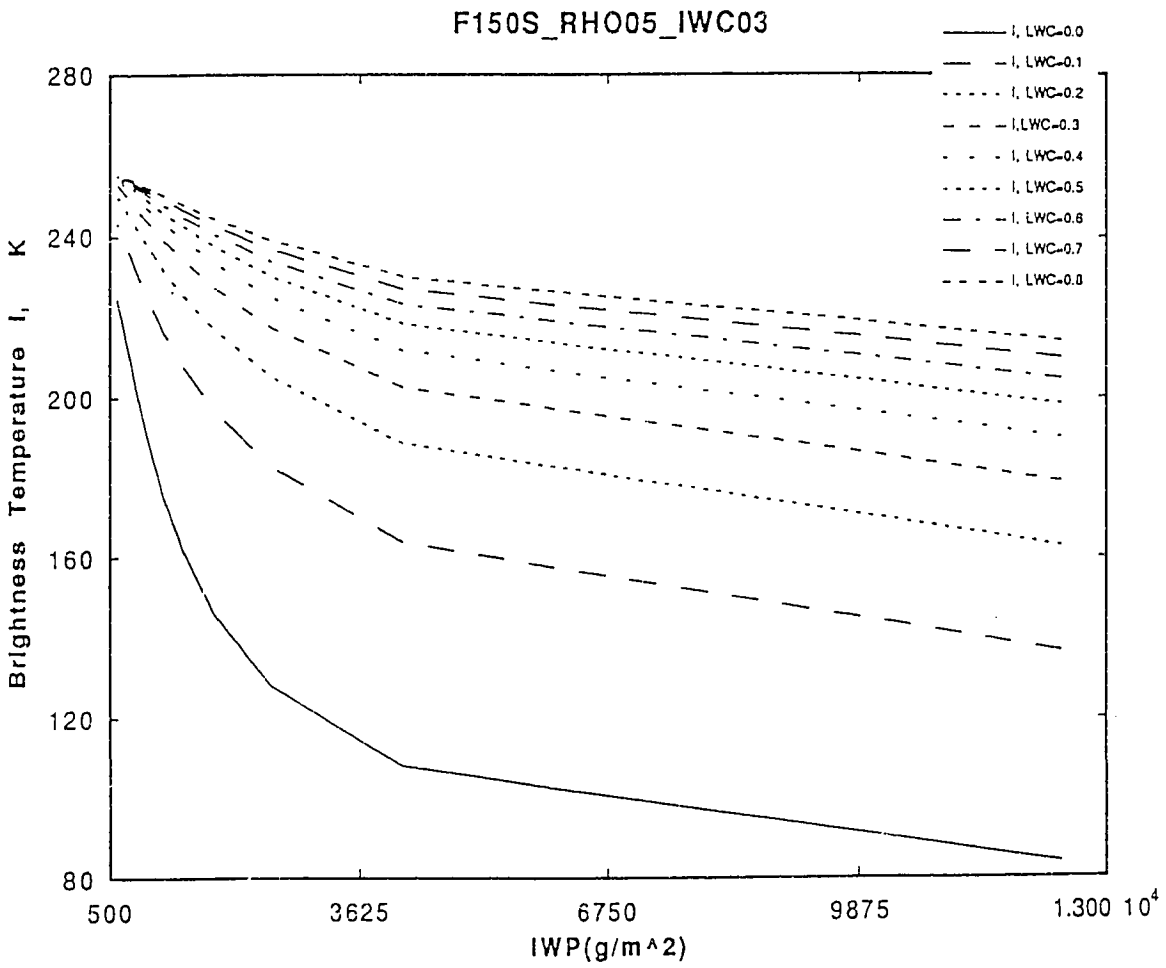

Figure 2.26: Brightness temperature I at 150 GHz as a function of ice water path for different liquid water path.

Chapter 3

GROUND-BASED RADIOMETER MODELING

3.1 Background on ground-based radiometry

Ground-based dual-channel radiometers have been used successfully for more than twenty years to monitor vapor and cloud water [77] [14] [20] [4]. Radiometric measurements of water vapor are about the same as, or better than, those of radiosondes [20]. Retrievals from ground-based radiometers are also used as a validation for satellite sensors. Unlike radiosondes, radiometers provide measurements unattendedly and continuously. Westwater [1978] and Staelin [1966] investigated the microwave spectrum of the atmosphere and its sensitivities to atmospheric components which provided the basis for most of the radiometric retrieval methods. In their investigation, statistical techniques were more or less utilized to deal with the variability of vapor and liquid components of atmospheric media both in time and space. Based on this, simple physical and linear/non-linear statistical algorithms were developed for ground-based radiometers to quantitatively retrieve water vapor and liquid cloud information under non-precipitation conditions [75]. Simple physical methods which oversimplify the real problems are less accurate than statistical ones, but statistical methods offer no insights to the physical processes and they provide little explanation as to the salient features of themselves. Most of the existing algorithms break down if the Mie scattering phenomenon due to ice and water drops is present because the earlier models are based on only an absorption phenomenon. For example, retrieval accuracies are marginal for cloud liquid much in excess of 3 mm [20] [76] [2].

Despite the successes of statistical models, comprehensive physical models are both possible and highly desirable [30] [31]. Retrieval techniques based on physical models are considered non-unique in nature. However, with the advent of remote sensing techniques, auxiliary measurements including measurements other than brightness temperatures can be incorporated to improve the confidence in remote sensing methods and to reduce ambiguities in the estimation of atmospheric quantities. Examples of auxiliary measurements are polarimetric and multi-frequency radiometer data, radar data, and Radio Acoustic Sounding System (RASS) data [5] [58] [45]. It is well known that variability of atmospheric structures

does not necessarily have the same degree of impact on the physics of radiative transfer. A comprehensive and accurate physical forward model which includes spatial distribution of atmospheric variables is crucial for quantitative investigation of sensitivities of each of the major atmospheric components such as vapor, cloud water and ice. Thus the forward model plays a key role in understanding microphysics and retrieval of the same.

The parameterization approach is a useful tool for comprehensive physical models of ill-posed problems as in the case of microwave radiometry [43]. It describes the state of the atmosphere using a limited number of unknowns, and lessens the ambiguities in inversion; it also provides a methodology for extracting information from radiometer measurements. To date, the majority of algorithms are based on more or less oversimplified forward (radiative transfer) models, which represent the relationship between brightness temperatures and environmental variables. Such an algorithm retrieves microphysical quantities using a set of algebraic expressions which are related to brightness temperatures. In this dissertation, we first developed a parametric radiative transfer model as a general forward model, which is tested against rigorous numerical models. The forward model is used to carry out a sensitivity study between brightness temperatures and environmental variables. Based on the sensitivity study, several different inverse models are impiemented using Artificial Neural Networks (ANN). Different from simple physical models, the parametric physical model deals with spatial distribution of absorption and scattering phenomenon of atmospheric constituents [43] [74]. Also, the sensitivity study is conducted using mean vertical profiles of input to the radiative transfer model. In the case of both forward and inverse models, the brightness temperatures (T_B) and microphysical parameters are coupled via non-linear functions. Moreover, auxiliary measurements are also integrated into retrieval algorithms to improve confidence in inferred quantities.

This chapter is organized as follows. Section 3.2 outlines the theoretical description of a parametric forward radiative transfer model. Temperature and vapor density profiles and the corresponding radiative properties of atmospheric gases are parameterized. A Millimeter-wave Propagation Model is used to obtain radiative properties of gases. Subsequently a complete radiative transfer model is developed by combining emission due to atmospheric gases and cloud liquid water and also scattering due to the ice layer. Parametric radiative transfer model results are compared with the rigorous numerical computations and actual brightness temperature measurements in Section 3.3. Also sensitivities of 20.6, 31.65 and 90 GHz brightness temperature to vapor, cloud water and ice are discussed. Based

on the sensitivity studies, a procedure to construct a neural network-based inverse model to retrieve vapor, liquid and ice is outlined in Section 3.4. Both explicit inversion and iterative inversion neural networks are considered. Section 3.5 shows the performances of explicit inversion and iterative inversion neural network models. It is shown that an iterative inversion model is better than the explicit inversion model.

3.2 Model Development

The main objective of passive microwave remote sensing is to extract quantitative micro-physical information using appropriate retrieval techniques. In principle, the development of a retrieval technique consists of several phases. The first phase is to adopt a cloud model which parameterizes realistic atmospheric and cloud structures relevant to the radiative transfer models. Parameterization leads to simplification of cumbersome vertical profile descriptions of temperature and vapor density . The second phase is to study the response of microwave emission and scattering characteristics to changes in cloud microphysics and/or environmental variables. This is known as the forward radiative transfer problem. Finally, an appropriate retrieval (or inverse) model is developed based on simulations and observations of the forward problem.

Atmosphere is characterized by high degrees of variability in time and space. A large number of unknowns are generally needed to describe the states of an atmosphere. With a limited number of measurements, a complete characterization of atmosphere is an ill-posed problem and no unique solution can be obtained. This is the main reason why statistical methods are widely used in radiometry models. On the other hand, it is not necessary, nor possible, to take enough measurements and determine the state of the atmosphere in much detail. Instead, the questions that should always be asked first are: what is the best way to parameterize the problem at hand, and what kind of information is retrievable from a given set of measurements. One of the practical solutions to these questions is a comprehensive physical model (forward model), which can offer a realistic description and detailed sensitivity studies of the remote sensing problem. As we know, a statistical retrieval algorithm is based on average states of atmospheric profile, and is of little help in the presence of precipitation. On the other hand, a physical model does not depend on geophysical location, but could have larger inherent biases if not calibrated properly. Thus, a combined physical and statistical model has the potential of providing better retrievals in all-weather conditions and extracting optimum information from measurements. For

the purpose of this dissertation, only statistical information of microphysics is used in our physical models. The procedure for the construction of a neural network based physical inverse model consists of the following steps:

(i) develop a parameterized forward model

(ii) conduct sensitivity studies using the parameterized model to identify the primary microphysical variables which are the most sensitive

(iii) generate three-channel brightness temperatures over the range of the microphysical variables

(iv) construct neural network based inverse models using the combinations of brightness temperature and microphysical variables.

3.2.1 Model Atmosphere

Supercooled liquid water (SLW) is known to cause aircraft icing, which continues to be one of the primary causes of aviation accidents, especially in winter weather situations [46]. A parametric radiative transfer model developed here focusses on the detection and estimation of supercooled water, vapor, and ice in winter clouds. The size of the supercooled liquid water (SLW) droplet ranges from tens to hundreds of micrometers. Temperatures for SLW can be as low as $-20°\ C$. Growth and formation of snow or other ice particles in a cloud quickly depletes supercooled cloud droplets. Thus the liquid water content (LWC) is very small in the presence of ice crystals [46]. In general, the cloud water profile does not have a regular shape and is difficult to determine. In-situ measurements by research aircraft show that the LWC usually increases slowly with height to a maximum value, then decreases quickly near cloud top [58]. This kind of liquid water profile information has been assimilated into liquid water and water vapor profiling using combined remote sensors. However, in this dissertation we use uniform profiles for both liquid and ice clouds for the following two reasons. First, our main focus is on the improvements of radiometry models, not the liquid water profiling. Second, without auxiliary measurements from other remote sensors like radar and RASS it is difficult to obtain vertical profiles. Also, the effects of a detailed liquid water profile are less significant in the simulated radiative transfer processes, which could be seen from sensitivity studies in a later section of this

dissertation. For the same reason, only the single layer cloud is used to simulate a variety of single and multilayer structures of liquid or ice clouds.

Drop size distribution of supercooled water drops is described by exponential or Gamma function. However, scattering due to liquid drop with sizes less than 0.1 mm is too small. Absorption or emission of water drops is proportional to mass per unit volume. In contrast to supercooled liquid water droplets, ice crystals have much larger sizes. Their shapes, bulk density, and size distributions have profound impacts on passive remote sensing. Since most of the ground-based radiometers do not measure polarimetric radiation from atmosphere, ice particle shapes are approximated as equivalent spheres. Their size distribution is assumed as modified Gamma size distributions [7],

$$n(r) = ar^{\alpha} \exp(-br^{\gamma}) \tag{3.1}$$

where, r is the radius of particles, α and γ are empirical constants, $n(r)$ is the number of particles per unit volume per unit radius. The value of parameters α and γ are set to two and one, respectively.

The parameters 'a' and 'b' are related to mode radius r_c, bulk density ρ and ice water content (IWC) as,

$$b = \frac{2}{r_c} \tag{3.2}$$

and

$$a = \frac{b^6}{160\pi\rho} IWC. \tag{3.3}$$

Radiosondes measure vertical profiles of relative humidity(or vapor density), pressure, temperature and dew point in the lower atmosphere. Figure 3.1 shows an example of a radiosonde measurement taken on 2 March 1991 at Platteville, Colorado. Derived quantities such as mixing ratio and vapor density are also shown. The environmental temperature decreases fairly smoothly with height except that there was a temperature inversion near the ground. Radiometry can also provide accurate temperature profile using oxygen emission ($\sim 60GHz$ and $118GHz$) bands. [5]. The temperature profile can be approximated by a linear relationship,

$$T(z) = T_A - \Gamma z \tag{3.4}$$

where T_A and Γ are effective near ground temperature and lapse rate, respectively. It should be noted that T_A and Γ are effective variables and are not necessarily equal to the actual near surface temperature and mean lapse rate, respectively [43]. For the forward problem, T_A and Γ can be directly calculated from radiosonde observations [44],

$$T_A = 4\bar{T} - 6T_\sigma \tag{3.5}$$

and

$$\Gamma = \frac{6}{H}[\bar{T} - 2T_\sigma] \tag{3.6}$$

where H is the thickness of the lower atmosphere. The parameters $\bar{T}$ and T_σ are the mean and first moment of the temperature profile,

$$\bar{T} = \frac{1}{H}\int_0^H T(z)dz \tag{3.7}$$

$$T_\sigma = \frac{1}{H^2}\int_0^H zT(z)dz. \tag{3.8}$$

In the case of a water vapor density profile, the scale height (H_v) and integrated water vapor column are used to characterize the profile. Often water vapor density profiles are approximated by exponential function [18],

$$\rho_v = \frac{V}{H_v}\exp(-\frac{z}{H}) \tag{3.9}$$

where V is integrated water vapor content

$$V = \int_0^H \rho_v dz \tag{3.10}$$

and H_v is water vapor scale height,

$$H_v = \frac{\int_0^H z\rho_v dz}{\int_0^H \rho_v dz}. \tag{3.11}$$

Although water vapor profiles measured by radiosondes rarely resemble exponential functions, vapor profiles are best approximated by equation (9) in the radiative transfer models of ground-based radiometers. The parameters V and H_v, which uniquely define equation (9), represent the maximum information that can be extracted or retrieved from

radiometer measurements. Some of the attempts to construct a water vapor profile using the integrated water vapor measurements by radiometers are not successful because the resulting profiles tend to be very smooth and lack detail [5].

Figure 3.2 shows an example profile of an atmosphere. The water vapor density profile is defined by integrated water vapor content and its scale height (Equation 11). The linear temperature profile is defined by equation (4). Assuming two cloud layers, the first layer is an all-liquid homogeneous cloud, and its profile is specified by cloud base height (H_b), cloud thickness (D), and liquid water content (LWC). The second is an ice cloud and is placed above the liquid cloud layer; its profile is defined in a similar way as a liquid cloud except that the ice particle mean size (r_e) and bulk density (ρ_v) are also specified. The liquid water content (LWC) and ice water content (IWC) in the two cloud layers are varied within their respective range of physical variations. The pressure profile, not plotted in Figure 3.2, is derived from surface pressure and the temperature profile is constructed by vertical integration of hydrostatic equation [18]. To avoid unreasonable atmosphere structure, the following constraints are imposed: (i) relative humidity must be less than or equal to 100% (ii) liquid cloud temperature must be between $-20°$ C and $5°$ C; (iii) ice cloud temperature must be below $0°$ C and (iv) the ice cloud base is above the liquid cloud top, consequently, co-existence of supercooled liquid water and ice particles is not allowed.

The above defined atmospheric profile is used to simulate brightness temperature data sets. In other words, radiosonde data are not needed for the simulation. Thus the construction of a retrieval algorithm is much more economical and faster, especially in a climatological area where radiosonde data are sparse. For example, each retrieval model developed in this dissertation was constructed in less than one week. It should to be noted that meteorological parameters defined above form a complete set of input to our physical model. No other intermediate optical parameters are used; therefore, any intermediate retrieval algorithm is unnecessary [43].

3.2.2 Forward Model

The radiative transfer process describes a nonlinear interaction between microwave emission, absorption, and scattering of atmospheric particles. In the atmosphere, microwave absorption and scattering are mainly due to molecular oxygen, water vapor, liquid water, and ice particles. Each of these atmospheric components has different optical properties and absorption spectrum. At frequencies below 100 GHz, water vapor absorption arises

from a weak resonant line at 22.235 GHz, and a relatively strong continuum absorption term. For oxygen, there are two strong resonant lines around 60 and 118 GHz. Away from these two oxygen absorption lines, dry air absorption is very weak. We use Liebe's unified Millimeter-wave Propagation Model (MPM) [35] to calculate the gaseous absorption. The MPM computes the microwave extinction coefficient of dry air and water vapor as a function of temperature, pressure, and humidity. In our model atmosphere, the water vapor profile is specified by vapor density as a function of height. To apply the MPM model, vapor density (ρ_v) is converted into a relative humidity profile (RH) using an empirical formula [35],

$$RH = \frac{e}{2.4089}(\frac{T}{300})^5 \times 10^{\frac{2950.2}{T}-10} \tag{3.12}$$

where T is the physical temperature, and e the partial water vapor pressure is given by the gas law

$$e = \rho_v RT. \tag{3.13}$$

The MPM model computes optical properties of water vapor and oxygen at the frequencies of interest. These optical properties are combined with absorption and scattering characteristics of cloud droplets and ice in the subsequent radiative transfer model. It is important to quantify accurately the gaseous absorption component because the scattered down-welling radiation by ice layer is modeled within a few Kelvin. In liquid cloud, absorption dominates over scattering. The Rayleigh approximation is applied to compute the absorption coefficients of cloud droplet ensembles. The Rayleigh absorption limit is valid for effective size $| n | k_0 a \ll 1$, where n is the refraction index of liquid water, k_0 the free space wave number, and a the radius of water droplets. In the Rayleigh limit, the absorption coefficient is linearly proportional to liquid water content and is independent of drop size distribution [65]. Although the effective size ($k_0 a$) of large liquid cloud droplets could exceed 0.2 or 0.3 at higher frequencies, the Rayleigh approximation is valid up to frequencies near 100 GHz due to the smallness of cloud droplets. The absorption rate of liquid water droplets increases with the decrease of physical temperature. Therefore, a liquid cloud with lower temperature looks brighter to the radiometers [43].

In the ice cloud, extinction is dominated by scattering and absorption is negligible. Ice particles are characterized by albedo close to unity with very little emission. The mean size of ice particles is in the order of sub-millimeters; ice crystals are usually non-spherical.

Since we are interested in zenith-looking T_B observations, ice particle shapes are modeled by equivalent spheres and their scattering properties are calculated using the Mie scattering theory. Modified Gamma size distribution is used to average scattering properties of ice particle ensembles. Refractive indices of liquid water droplet and ice particle at the needed frequencies are obtained by interpolating the tabulated values in [51]. The invariant embedding method is applied to find the solution to the radiative transfer equation [65]. In the invariant embedding method, an arbitrary vertical structure is divided into a number of homogeneous layers. In each layer, the radiative transfer equation is rewritten in the form of interaction principle by making use of the finite-difference and Gaussian quadrature integral formula. To integrate properties of all infinitesimal layers, the linear nature of the interaction principle is used repeatedly. The formulation of radiative transfer in the form of the reflection and transmission matrices and emission source vectors of the whole medium also includes the boundary conditions of the transfer equations. In this way, the outgoing radiation and the radiation field inside the medium can be obtained from the interaction principle. We use land surface with an emissivity of 0.95, and let the ground temperature be equal to effective near surface temperature. At the top boundary, the cosmic radiation of 2.7 K is incident from above.

The theoretical description of absorption spectra of atmospheric constituents is incomplete. For example, the physical basis of absorption of water vapor continuum is not yet completely understood. Also, in the case of the liquid water absorption rate, we found that Liebe's MPM model differs from the Rayleigh approximation by about 1 to 6 percent. These discrepancies introduce biases into the radiative transfer model results. Hence, a good calibration is essential to eliminate the inherent bias. One simple way to calibrate a physical model is to compare it with some well calibrated statistical algorithms, such as NOAA's ground-based dual-channel radiometer retrieval results [15]. The calibration procedure is described in later section of this chapter.

In summary, we have outlined the development of a parametric radiative transfer model for the simulation of brightness temperature of the model atmosphere with vertical distributed water vapor, temperature, liquid and ice clouds. The model parameters include frequency of interest, integrated water vapor and vapor scale height, liquid cloud base and top, liquid water path, ice cloud base and top, ice water path, ice particle mean size and bulk density, and effective near surface temperature and lapse rate. As outlined above, profiles of temperature and water vapor are parameterized and corresponding optical depths

are computed using Liebe's MPM model. These optical properties are combined with the radiative properties of liquid and ice cloud. The resulting radiative transfer equation is solved by the invariant embedding method. The major advantage of the parameterized radiative transfer model is that a detailed description of temperature and vapor density is specified by a finite number of distinctive parameters.

3.3 Parametric Model Testing and Sensitivity Studies

To validate the performance of a parametric radiative transfer model the results are compared against the numerical integration method and radiometer measurements. The first test is based on radiosonde data plotted on Figure 3.1. From sounding data, it is found that the integrated water vapor and vapor scale height are 0.85 cm and 1.82 km respectively. The effective near ground temperature is 273.86° K and lapse rate is 5.986° K/km. For the purpose of model testing, cloud liquid and ice amount are assumed to be zero in this case. The results using rigorous radiative transfer model are 11.54° K, 10.67° K, and 28.95° K at 20.6, 31.65, and 90 GHz, respectively. These values are very close to the parameterized model simulation results, which are 11.36° K, 10.60° K, and 28.98° K.

In the second test, the observations made by the NOAA radiometer are used. NOAA ground-based dual-channel radiometers measure downwelling radiation in the zenith direction at 20.6 and 31.65 GHz. One of the facilities has an additional 90 GHz channel. The 20.6 GHz channel, which is offset from a weak water vapor resonant line at 22.235 GHz, senses mainly the integrated vapor and is less sensitive to the pressure and water vapor profiles. The 31.65 GHz is primarily sensitive to liquid water and the 90 GHz channel is in the scattering regime. On 2 March 1991, the NOAA radiometer measured 0.81 cm integrated water vapor and 0.018 mm liquid water. Cloud base height at 0.67 km was detected by a ceilometer; and the cloud top was estimate to be 0.85 km by the adiabatic approximation [58]. The corresponding measured brightness temperatures at the three channels are 16.04° K, 13.93° K, and 32.47° K. Using NOAA radiometer's retrieved vapor and liquid values, the corresponding parameterized model predicted brightness temperatures are 13.50° K, 11.80° K, and 32.24° K. The parameterized physical model results differ slightly from the actual observations and these differences are subsequently used to calibrate the neural network inversion models as explained in later sections.

The radiative transfer models which deal with the scattering phenomenon, generally use one of the "Standard Atmospheric" profiles to account for gaseous emission components

[70] [41]. Using a parameterization approach, we have not only simplified the process of solving radiative transfer equations but also preserved the main features of temperature and humidity profiles. The parameterized radiative model is initialized by thirteen different variables as listed in Table 3.1. With a limited number of measurements from radiometers, it is difficult to invert this parametric model. Simulations might help to gain some insights into the dominant physical process and identify the signatures of required environment variable in terms of brightness temperatures. But equally or more important is the sensitivities of brightness temperature T_B at a given channel to a particular parameter p_i, namely $\partial T_B / \partial p_i$ [44]. To describe an implicit function, three pieces of information are needed and they are its value, derivative, and dynamic range. A sensitivity study can estimate the impact of each of the environmental variable on the radiative transfer results and thus identify the significant environmental parameters for the problem at hand. Non-linearity in the model is identified by the dynamic nature of the sensitivity values, well represented by variation in sensitivities. To the contrary the sensitivities are constant for linear retrieval algorithms. Non-linearity in the model inversion is easily implemented with the aid of neural networks; the retrieval is problematic only if the sensitivities approach zero. For the development of an inverse model, it is also more important to identify insignificant parameters that are usually kept unchanged. Some of the insignificant parameters are treated as noise in both physical and statistical retrieval algorithms and they are not used in the model inversion procedure.

The parametric radiative transfer model is nothing more than a function defined in multi-dimension space. The basic idea of the sensitivity study is to cut the space along each dimension around a base state, and observe the behavior of the function on those cuts. A base state is primarily determined by mean-state parameters of the above mentioned thirteen variables. In general, results of sensitivity studies are base state dependent. In many applications, one can narrow down the parameter ranges and a large variation around the base state may not be necessary.

The sensitivity study was conducted at three frequency channels: 20.6, 32.65, and 90 GHz. A base state is chosen according to Denver winter time climate; namely, T_A = 0° C, Γ = 6.5 K/km, V =0.8 cm, H_v = 2 km, P_0 = 84 kPa, LWP = 200 g/m^2, D = 1 km, H_b = 1.5 km, IWP = 200 g/m^2, D_{ice} = 1 km, H_{bice} = 4.0 km, ρ = 0.92 g/cm^3, and r_e = 0.05 cm. The parametric model is examined in the neighborhood of this base state, which is referred as Base state 1.

Figure 3.3 shows sensitivities of brightness temperature at each channel with respect to the integrated water vapor ($\partial T_B/\partial V$). In the range of interests, all three channels exhibit almost linear characteristics. Sensitivities are almost constant over the range of V, and they are 7.0, 4.3, and 16.3 K/cm at 20.6, 31.65, and 90 GHz channels, respectively. As expected, the 20.6 GHz channel is much less sensitive to integrated water vapor than 90 GHz channel, although 20.6GHz is close to the water vapor resonance line at 22.235 GHz but it is more sensitive than the 31.65 GHz channel. Nevertheless, every channel shows certain sensitivity to integrated water vapor. As depicted in Figure 3.4, the microwave brightness temperatures are much more sensitive to cloud liquid water than to vapor. Sensitivities at 20.6 and 31.65 GHz channels are almost constant. The 90 GHz response is in a non-linear regime and its channel sensitivity drops quickly with the increase of the liquid water path. It is interesting to note that the 90 GHz channel will eventually saturate and loses its sensitivity to liquid water; however, a lower frequency such as the 31.65 GHz channel is still sensitive at these high LWP. Figure 3.5 illustrates the brightness temperature sensitivity to the ice water path. The relationship is approximately linear over the range of interests. Ice cloud is optically thinner by at least a factor of two than liquid cloud around 90 GHz [3]. It is interesting to note that all three channels exhibit some sensitivities to ice path. An increase in ice water path by about 1 kg/m^2 elevates the brightness temperature by about 5 K at 20.6 GHz, 14 K at 31.65 GHz, and 64.5 K at 90 GHz.

Brightness temperature is also very sensitive to bulk density and mean size of the ice particles as shown in Figures 3.6 and 3.7. The sensitivity at 90 GHz increases rapidly with the increase of bulk density up to 0.7 g/cm^3, and then it decreases until bulk density reaches its maximum value 0.92 g/cm^3. However, the 90 GHz T_B values are more sensitive to IWP than to LWP. The sensitivity signatures in Figures 3.6 and 3.7 indicate strong non-linearity and can be explained as follows. The key to understanding these sensitivity signatures is that the IWP is constant in all our sensitivity calculations, except in cases where we studied sensitivities to IWP itself. Downwelling brightness temperatures increase with the optical depth of the ice layer. Both mode radius and number concentration will increase the optical depth. However, for a given IWP and bulk density, an increase in mode radius will result in decrease of number concentration. As a result, the optical depth is a trade off between ice particle size and number concentration. As shown in Figure 3.7, T_B sensitivity at 20 and 31 GHz channels increases first then decreases,

but these sensitivities are always positive in the range of interests. This indicates that T_{B20} and T_{B31} increase with r_e in that range. For the 90 GHz channel, the sensitivity decreases monotonically from positive to negative. Hence, T_{B90} will increase initially and then decreases as r_e increases.

The impact of vapor scale height (H_v) on brightness temperature sensitivity is shown in Figure 3.8. Changes in H_v affects both mean water vapor column temperature and vapor partial pressure which will in turn change the vapor mean radiation temperature, strength of vapor continuum absorption, and width of the absorption line at 22.2 GHz. As a net effect, the sensitivity decreases with H_v and becomes slightly negative for H_v greater than $1.5Km$. The 90 GHz channel shows the greatest sensitive to H_v, and 31.65 GHz is the least sensitive channel. But the sensitivity to H_v is relatively small at all three channels.

Brightness temperature sensitivities to the rest of the model parameters, namely, H_b, T_A, Γ, D, and D_i are also studied. It is found that these parameters are less sensitive when compared to that of V, LWP, IWP, ρ, and r_e. For some parameters, such as the thickness of liquid and ice cloud, the sensitivity is close to or below radiometer noise level, which indicates that they cannot be retrieved by radiometer measurements alone.

The sensitivity of brightness temperature is quantitatively summarized in Table 3.1 for the case studied. Thirteen model parameters are classified into three classes according to their sensitivities to brightness temperature, namely high, medium, and low. This kind of information or classification is very helpful when we construct physical retrieval models. In principle, sensitive parameters should be included in the retrieval algorithm; otherwise they could introduce a large bias or pose strong limitations on the retrieval method. The procedure to incorporate all sensitive parameters into the inverse model is determined primarily by available measurements. If the number of measurements is larger than that of most sensitive physical parameters, it might be possible to include some of the slightly sensitive parameters and fix the rest of the variables at their meteorological mean values. For the insensitive variables, mean values should be used and their inclusion in the retrieval model will only complicate the algorithm.

Table 3.1 helps us to understand the design criteria for ground-based radiometers. For example, according to sensitivities of brightness temperature to V and LWP in Table 3.1, the 20.6 and 31.65 GHz is the best combination for dual-channel ground-based radiometry than any other combinations. NOAA's technique rely primarily on this key idea. The popular NOAA' linear statistical retrieval algorithm is based on long term radiosonde

Table 3.1: Model Sensitivity

Parameter(p)	Base State	$\frac{\partial T_{B20}}{\partial p}$	$\frac{\partial T_{B31}}{\partial p}$	$\frac{\partial T_{B90}}{\partial p}$	$Unit$	Sensitivity class
V	0.8 cm	7.0	4.3	16.3	K/cm	High
LWP	0.2 mm	31.0	62.5	199.0	K/mm	High
IWP	0.2 mm	5.0	14.0	64.5	K/mm	High
P_0	84.0 KPa	0.06	0.13	0.27	K/KPa	Medium
ρ	0.92 g/cm^3	1.49	4.5	17.5	$K\ cm^3/g$	Medium
r_c	0.05 cm	20.0	33.0	51.0	K/cm	Medium
D	1.0 km	0.6	1.0	0.2	K/km	Low
D_i	1.0 km	−0.05	−0.05	−0.15	K/km	Low
H_{bi}	4.0 km	−0.05	−0.05	−0.3	K/km	Low
Γ	6.5 $°C/km$	0.25	0.7	−0.2	$K\ km/C$	Low
T_A	0°C	−0.16	−0.3	0.2	K/C	Low
H_b	1.5 km	1.0	1.7	0.3	K/km	Low
H_v	2.0 km	−0.8	−0.6	−2.1	K/km	Low

Table 3.2: Sensitivity Comparison Unit: K/cm

	$\frac{\partial T_{B20}}{\partial V}$	$\frac{\partial T_{B31}}{\partial V}$	$\frac{\partial T_{B20}}{\partial LWP}$	$\frac{\partial T_{B31}}{\partial LWP}$
NOAA Model	11.723	4.761	245.07	561.50
State 1	7.0	4.3	310	625
Difference (%)	40.3	9.6	-26.5	-11.3
State 2	10.038	4.23	283.24	560.50
Difference (%)	14.4	11.1	15.6	0.2

observation. A typical dual-channel algorithm for Denver area is given by [17] [20],

$$V = -0.1705 + 0.10368T_{B20.6} - 0.04526T_{B31.65} \tag{3.14}$$

$$L = -0.0132 - 0.0008791T_{B20.6} + 0.002165T_{B31.65} \ . \tag{3.15}$$

Unlike in physical models, its retrieval coefficients change with climatological conditions (locations and seasons). It is interesting to compare the brightness temperature sensitivity derived from NOAA's inverse model and sensitivities computed using the parameterized radiative transfer model. Because the scattering due to ice cloud is ignored in NOAA's model, the sensitivity of physical model is calculated again around following base state 2: T_A = 273 K, Γ = 6.5 K/km, V = 0.5 cm, H_v = 2 km, P_0 = 84 kPa, LWP = 0.0 g/m^2, D = 1 km, H_b = 1 km. The ice water path is kept at zero, i.e. IWP = 0.0 g/m^2. The sensitivities from both models are compared in Figures 3.9 and 3.10. The results show that the linear relationship between brightness temperature and integrated water vapor is a very good approximation. But for liquid water, the 31.65 GHz channel exhibits considerable non-linearity. The sensitivity differences between our physical and NOAA's linear statistical model is roughly estimated as shown in Table 3.2. Base state 1 contains both ice and liquid clouds. In this case the physical model sensitivity deviates clearly from NOAA's results. In principle, NOAA's model should be accurate around the base state because their model is developed for ice free conditions.

In the absence of ice, the maximum difference between NOAA's value and our physical model is 15%. The difference is small, especially when one considers the accuracy of the linear statistical model. Hogg compared the statistical model results and their

Table 3.3: Three Channel Radiometer Sensitivities Unit: K/cm

	T_{B20}	T_{B31}	T_{B90}
Vapor	7.0	4.3	16.3
LWP	310	625	1990
IWP	5.0	140	645

corresponding radiosonde measurements taken at Denver in six months. He found that the rms difference between them is 1.7 mm for integrated water vapor [20]. Wei did similar investigation on radiometer data collected at Shearwater, Nova Scotia, Canada [73]. He assessed similar rms deviations for integrated water vapor and liquid water to be 0.867 mm and 0.159 mm respectively, which are about 8.7% and 37% of the overall average vapor and liquid. The radiosonde itself is not a very accurate standard to compare with. Its performance is poor for relative humidity below 20% and above 90%, and reasonable otherwise [54].

We have analyzed sensitivities of the three-channel radiometer for a number of atmospheric parameters. Based on these studies, the most sensitive variables are identified and they are V, LWP, IWP and r_e. Since the primary objective is to retrieve V, LWP and IWP, sensitivities of these parameters for all of the three-channel are tabulated in Table 3.3. The 20 GHz channel is affected by both vapor and liquid. Hence, NOAA's dual-channel (20, 31 GHz) technique outperforms any single channel (20 GHz) method by retrieving vapor and liquid simultaneously. If we are interested in water vapor and liquid water retrievals in the absence of ice then, inclusion of the 90 GHz channel should not improve cloud liquid estimation. In the presence of IWP, the 30 GHz T_B is modulated by scattering ice layer. As expected the 90 GHz channel is sensitive to all of the three components, namely, V, LWP and IWP. The three-channel radiometer might be able to retrieve LWP with improved accuracy by taking into account ice layer scattering. Estimation of ice critically depends on precise estimations of V and LWP. Hence, both emission and scattering frequencies are necessary to retrieve ice information.

3.4 *Neural Network Modeling*

Recently, there has been increasing interest in using an artificial neural network to retrieve geophysical information from the passive microwave remote sensing measurements [61] [6]. Neural networks can handle non-linearity in the remote sensing problems. It is also relatively easier for neural networks to incorporate auxiliary measurements and/or information into the retrieval algorithms. Here, we apply neural network techniques to the multiparametric retrieval from multifrequency T_B observations. We briefly discuss one of the common neural network models, namely, the feedforward Multilayer Perceptron (MLP), then describe a procedure to construct data driven forward and inverse remote sensing models using MLP's.

3.4.1 *Feedforward Multilayer Perceptrons*

Figure 3.11 illustrates the basic structure of a feed-forward MLP. The network can be described as a parameterized mapping from an input vector $a(0)$ to an output vector $a(L)$;

$$\bar{a}(L) = \phi(\bar{W}, \bar{a}(0)) \tag{3.16}$$

where $\bar{W}$ is the vector of weights, and L is the number of layers in the network. Passing a vector forward to the output layer consists of taking the inner product of the vector with the incoming weight vectors, and feeding the inner product into the nonlinear function of neurons. In the classical paradigm, training is the procedure of changing the weights to reduce the discrepancy between a target vector and the actual output vector $\bar{a}(L)$. The discrepancy, which is also called cost function, can take any form of a differentiable function. This offers us many ways to impose constraints and prior knowledge. Most often, this discrepancy is defined as sum squared error at the output units ($\bar{t}$) of the network, denoted by $\bar{E}$,

$$\bar{E} = \frac{1}{2}(\bar{t} - \bar{a}(L))^T(\bar{t} - \bar{a}(L)). \tag{3.17}$$

Backpropagation is an algorithm for computing gradient of the cost functional to minimize the cost. This is achieved by using the chain rule to differentiate cost function E with respect to the weight vector W then updating the weights iteratively [52]:

$$\bar{W}^{(n+1)} \longleftarrow \bar{W}^{(n)} - \eta \frac{\partial \bar{E}}{\partial \bar{W}^{(n)}} + \mu \Delta \bar{W}^{(n-1)} \tag{3.18}$$

$\bar{W}^{(n-1)} = \bar{W}^{(n)} - \bar{W}^{(n-1)}$, η and μ are learning rate and momentum parameter respectively. Once trained, an MLP can approximate an arbitrary input-output relationship [21].

3.4.2 Construction of a Forward and Inverse Model Using MLP

The general approach to solving inverse problem using MLP's is a two-phase procedure. In the first phase, a set of data generated from the physical radiative transfer model is used to train a data driven neural network model that maps from parameter space ($\bar{\mathbf{p}}$) to measurement space ($\bar{\mathbf{m}}$). In other words, a causal relationship (ϕ) defined by the radiative transfer model $\mathbf{m} = \phi(\mathbf{p})$ is copied by the neural network to obtain a forward model $\hat{\mathbf{m}} = \hat{\phi}(\mathbf{p})$ as an approximation. It takes meticulous effort to train the MLP; but once trained, a forward model can process the data speedily and accurately. More importantly, a forward model contains gradient information of measurements with respect to parameters. In the second phase, an inverse model is constructed based on this gradient information which provides us a way of searching solutions in parameter space for a given measurement. This information may not be crucial when the inverse relationship is also causal.

In general, neural networks have little difficulty to learn forward problems since those mappings are unique. There are two important issues for a data driven forward neural network model (or forward model). One is how accurately the training and testing data set represents the situation being studied. This is a problem of sampling techniques. When the number of input units is too large, a favorite technique could be to create a grid of input variables and select points randomly in the grid. Otherwise, uniform sampling can be used. To evaluate a forward model, one can apply cross validation, training with one data set and testing with a different set, or test the model against independent synthetic data [6]. The second issue is how well the neural network can generalize or interpolate the training data. Since neural networks can approximate any function, their flexibility works against generalizations when the training data is noisy. For the problems studied in this dissertation, noise free training data is generated using our physical radiative transfer model. It is also found that a cross validation or a test against independent synthetic data is generally unnecessary.

One simple way to invert a neural network forward model is to train an inverse model by reversing the roles of the inputs and outputs. This method, known as explicit

inversion, is widely used in remote sensing and in many other areas. Unfortunately, the radiative transfer model (or forward model) is characterized by many-to-one mapping. Although the mapping is uniquely determined by environment variables, inversion of such a forward model suffers one-to-many mapping. Explicit inverse method resolves such a mapping problem by averaging across the multiple targets. Specifically, if the cost function takes the form of sum-of-squared error, and one set of brightness temperature measurements corresponds to a number of environment states, the explicit inverse model will find an environment state which has minimum total Euclidean distance to all the corresponding environment states [6]. Furthermore, involved in the forward model are not only many-to-one functions, but also the geometry of the parameter space. As shown in Figure 3.12, the inverse image of the forward model (nonlinear transformation) is not necessarily convex. The average point in a non-convex set could be outside the set [25]. As a result, an average of many possible inversions may not be even an inversion. If one uses an explicit inverse model and retrieves certain atmospheric state for a given brightness temperature measurement, then feeds this retrieval into the forward model, the simulated brightness temperature could be different from the actual measurements. Therefore, the explicit inversion model is not usually consistent with the forward model. Davis and others have recently developed the iterative inversion algorithm to invert a neural network [6]. The idea is to repeatedly present outputs to the forward model and search for a solution in the input space of the model while freezing the weights of the model. The algorithm is performed by computing the gradient of the cost functional with respect to the activation of the input units, and applying the iterative gradient descent algorithm to minimize the cost $\bar{E}$ [6],

$$\begin{aligned} \bar{a}(0)^{(n+1)} \longleftarrow\ & \bar{a}(0)^{(n)} - (1-\mu)(\eta \frac{\partial \bar{E}}{\partial \bar{a}(0)^{(n)}} / \parallel \frac{\partial \bar{E}}{\partial \bar{a}(0)^{(n)}} \parallel \\ & -\mu \triangle \bar{a}(0)^{(n-1)}) \ . \end{aligned} \tag{3.19}$$

In other words, instead of updating weights of networks, the iterative inversion approach updates inputs of forward models.

The iterative inversion and explicit inversion are fundamentally different. First, the iterative inversion approach finds a particular solution in the input (parameter) space, rather than an average over many possible solutions. The particular solution is one of the possible solutions, but the average solution obtained from explicit inversion may not be even be

a solution. Second, the iterative approach starts with an initial solution. By choosing a initial guess properly, one can bias the trajectory movement to find the desired solution. In this way the iterative inversion is able to incorporate additional constraints or auxiliary information.

3.5 Synthetic Data Retrieval Using Neural Networks

In the earlier section, we described a methodology to construct neural network models for remote sensing applications. The primary motivation is to make use of the inversion technique to retrieve V, LWP and IWP using three-channel radiometer observations. One of the critical issues in microwave remote sensing of atmosphere is to verify independently the quantities which have been retrieved. In spite of in-situ aircraft observations and radiosonde measurements, the independent quantifications of atmospheric parameters such as LWP and IWP are incomplete. The incompleteness of in-situ observations limits the detail verification of neural network performance. In the following sections of this chapter, we compared the independent microwave radar and radiosonde observations with the neural network based radiometer retrievals. In this section, the performance of neural network models are evaluated by using a synthetic or simulated data set. This test is critical because the true inverse solutions are known in the synthetic data set.

Based on sensitivity study results, we choose four model variables to build the parameter space: integrated water vapor (V), liquid water path (LWP), ice water path (IWP), and surface pressure (P_0). The neural network outputs are three radiometer measurements: brightness temperatures T_B at 20.6, 31.65 and 90 GHz, and surface pressure P_0. The rest of the model parameters are fixed at their mean state. Details are listed in Table 3.4. It is to be noted that surface pressure is used as an auxiliary measurement and is included in both inputs and outputs of the network to assist the training. The training data set consists of 1920 data points generated with parametric radiative transfer model by sampling input space uniformly in the range of interest. As described earlier, both a forward and an explicit inverse model are trained. Each model has four input and output units, one hidden layer with 25 neurons. After 5000 batch training, the average output errors are 0.000867 and 0.062538 for the forward and explicit inversion models, respectively.

The next step is to evaluate the performances of explicit inversion and iterative inversion neural networks. For this purpose, a time series of vapor, liquid, ice and surface pressure are specified as in Figure 3.13. Actual range of these quantities are specificed in Table

Table 3.4: Scheme 1 for synthetic data set

Retrieval variables	Range	Unit
V	(0.4, 0.97)	cm
LWP	(0.0, 800.0)	g/m^2
IWP	(0.0, 800.0)	g/m^2
P_0	(76.0, 86.0)	Kpa
Fixed Varibales	**Fixed value**	**Unit**
ρ	0.5	g/cm^3
r_c	0.05	cm
H_b	1.5	Km
H_v	2.0	Km
T_A	−2.0	$°C$
Γ	6.0	K/Km
H_{bi}	3.5	Km
D	1.0	Km
D_i	2.0	Km

3.4 and they are normalized between zero and unity for performance evaluation. The profiles in Figure 3.13 are completely independent of the training data set. These profiles are selected such that they represent a changing atmospheric condition and also ice and ice-free conditions. Using the radiative transfer model, the corresponding three-channel brightness temperatures are generated. These simulated T_Bs are used in both explicit and iterative inversion models to retrieve the physical parameters shown in Figure 3.13. The results of the explicit inversion model is given in Figure 3.14. The retrieval accuracies for V and LWP are good. However, the retrieved IWP exhibits wild fluctuation between 10 and 20 hours. Between 0 and 10 hours, the retrieved IWP is greater than the original value by 0.03 mm. This might be due to non-uniqueness of the inversion. The retrieval results using iterative inversion is displayed in Figure 3.15. The inferred values are almost identical to the original ones. There is no significant bias in V, LWP or IWP values. Surface pressure is tracked very well. These results are far-superior to explicit inversion model values. Therefore, iterative inversion is clearly superior and necessary.

3.6 Radiometer and Radar Instrumentation During WISP

WISP project was conducted near Denver, Colorado. The scientific objectives of the project are: (i) to develop and test methods using existing technology for remote detection of supercooled water and (ii) to understand the formation and maintenance of regions of super cooled water in winter storms [49]. A number of observational facilities such as radar, radiometer, radiosonde and research aircraft were deployed. Data from two different field programs were analyzed: WISP91 [50] and WISP94 [60]. In this dissertation we dealt with the data collected from NOAA two- and three-channel radiometers, NOAA K-band radar and radiosondes. The three-channel radiometer is located at Erie, Colorado and measures the brightness temperatures at 20, 30 and 90 GHz. The two-channel radiometer is located at Plateville, Colorado and it records T_Bs at 20 and 30 GHz. The two and three-channel radiometers are separated by 30 km. Under cloudy conditions, the spatial inhomogenuities in atmospheric quantities prevented from intercomparison of these two observations.

The NOAA K-band radar was co-located with the three-channel radiometer at Erie, Colorado. The radar is one of the most sensitive ones and it can typically detect -30 dBz echo at 10 km range. Operational characteristics of the radar are shown in Table 3.5. The National Center for Atmospheric Research (NCAR) launched Cross-chain Loran

Table 3.5: NOAA K-Band Radar Characteristics

Antenna	
System Gain	43.75
Polarization	H/V, Circular
Scan Rate (deg/s)	0 - 30
Beam with (deg)	0.5
Transmitter	
Wavelength (cm)	0.87
Frequency (GHz)	34.76
Peak Power (kW)	98
Pulse Width (μs)	0.25
Date Acguisition	
No. of Range Gates	328
Gare Spacing (m)	37.5 - 75

Atmospheric Sounding System (CLASS). These sondes provided temperature, dewpoint temperature, pressure and wind profiles. We used the sonde measurements which are the closest in time and space with regard to the respective radiometer observations.

3.7 Retrieval of Meteorological Parameters by Neural Networks

Ground-based radiometer measurements include the brightness temperatures at two or three channels, surface pressure, temperature and humidity parameters. However, most of the radiometers operate in a dual-channel mode. Therefore, first we compare neural-net derived values against NOAA's dual-channel statistical algorithm based results. Then we explore the possibility of ice information retrieval by including 90 GHz channel.

3.7.1 Dual-channel radiometer models

Ground-based dual-channel radiometers retrieve integrated water vapor and liquid water path using brightness temperature measurements at 20.6 and 31.65 GHz channels. So far, only statistical retrieval algorithms are widely used in routine radiometer operations. It's

very desirable to see if our physical models based neural networks can produce retrievals comparable to statistical ones. However, it should be borne in mind that both statistical model and our neural network model have inherent biases. As we mentioned before, uncertainties in calculation of water vapor absorption will introduce some biases for each kind of model. For NOAA's radiometric model, the average accuracy of water vapor retrieval was estimated to be 0.175 cm with about 0.1 cm bias [20] [5]. For radiosonde measurements, water vapor is accurate up to about 0.11 cm [19]. In this section, only iterative inversion approach was used. There are two ways of model comparison. We can either feed NOAA's retrieval data into our forward model and compare simulated brightness temperatures with radiometer measurements, or we can invert radiometer measurements using iterative inversion and compare the retrievals by two different models. To contrast different retrieval schemes, several cases will be processed repeatedly by different neural networks. Case A measurements were collected by NOAA three channel radiometer on a clear day of 22 March 1994 at Erie, Colorado. This data set was used for the instrument calibration. Case B measurements were taken on 15 March 1991 by a dual-channel radiometer at Platteville, Colorado, which is about 30 miles north-east of Erie. Case C is again three channel radiometer measurement taken on on the same day as case B at Erie. On this day, there were a persistent snowband oriented north-south in eastern Colorado, and low clouds that contained supercooled liquid water. The base and top of the liquid layer were estimated at 0.80 and 1.13km AGL [58].

A forward model was trained by synthetic data created with our parametric radiative transfer model. It has two input units for water vapor and liquid water, three output units for brightness temperatures at 20.6, 31.65 GHz and 90 GHz channels, and one hidden layer with 10 neurons. The training data are generated under the scheme 2 in Table 3.6. Constants chosen for fixed parameters are roughly based on long time winter seasonal average at Denver. After training, this forward model is used to process radiometer data of Case A. Figure 3.16 through 3.18 compare the brightness temperature simulations with measurements at the two radiometer channels. NOAA's retrieval was fed into our forward neural network model. It is to be noted that our physical model exhibits very similar trends to those predicted by NOAA's non-physical (statistical) model. The plots indicate some biases between the two models. The mean and standard deviation of the biases are 1.503° K and 0.223° K at 20.6 GHz, 0.984° K and 0.135° K at 31.65 GHz, and 0.276° K and 0.389° K. Since NOAA radiometers models are well calibrated at these three channels, a

simple way to calibrate our model would be to ingest the biases between the two models into our synthetic training data and redo the forward model training. A complete model calibration technique is not of interests in this dissertation.

A calibrated forward model provides a basis for fair comparison of inverse models. Our first inverse neural network model was trained using calibrated synthetic brightness temperature at 20.6 and 31.65 GHz to retrieve water vapor and cloud liquid. Case A has been used for model calibration. To have a stronger comparison, we used another data set, Case B measurements, for iterative inversion of water vapor and liquid water. The inverse results are plotted against NOAA retrieval in Figure 3.19 and 3.20. The dots indicate independent water vapor measurements by radiosondes. The reader is reminded that the radiosonde accuracy of water vapor is about 0.11cm. Plots show excellent agreement between both of the retrieval techniques. However, this agreement means nothing more than the consistency of these two techniques. They are actually both biased in the same way by ignoring the existence of ice cloud.

3.7.2 Three channel radiometer models

Ground-based three channel radiometers have been operating for several years. But to author's knowledge, retrieval algorithm has no better performance on vapor and liquid retrieval by including measurements at 90 GHz channel. There are several reasons. First, if one wants to retrieve water vapor and liquid water only, one more channel at 90 GHz may not be helpful unless it is better calibrated. Second, 90 GHz is very sensitive to ice cloud. Even well calibrated with water vapor and liquid water, the channel could be very noisy when ice is present. Here, we use three-channel radiometer to explore the possibility of ice information retrieval. However the ice information contained in three channels is incomplete. Our sensitivity study shows that Brightness temperature is also sensitive to both bulk density and mean size of ice clouds. With only three channels, the retrieval algorithm is definitely nonunique. Therefore, we have to use iterative inversion and retrieve more than three significant model parameters.

Our three channel radiometer models have 4 input and 3 output units, one hidden layer with 30 neurons. The neural network input vector includes integrated water vapor, liquid water path, ice water path, and ice particle mean size; and the output units are brightness temperature at three channels. The bulk density is fixed at $\rho = 0.5\ g/cm^3$. For other information please see Table 3.6 under Scheme 3. Before training, the synthetic data was

Table 3.6: Scheme 2 and 3

	Scheme 2	Scheme 3	
Retrieval variables	Range	Range	Unit
V	(0.4, 0.97)	(0.3, 0.9)	cm
LWP	(0.0, 800.0)	(0.0, 280.0)	g/m^2
IWP	(0.0, 800.0)	(0.0, 800.0)	g/m^2
P_0	(76.0, 86.0)	84.0	Kpa
ρ	0.5	0.65	g/cm^3
r_c	0.05	(0.01, 0.15)	cm
H_b	1.5	1.0	Km
H_v	2.0	2.0	Km
T_A	−2.0	−2.0	^oC
Γ	6.0	6.0	K/Km
H_{bi}	3.5	3.5	Km
D	1.0	1.5	Km
D_i	2.0	2.0	Km

calibrated at 20.6 and 31.65 GHz channel as in dual-channel radiometer models. 90 GHz was not calibrated.

Case C is processed by this three channel model and the two channel in the last section. The results are illustrated in Figure 3.21 through 3.23. Figure 3.21 and 3.22 compare the two and three channel radiometric retrieval of water vapor and liquid water with NOAA's model results. The dots are again independent radiosonde measurements. Assuming radiosonde data is accurate, our two and three channel neural network models produced results that are about the same as, or better than, those of NOAA's dual-channel model. Figure 3.23 depicts the retrievals of ice water path and mean size of ice particles. It is worth mentioning that the forward model can match accurately the measurements when provided with the retrieval of our three channel model. In other words, our retrieval is indeed a model solution. Therefore it is feasible to retrieve ice information using ground-based three channel radiometers. A well-trained Neural network is capable of retrieving water vapor, cloud liquid, and cloud ice. The performance of these techniques can be verified by comparing with radar and aircraft estimated values.

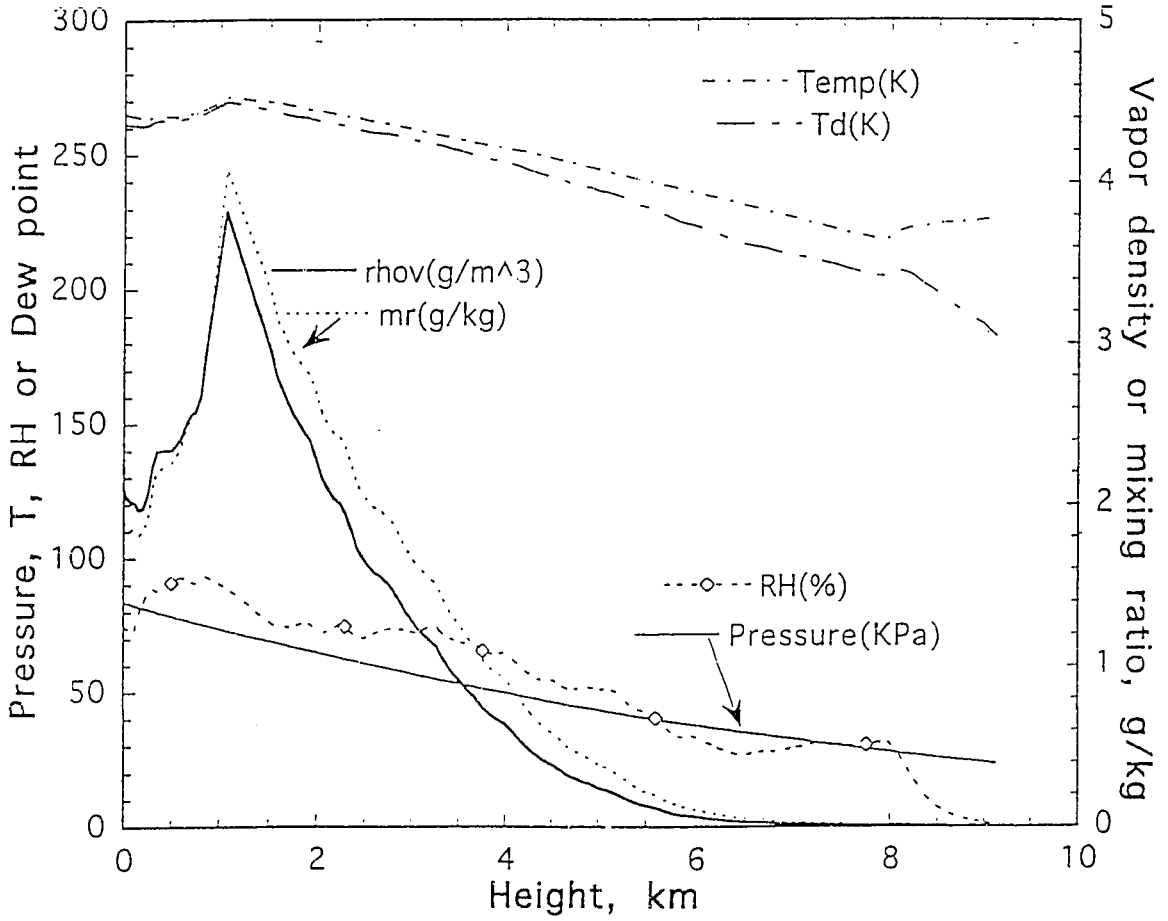

Figure 3.1: Pressure, temperature, dew point, relative humidity, vapor density, and mixing ratio profiles measured by radiosonde at 15:00 GMT, 2 March 1991.

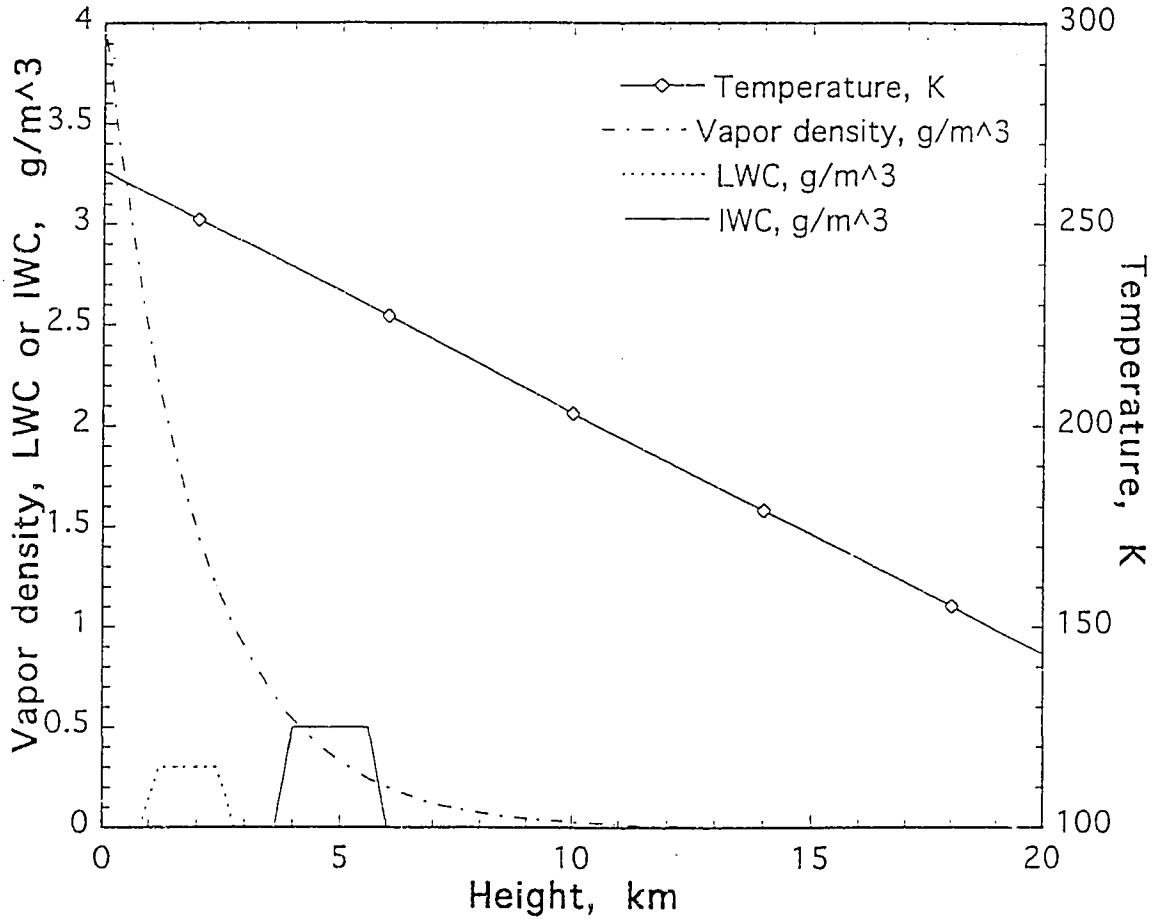

Figure 3.2: An example of a parameterized atmosphere structure which is used as an input for the parametric radiative transfer model.

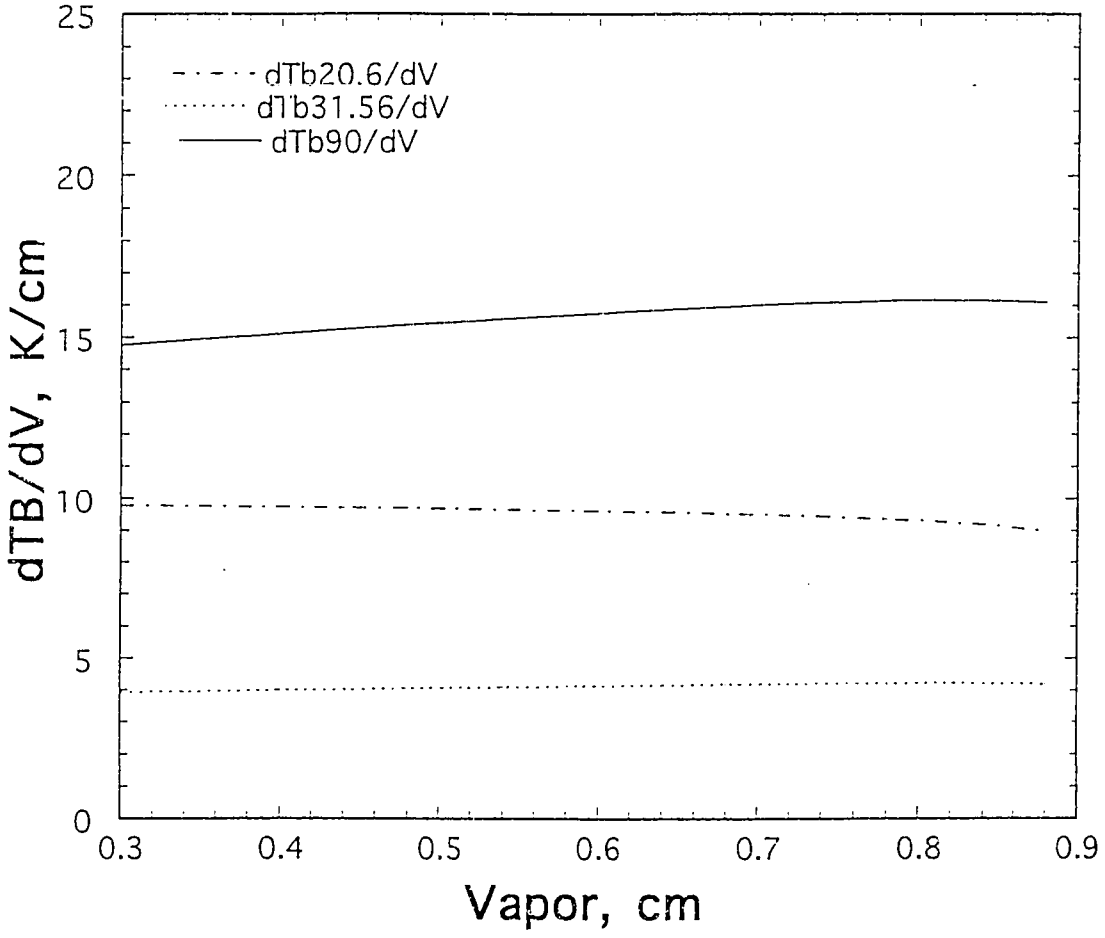

Figure 3.3: Ground-based three-channel radiometer brightness temperature sensitivities to integrated water vapor $(\partial T_B/\partial V)$ (V), as function of V.

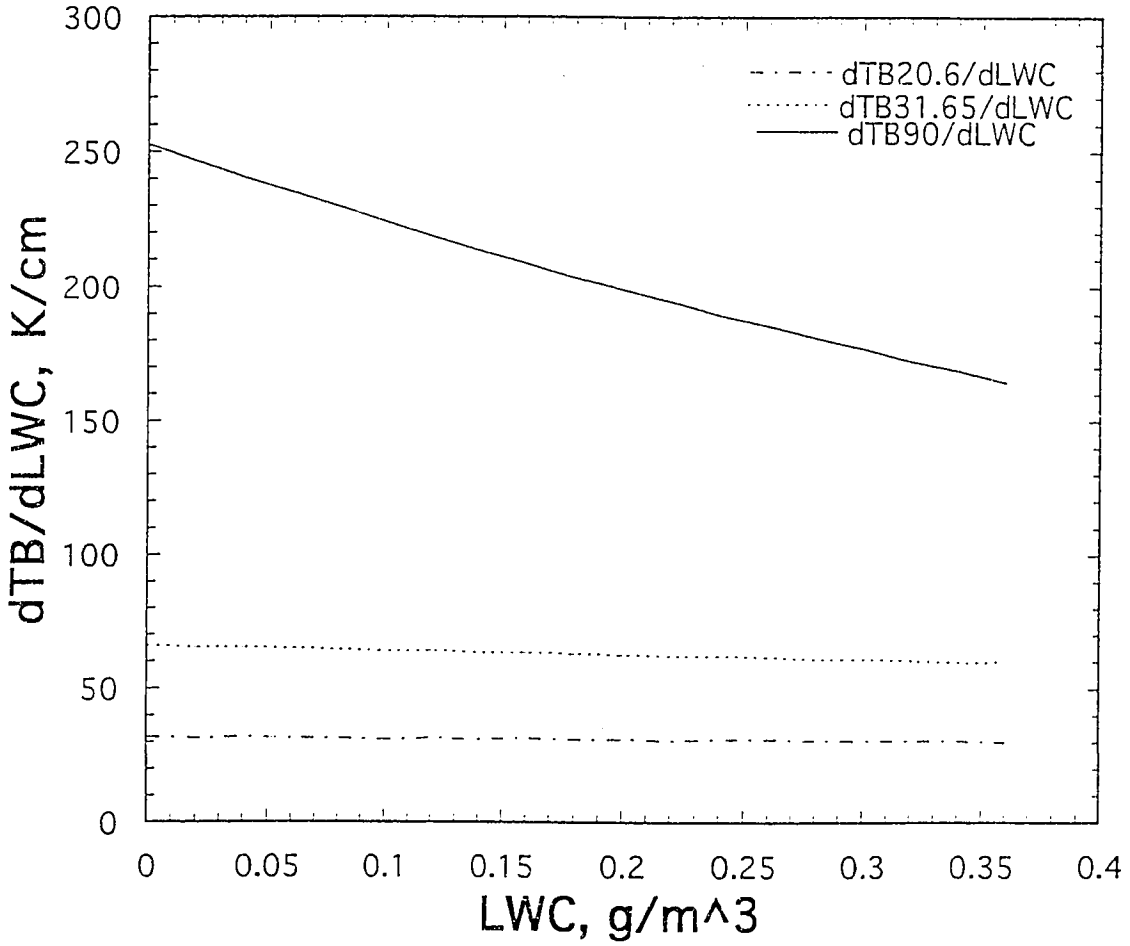

Figure 3.4: Ground-based three-channel radiometer brightness temperature sensitivities to liquid water content (LWC) ($\partial T_B/\partial LWC$), as function of LWC.

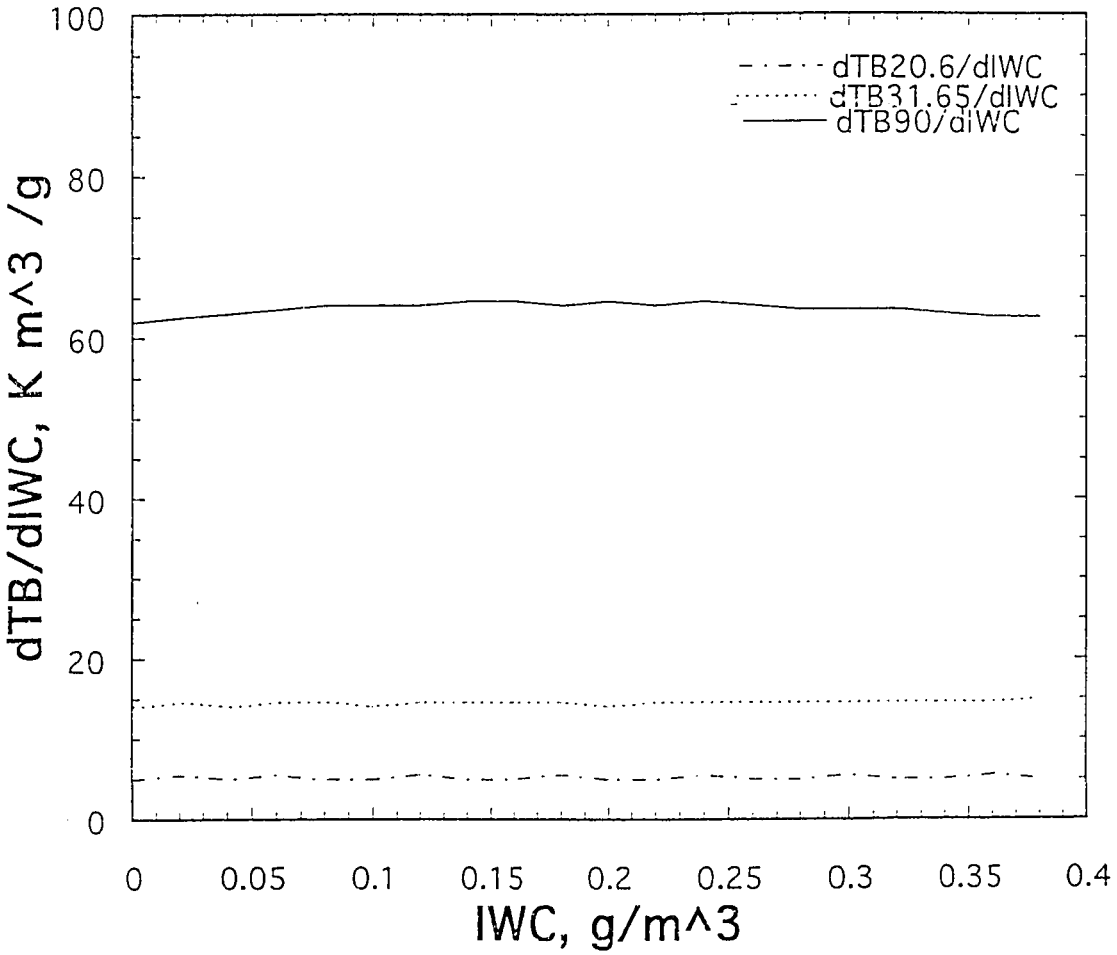

Figure 3.5: Ground-based three-channel radiometer brightness temperature sensitivities to ice water content (IWC) ($\partial T_B/\partial IWC$), as function of IWC.

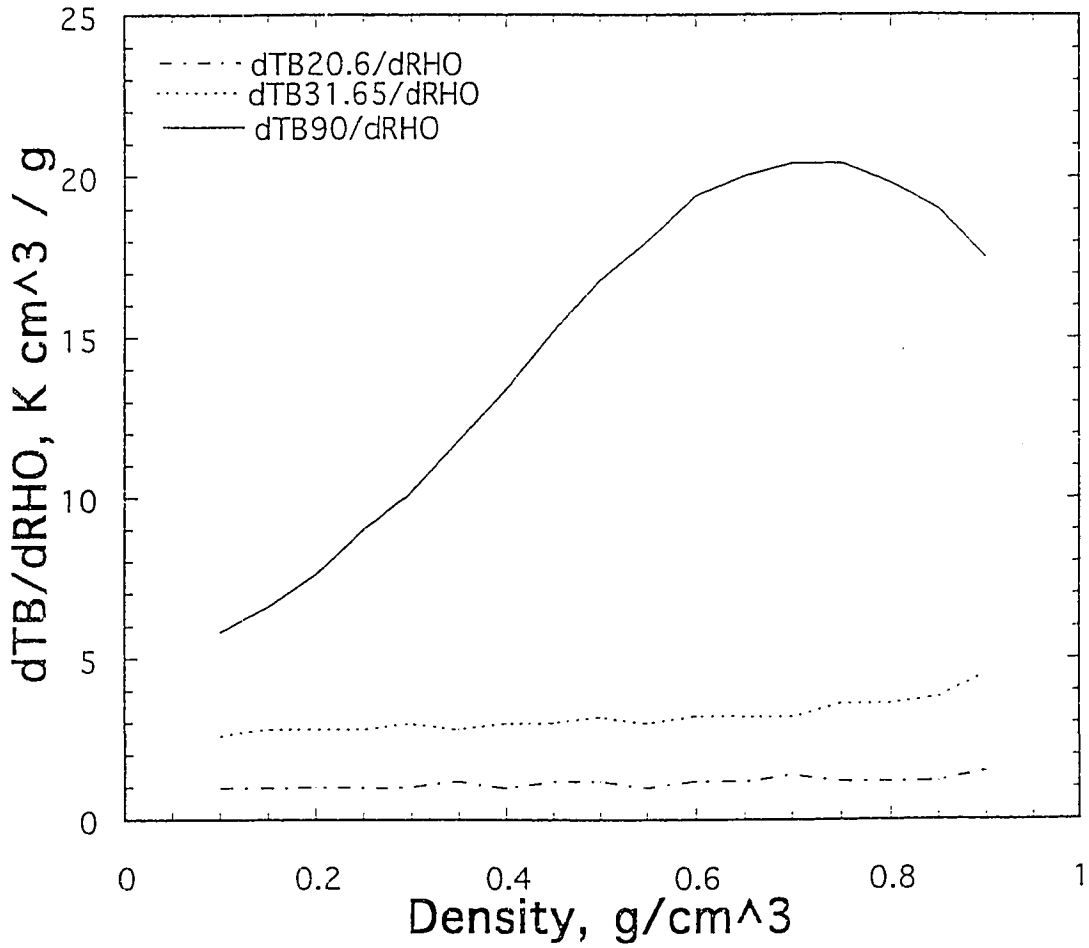

Figure 3.6: Ground-based three-channel radiometer brightness temperature sensitivities to ice bulk density ρ ($\partial T_B/\partial\rho$) as function of ρ.

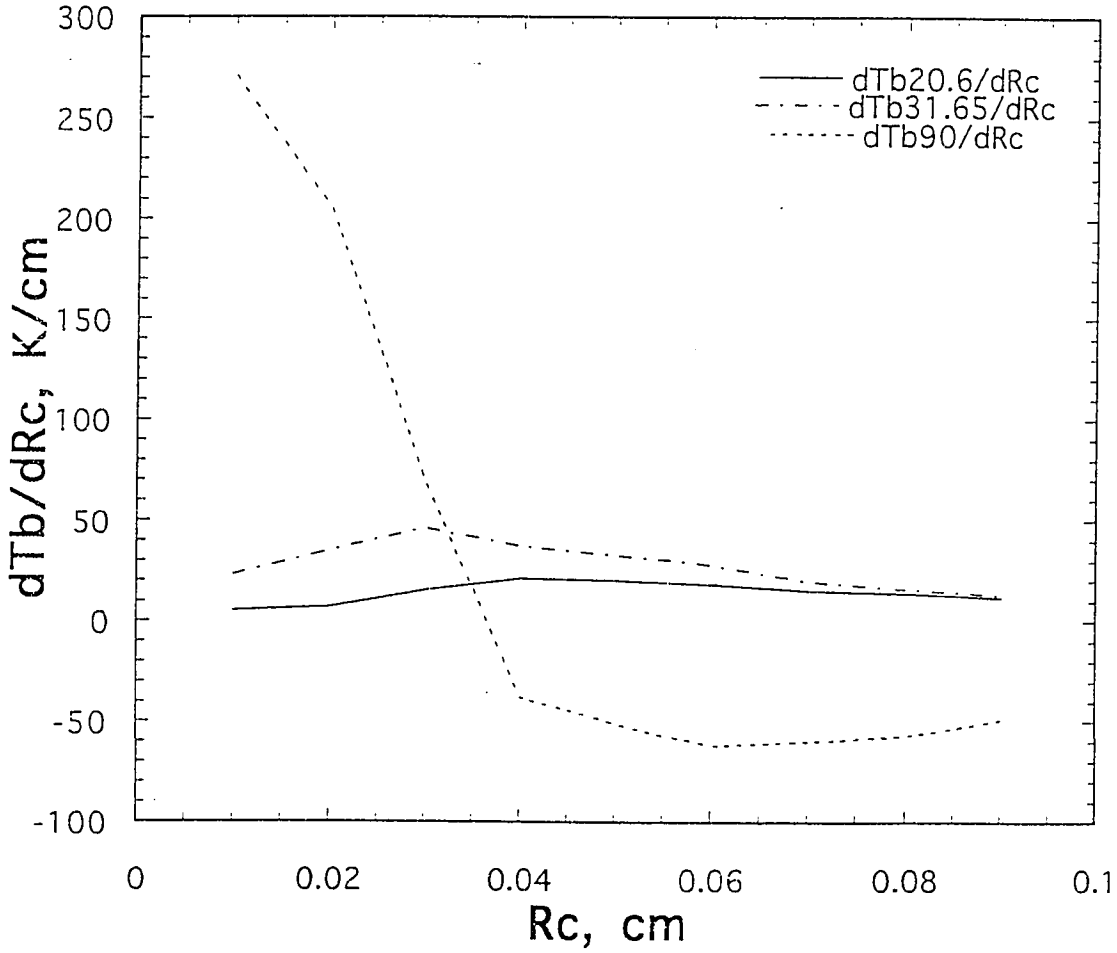

Figure 3.7: Ground-based three-channel radiometer brightness temperature sensitivities to mode radius of ice particles $(\partial T_B/\partial r_c)$ as function of r_c.

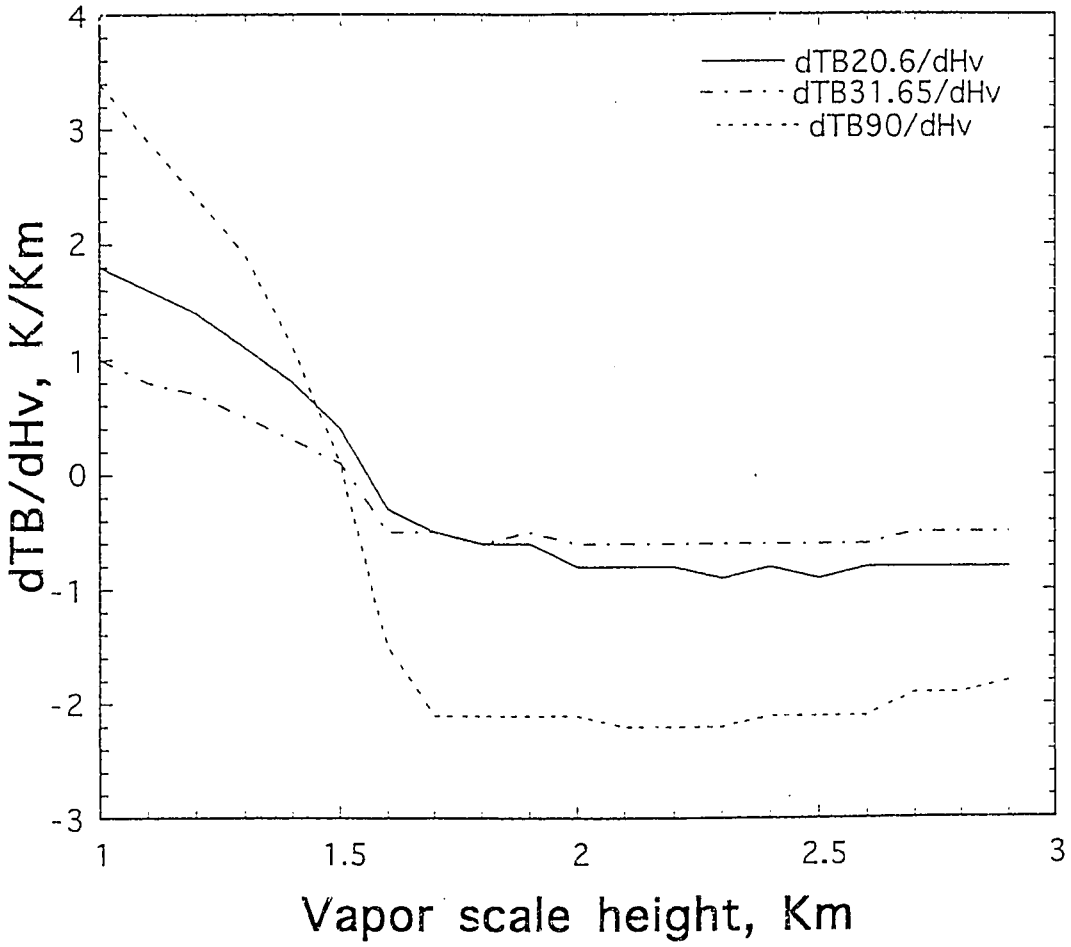

Figure 3.8: Ground-based three-channel radiometer brightness temperature sensitivities to vapor scale height H_v ($\partial T_B/\partial H_v$) as function of H_v.

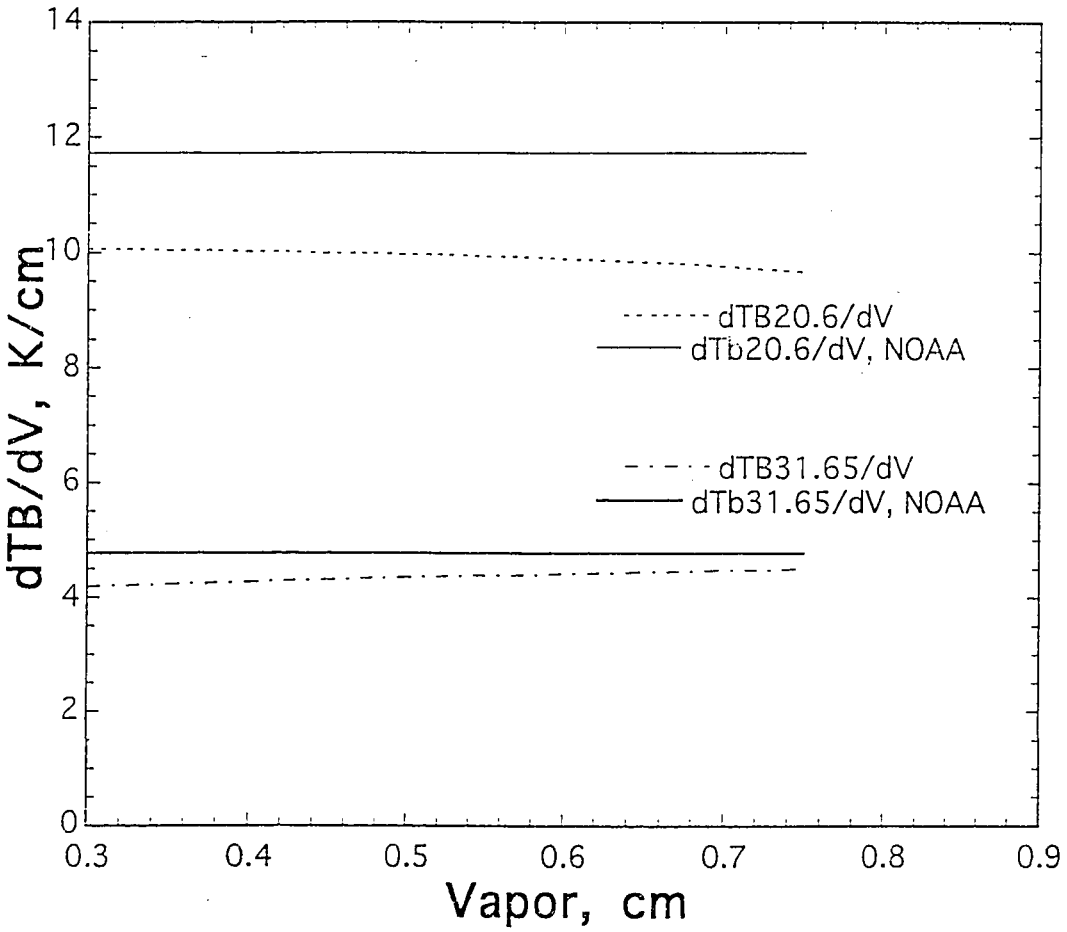

Figure 3.9: Model sensitivity to water vapor path ($\partial T_B/\partial V$). Sensitivities between NOAA's linear statistical inverse model and the parametric radiative transfer model are compared for the ground-based dual-channel radiometer.

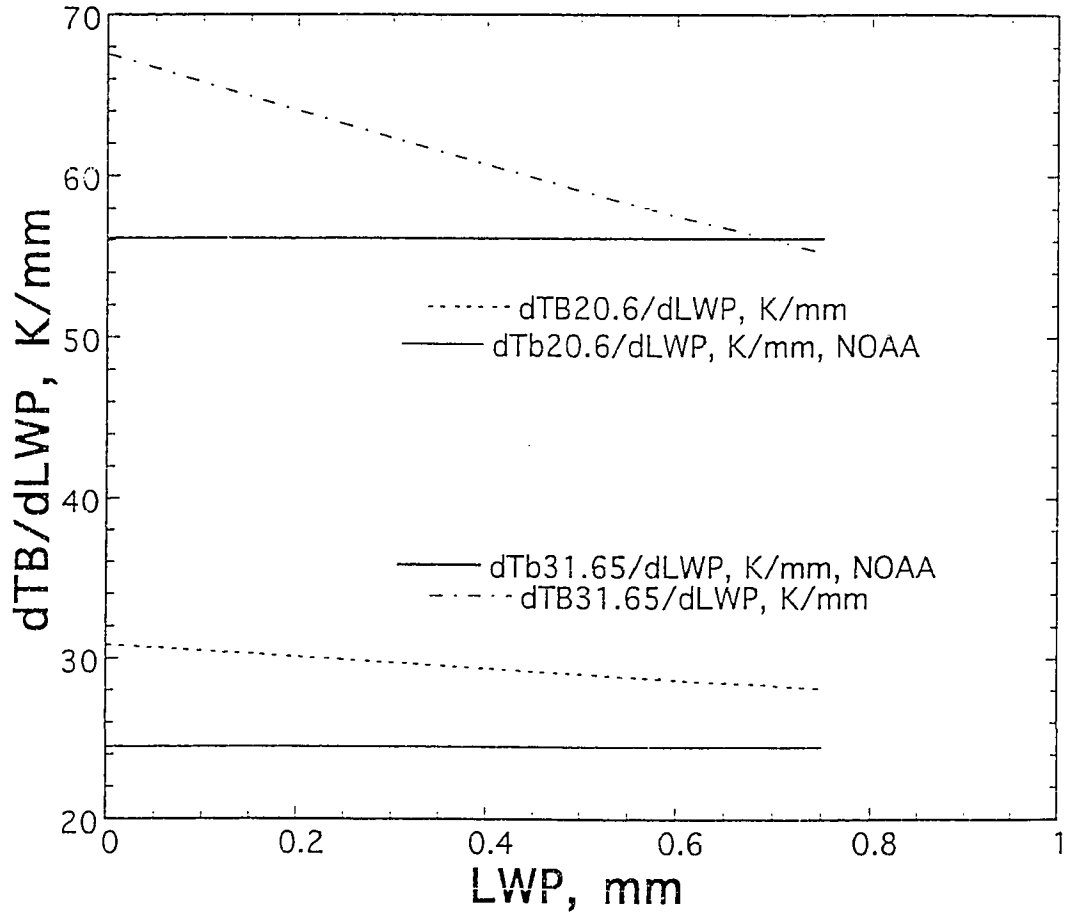

Figure 3.10: Model sensitivity to liquid water path ($\partial T_B / \partial LWP$). Sensitivities between NOAA's linear statistical inverse model and the parametric radiative transfer model are compared for the ground-based dual-channel radiometer.

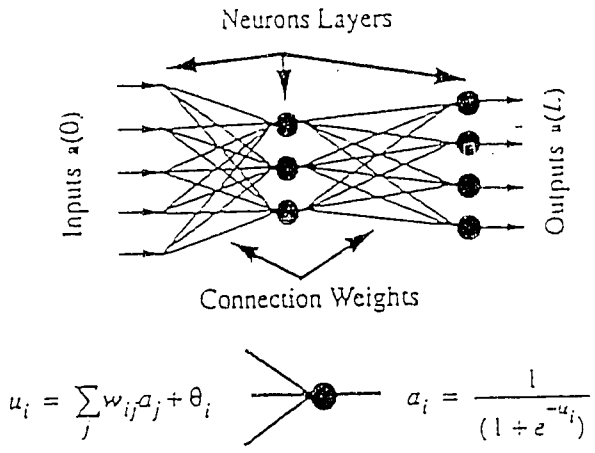

Figure 3.11: The basic structure of a multilayer perceptron. The input layer feeds the input vector, multiplied by the associated connection weights, to the neurons of the next layer, where the multiplied input values are summed, added to an offset, and passed through a sigmoid function, the output of which serves as the input to the next layer of neurons.

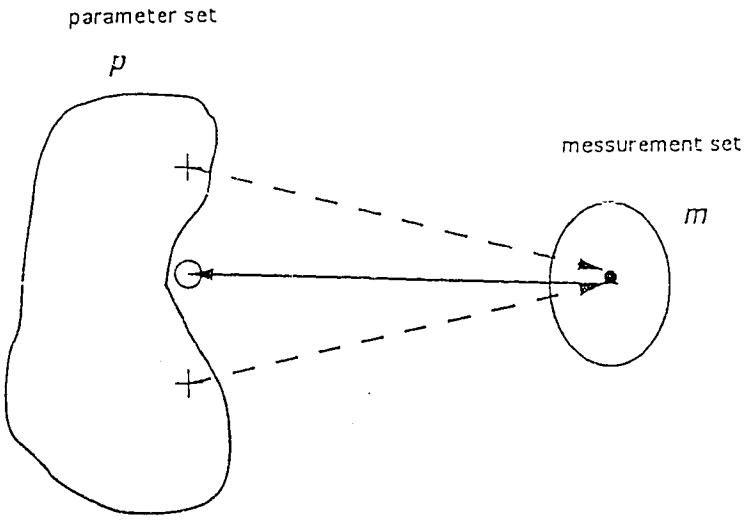

Figure 3.12: The non-convex problem. Forward model accurately maps each parameter to the resulting measurement set, while explicit inverses may face one-to-many mapping. The solid arrow line represents the direction in which the mapping is learned by explicit inversion. The two points lying inside the inverse image in parameter space are averaged by the learning procedure, yielding the vector represented by the small circle. This point is not a solution, because the inverse image is not convex.

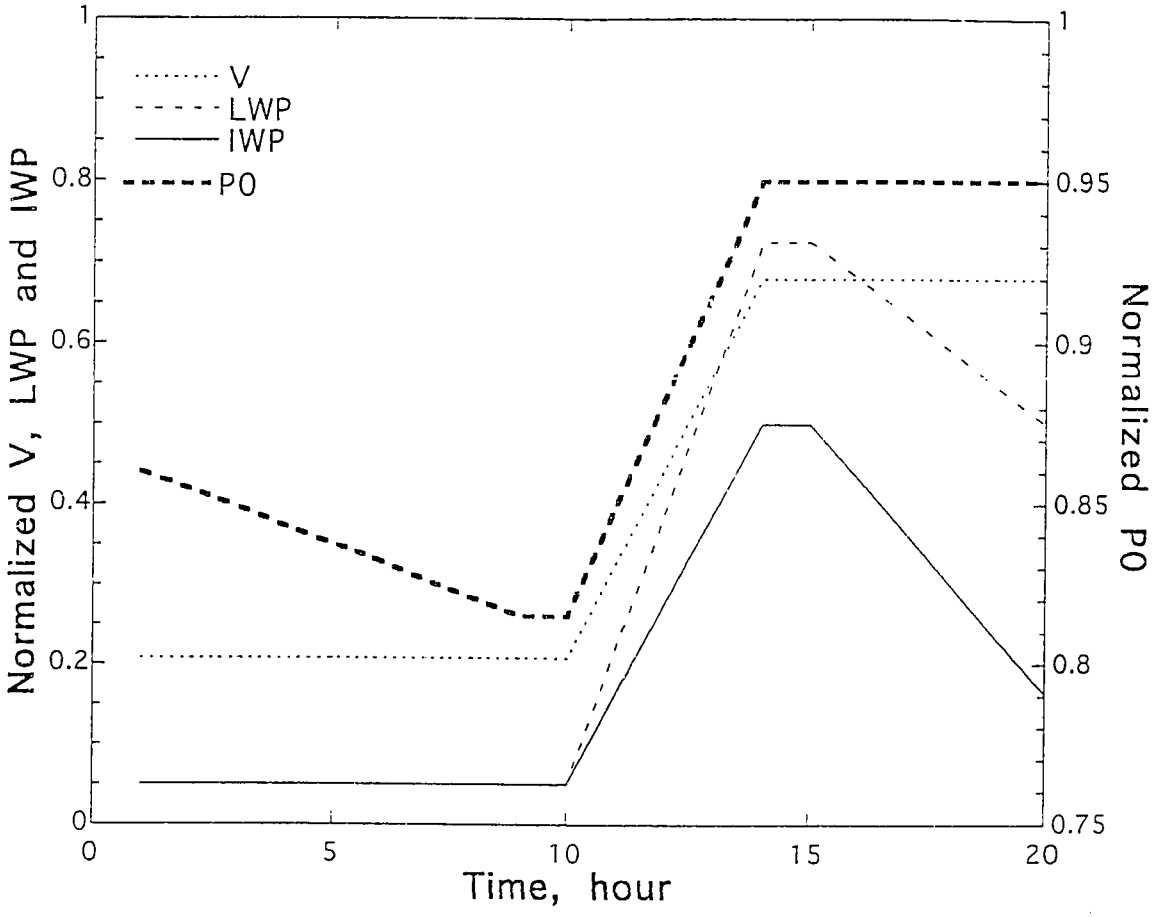

Figure 3.13: Model atmospheric time series of normalized pressure, vapor, liquid, and ice components. This data set was used to simulate ground-based radiometer brightness temperatures using the parametric radiative transfer model.

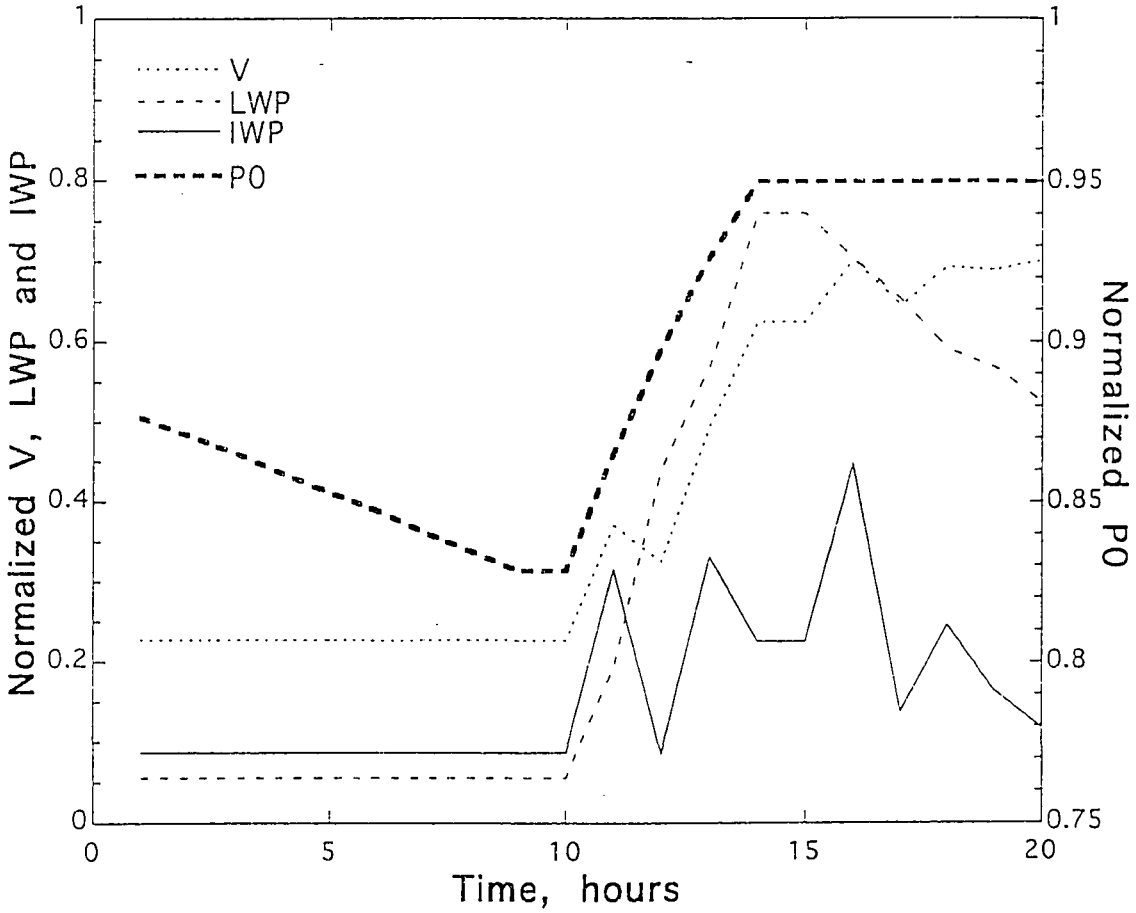

Figure 3.14: Retrieved time series of normalized pressure, vapor, liquid, and ice components from simulated ground-based radiometer brightness temperatures using explicit inversion neural network modeling.

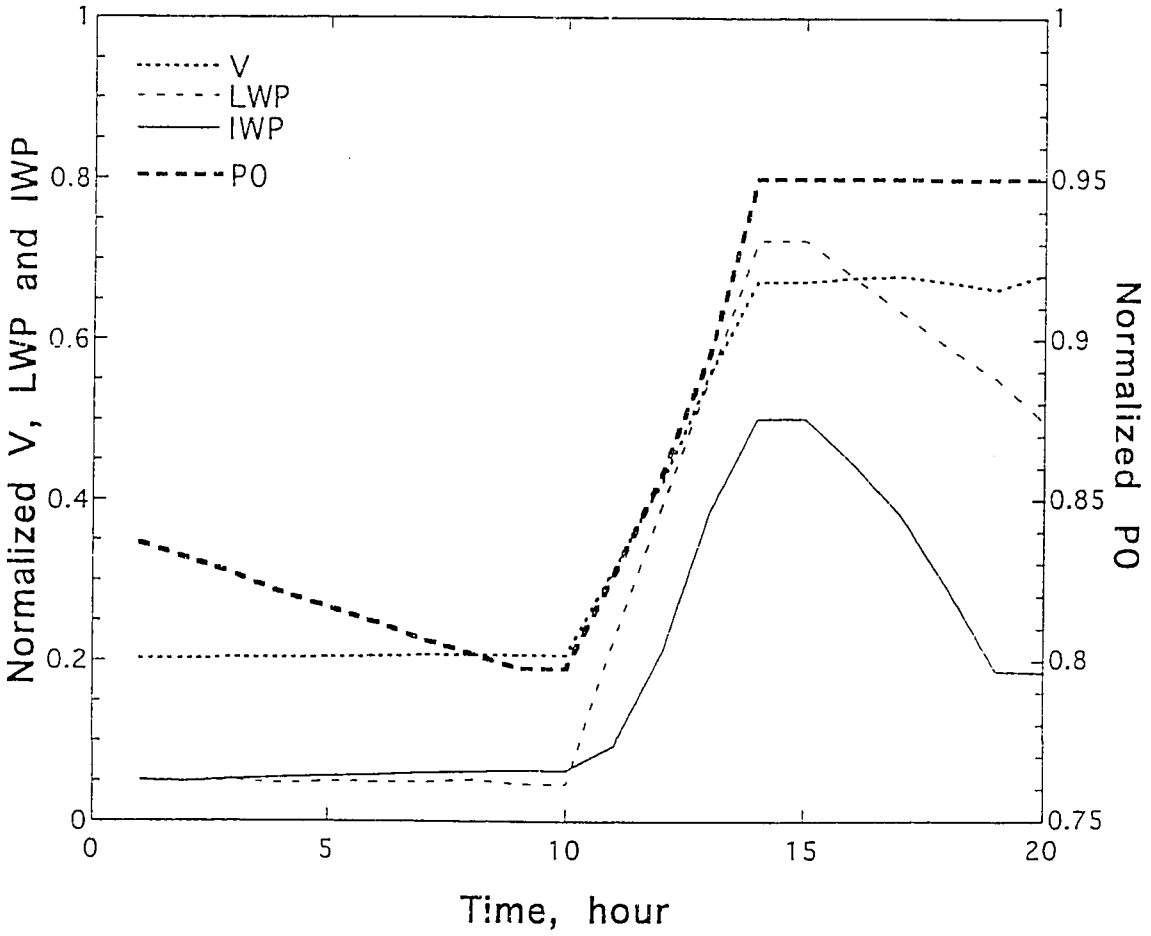

Figure 3.15: Retrieved time series of normalized pressure, vapor, liquid, and ice components from simulated ground-based radiometer brightness temperatures using iterative inversion neural network modeling.

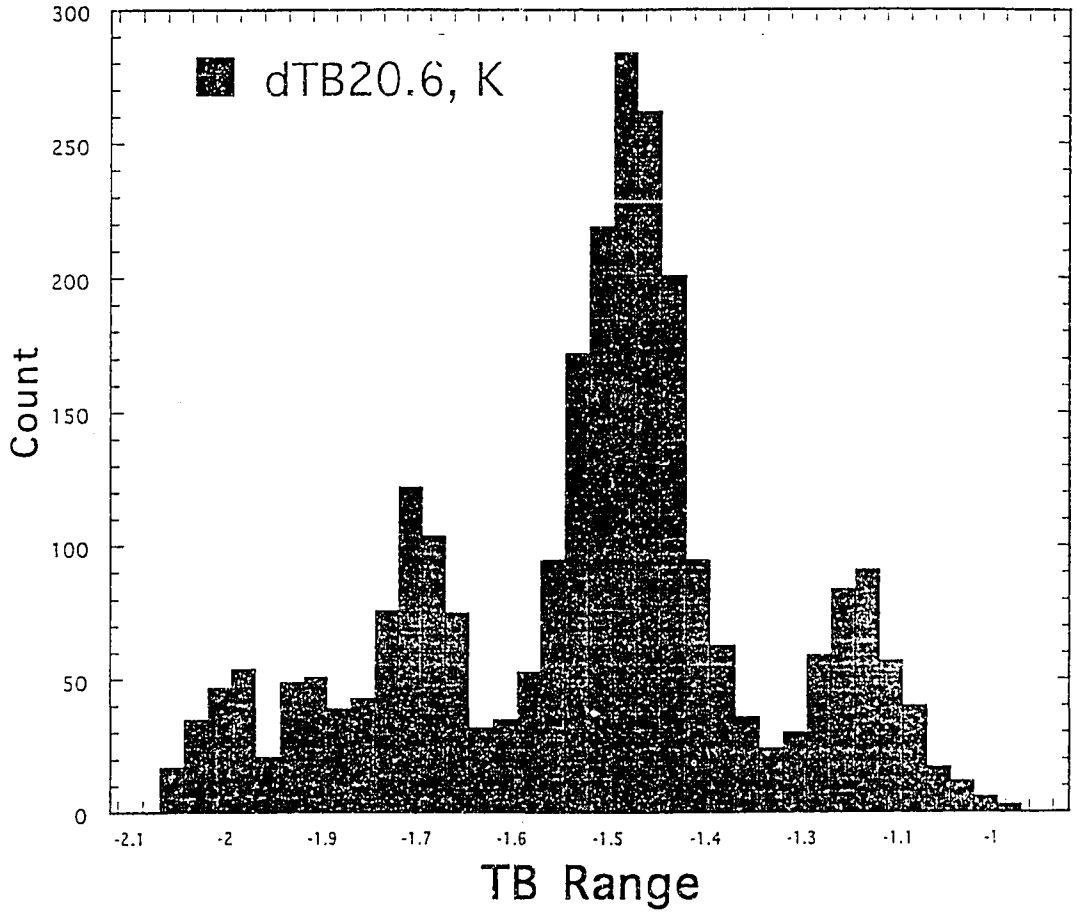

Figure 3.16: Brightness temperature bias at 20.6 GHz on Case A between uncalibrated physical model and NOAA statistical model.

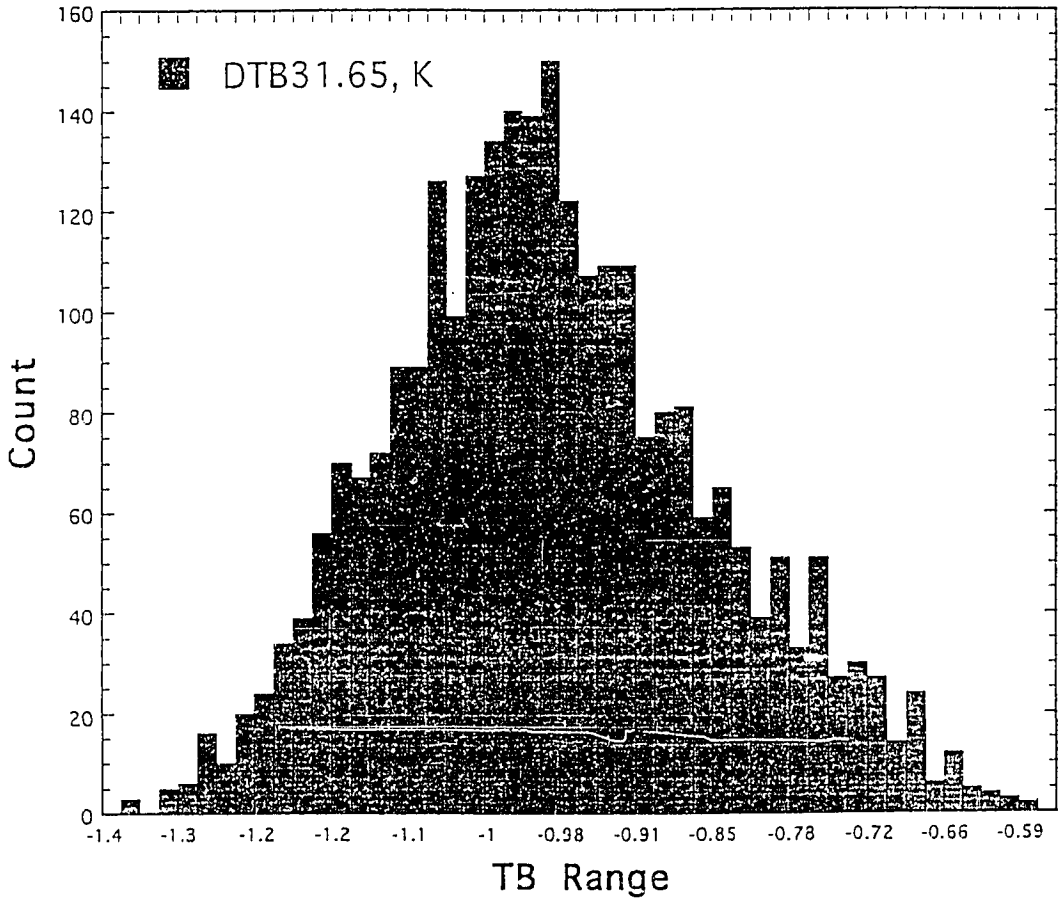

Figure 3.17: Brightness temperature bias at 31.65 GHz on Case A between uncalibrated physical model and NOAA statistical model.

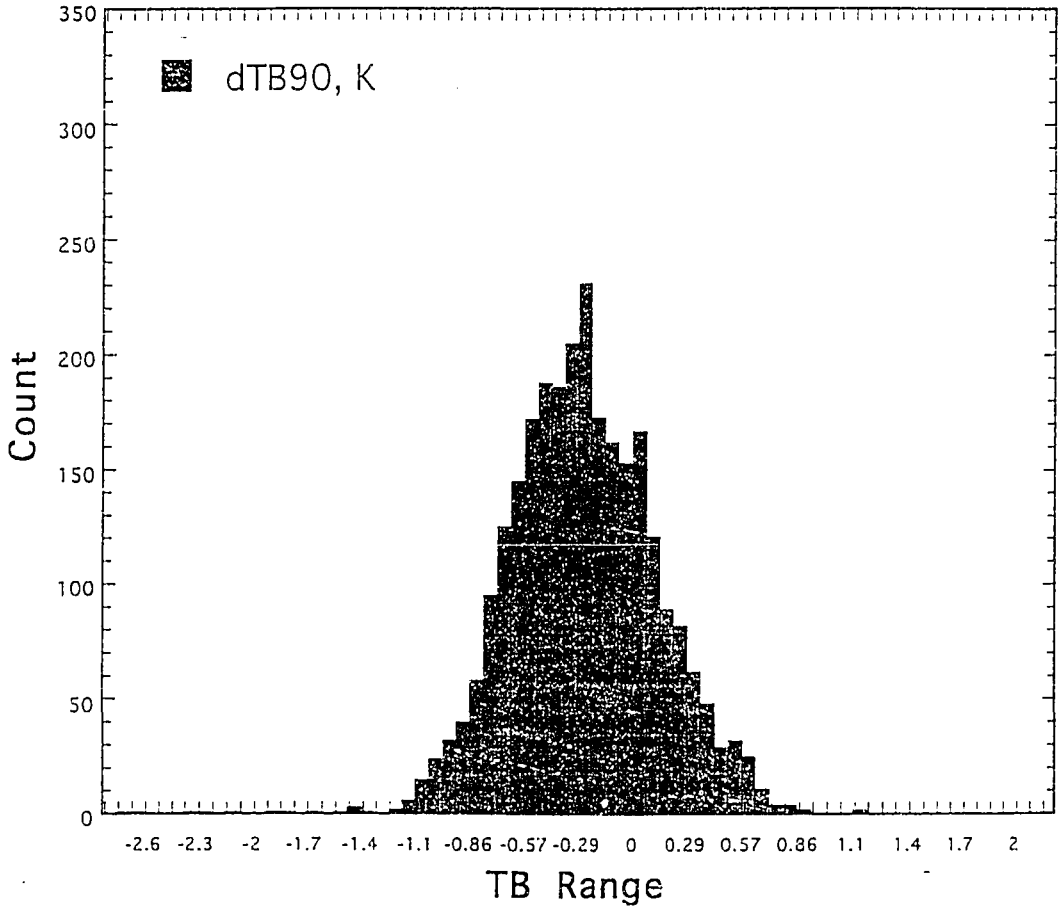

Figure 3.18: Brightness temperature bias at 90 GHz on Case A between uncalibrated physical model and NOAA statistical model.

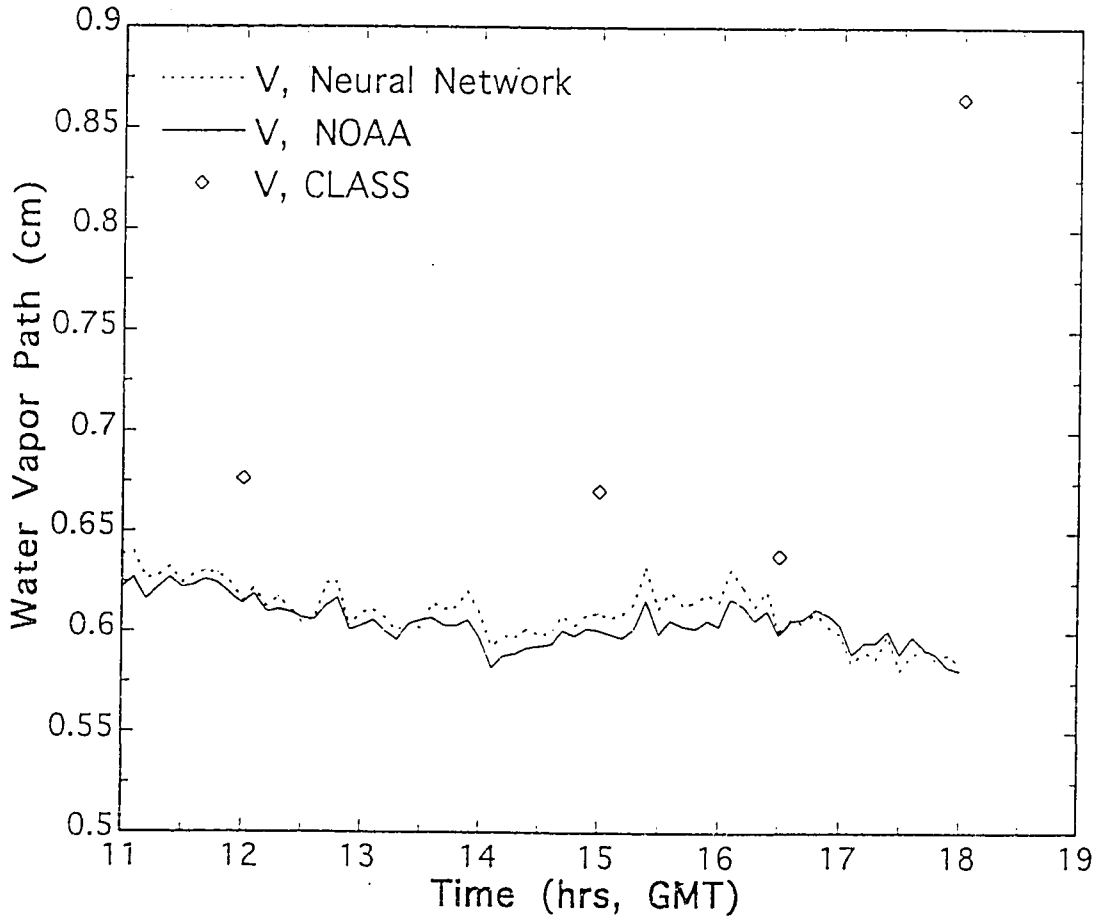

Figure 3.19: Comparison of water vapor retrieval from dual-channel radiometer between physical inverse model and NOAA statistical model. Discrete data points are in situ measurements of radiosonde. Radiometer data were taken on 15 March 1991 at Platteville, Colorado.

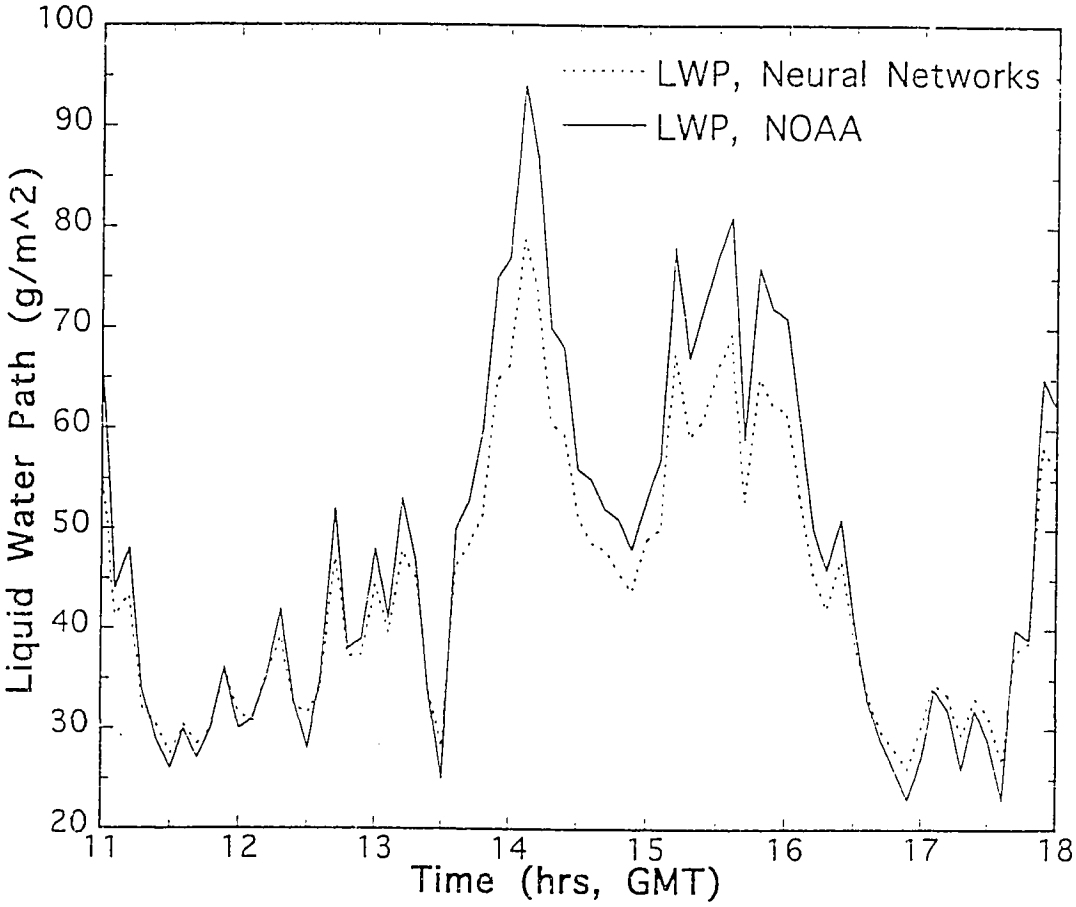

Figure 3.20: Comparison of liquid water retrieval from dual-channel radiometer between physical inverse model and NOAA statistical model. Radiometer data were taken on 15 March 1991 at Platteville, Colorado.

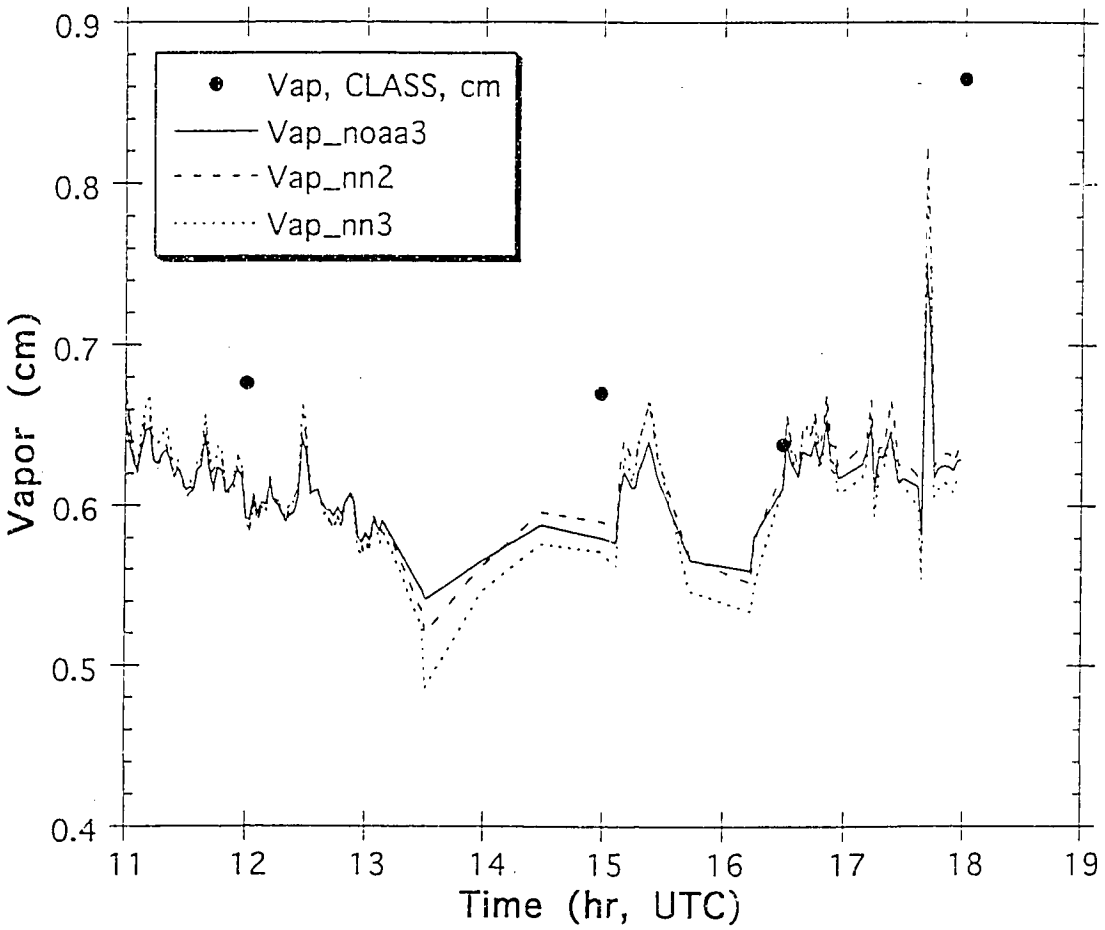

Figure 3.21: Comparison of water vapor retrieval from three-channel radiometer between physical inverse model and NOAA statistical model. Discrete data points are in situ measurements of radiosonde. Radiometer data were taken on 15 March 1991 at Erie, Colorado.

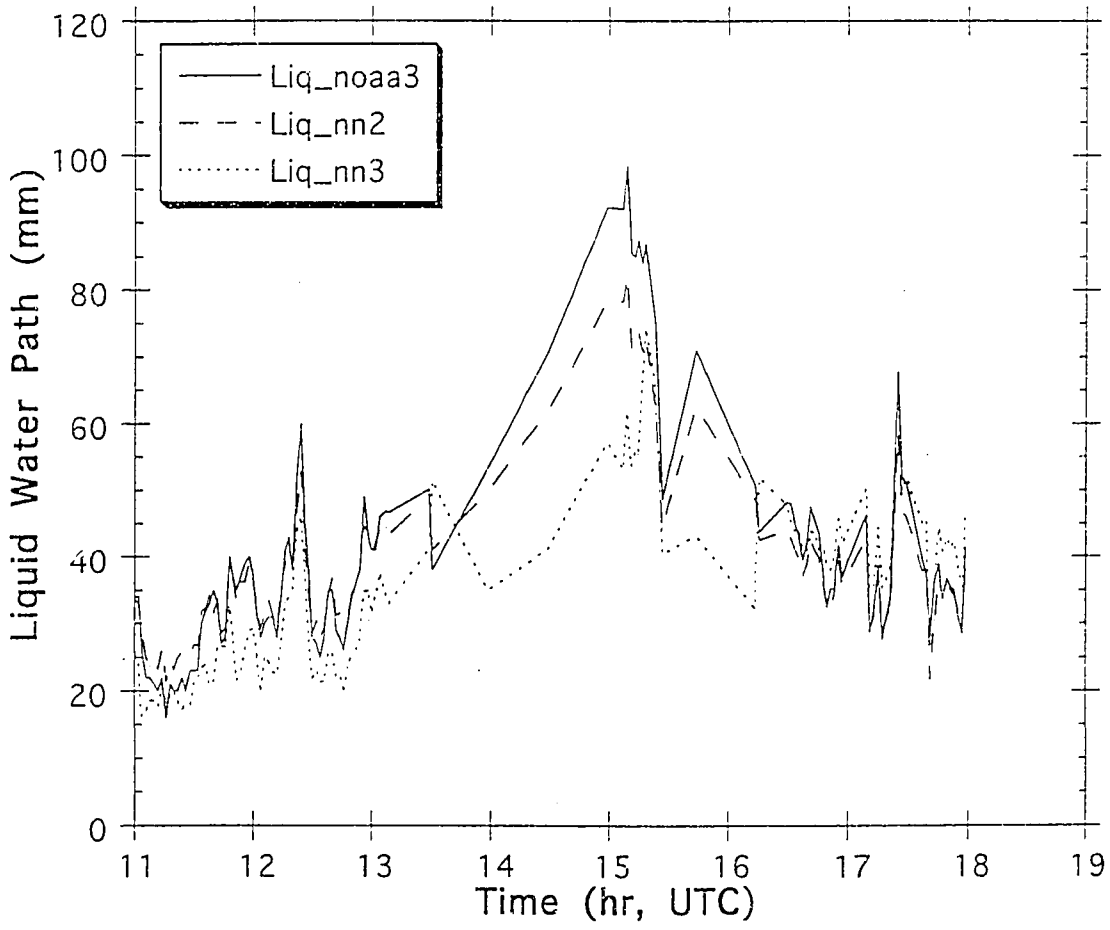

Figure 3.22: Comparison of liquid water retrieval from three-channel radiometer between physical inverse model and NOAA statistical model. Radiometer data were taken on 15 March 1991 at Erie, Colorado.

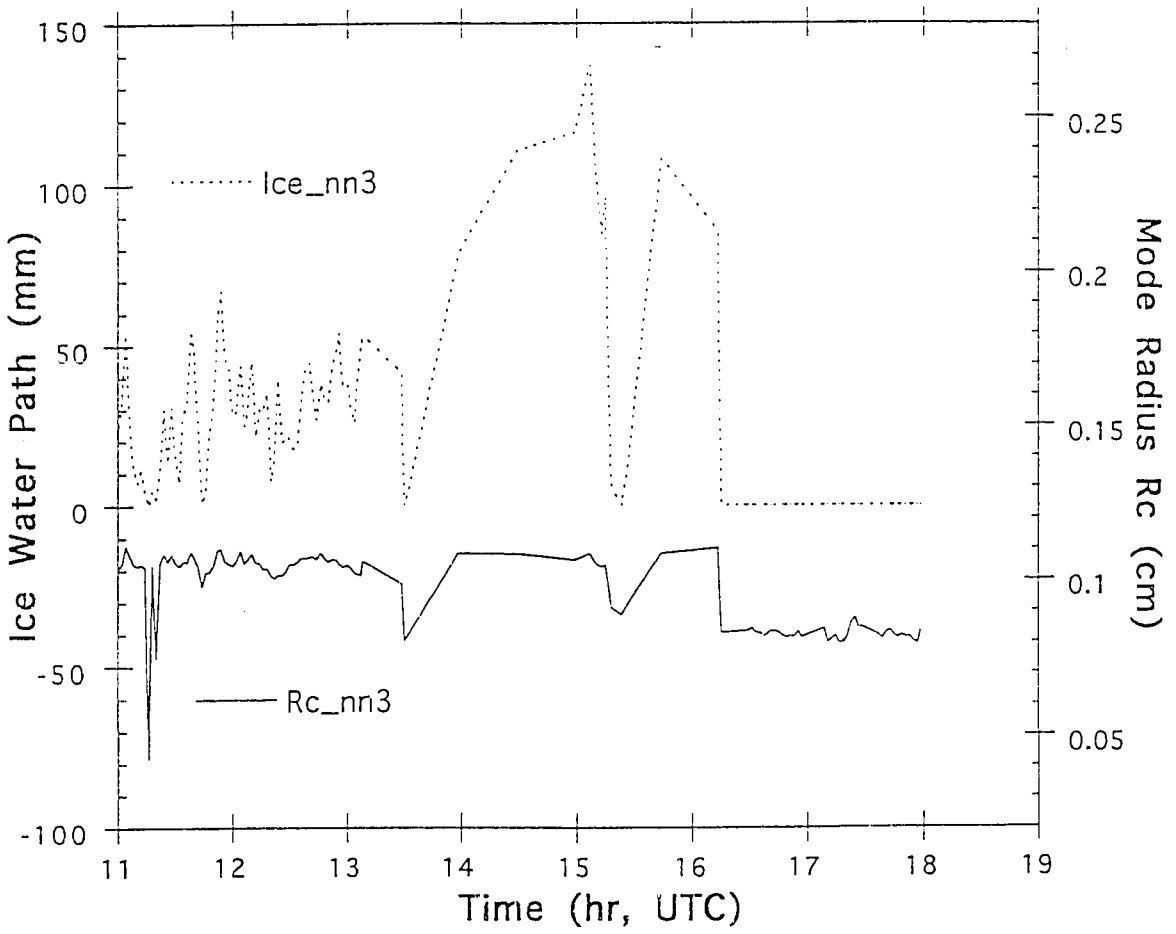

Figure 3.23: Ice water path and mode radius retrievals from three-channel radiometer Radiometer data were taken on 15 March 1991 at Erie, Colorado.

Chapter 4

COMBINED RADAR/RADIOMETER METHOD

Since 1990, a number of combined radar and radiometer methods have been proposed and investigated for the cloud and precipitation profiling from airborne or spaceborne platforms [39] [40] [26] [37] [59]. Although most of those algorithms are still focused on simulations of radar and radiometer observations, and no complete inverse algorithm has been developed, some preliminary results already indicated that a combined radar/radiometer method should be able to handle multilayer precipitation structures since it reduces the ambiguity of radar atmosphere profiling. In principle, a combined radar/radiometer method can integrate different precipitation components, such as, rain, melting, and snow, in a potentially consistent way. But fully consistent modeling of radar/radiometer has not been achieved [27] [40]. Of course, any combined method would be premature without a through understanding of the relationship between radar and radiometer observations. On the other hand, a preliminary combined radar/radiometer inverse model can also help us to understand this relationship. For the purpose of this dissertation, we will briefly discuss some perspectives of radar inverse techniques, then propose and illustrate a combined radar/radiometer method to vertically profile ice microphysics such as mean bulk density, number concentration and ice particle median diameter.

4.1 Combined Radar/radiometer Method

The ice particle size spectrum is usually described by the Gamma size distribution [67] as

$$N(D) = N_0 D^m \exp[-(3.762 + m)D/D_0] \tag{4.1}$$

where D is the equivolume particle diameter of the ice crystal and D_0 the median diameter. For C-band and K-band radar observations in winter seasons, most liquid and ice clouds, even snow, can be modeled by Rayleigh approximation [8]. A general relationship between reflectivity Z_{hh} and ice water content (IWC) is given as [68],

$$
\begin{aligned}
Z_{hh} &= 0.242 N_0^{-\frac{3}{4+m}} \Gamma(7+m) \rho^{(0.736+0.934m)/(4+m)} \\
&\quad [\frac{6000}{\pi \Gamma(4+m)}]^{\frac{7+m}{4+m}} \\
&\quad (IWC)^{\frac{7+m}{4+m}}
\end{aligned} \tag{4.2}
$$

where ρ is the ice bulk density and $\Gamma(\cdot)$ the Gamma function. IWC is defined as

$$
\begin{aligned}
IWC &= \frac{\pi}{6000} \rho \int D^3 N(D) dD \\
&= \frac{\pi}{6000} \frac{\Gamma(m+4)}{(m+3.672)^{m+4}} \rho D_0^{m+4} N_0
\end{aligned} \tag{4.3}
$$

Since the atmosphere is sparse media, the radar reflectivity should be proportional to IWC or ice particle concentration (N_t) for a given m and median diameter D_0 [65]. N_t is calculated by

$$
N_t = \int N(D) dD = N_0 \frac{\Gamma(m+1)}{(m+3.672)^{m+1}} D_0^{m+1} \tag{4.4}
$$

Using equation(4.1), (4.2) and (4.3), we have,

$$
IWC = \frac{\pi}{6000} \frac{\Gamma(m+4)}{\Gamma(m+1)} (m+3.672)^{-3} \rho D_0^3 N_t \tag{4.5}
$$

and

$$
Z_{hh} = 0.242 \frac{\Gamma(m+7)}{\Gamma(m+1)} (m+3.672)^{-6} \rho^{1.934} D_0^6 N_t \tag{4.6}
$$

or

$$
Z_{hh} = \frac{1452}{\pi} \frac{\Gamma(m+7)}{\Gamma(m+4)} (m+3.672)^{-3} \rho^{0.934} D_0^3 (IWC) \tag{4.7}
$$

The above equations offer us interesting insights into the Z_{hh} and IWC relationship. For fixed ρ and m, Z_{hh} and IWC are proportional to $D_0^6 N_t$ and $D_0^3 N_t$, respectively. This indicates that D_0^3 is an important source of ambiguity for the linear relationship between IWC and Z_{hh}. Given Z_{hh} measurements, we can have different IWC by changing D_0 and N_t on the line of $D_0^6 N_t = constant$. In other words, we can search IWC iteratively on

a $D_0^6 N_t$ line toward a desired value while keeping Z_{hh} unchanged. Figure 4.1 shows how such a search can be implemented on the $D_0 - N_t$ plane. Solid lines are $Z_{hh} = constant$ and dashed line $IWC = constant$. Following empirical rule is used in the plot:

- $\rho = 0.90$ if $Z_{hh} \leq -5dBz$
- $\rho = 0.60$ if $-5 < Z_{hh} \leq 0dBz$
- $\rho = 0.20$ if $0 < Z_{hh} \leq 10dBz$
- $\rho = 0.01$ if $Z_{hh} > 10dBz$

There are two reasons for us to use this empirical rule. First, from equation (4.6), the uncertainty of IWC introduced by bulk density is $\rho^{-0.934}$, which is much less than that by median diameter, D_0^{-3}; Second, as a first step our goal is to investigate possible ways to combine radar with radiometer, this empirical rule serve us as an approximation and can be modified later by incorporating more information.

The basic idea of our radar/radiometer method is, for a given radar reflectivity profile Z_{hh}, to construct an atmospheric component profile $[N_t(z), D_0(z), \rho(z)]$ that will:

1. reproduces the reflectivity profile,
2. gives an IWP as close to radiometer IWP retrieval as possible,
3. follows constraints imposed by cloud physics.

It is to be noted that imposing constraints is actually a way of incorporating different kinds of information into the combined retrieval algorithm. As an example, in case of snow aggregation, the ice particle size may increase when they fall onto the ground. In this dissertation, we only force the ice particle size and concentration to be in a reasonable range: $0.05mm \leq D_0 \leq 3.00\ mm$ and $0 \leq N_t \leq 3 \times 10^5\ m^{-3}$. Another important issue for this iterative method is the initial guess profile. As an ill-posed problem, radar/radiometer profiling heavily depend on initial guess since generally there is no very strong constraint to control the iterative procedure. In other words, different kind of initial guesses are needed for different problems. For stratiform rain over ocean, constant N_0 in equation (4.1) are often used [40]. For cases studied here, we chose constant D_0 profile as initial guess. This

assumption imply that the variation of radar reflectivity is mainly due to the change in ice particle concentration, rather than median diameter. If we take the radiometer retrieved ice water path IWP_{radiom} as a first guess for radar, then the initial guess of median diameter $D_{0-initial}$ can be found from

$$\begin{aligned} IWP_{radiom} &= \sum(IWC)\Delta z \\ &= 2.186 \times 10^{-3}(m+3.672)^3 \frac{\Gamma(m+4)}{\Gamma(m+7)} D_{0-initial}^{-3} \\ &\quad \cdot(\sum \rho^{-0.93476} Z_{hh}\Delta z) \end{aligned} \tag{4.8}$$

Based on this initial guess of D_0, we can distribute radiometer IWP retrieval proportionally according to Z_{hh} profile measured by radar. Then the iterative approach defined by equation (4.4) to (4.6) can be applied to find an ice water content profile which gives an IWP as close as possible to IWP_{radiom}.

In the above case, we only discussed ice clouds. similar equations can be obtained for liquid clouds,

$$LWC = \frac{\pi}{6000}\frac{\Gamma(m+4)}{\Gamma(m+1)}(m+3.672)^{-3} D_0^3 N_t \tag{4.9}$$

and

$$Z_{hh} = \frac{\Gamma(m+7)}{\Gamma(m+1)}(m+3.672)^{-6} D_0^6 N_t \tag{4.10}$$

or

$$Z_{hh} = \frac{6000}{\pi}\frac{\Gamma(m+7)}{\Gamma(m+4)}(m+3.672)^{-3} D_0^3 (LWC) \tag{4.11}$$

where $0 \leq D_0 \leq 100\mu m$, $0 \leq N_t \leq 1000/cm^3$ for clouds over land, and $0 \leq N_t \leq 200/cm^3$ over ocean.

4.2 Case Study

On 8 February 1994, a surge from the north went by Denver and the temperature dropped from 33 F to 17 F within an hour. Once the surge went through the area it got hung-up on the Palmer Divide, which is south of Eire. Overrunning led to the development of light snow over areas north of the Palmer Divide. Very little accumulation was noted with the snow; however, a quarter of inch did accumulate at Hudson, northwest of Eire. By

1800UTC most of the light snow had dissipated, but by this time convective snow showers forming over the Continental Divide began to advect over areas north of Fort Collins, Colorado. During the afternoon the convective bands continued to increase in intensity, with a mesonet station in Laramie, Wyoming reporting S_+ at 2030UTC.

From 1300UTC, both NOAA's three-channel radiometer and K-band radar were up and operating at Eire, Colorado. We processed radiometer measurements to retrieve water vapor, cloud liquid and ice using our 3-channel neural network model. The water vapor and cloud liquid retrievals are plotted on Figure 4.2 and Figure 4.3; and, not surprisingly, they agree with NOAA's retrievals very well. Figure 4.4 shows radar observations of reflectivity, circular depolarization ratio, velocity, and correlation at 2029 UTC. The circular depolarization ratio shows very nicely the depolarization signature of ice clouds for the first cloud layer, which indicates that the observed clouds were ice clouds. Since the second and third layers do not show any depolarization signature, they should be liquid clouds. The ice microphysics can be profiled using radar/radiometer method of this dissertation. Figure 4.5 plots retrieved ice information. The solid line is IWP inverted from radiometer only, and the dashed line from radar/radiometer method. As we can see, the two methods generally agree on the IWP retrievals. Figure 4.6 shows the microphysics profile at 2029UTC. The retrieved median diameter is much larger at first cloud layer, ice cloud, than at the second and third layer, liquid cloud. It is to be noted that this size information is not imposed in our combined method, but expected by the microphysics. Therefore our radar/radiometer method as a first step is quite satisfactory.

Although the combined method is still premature and needs improvements, it should be consistent with some existing research results. For example, equation (4.2) is often used to explain why most empircal $Z_{hh} - IWP$ relationship is in the form of power law, instead of linear function. In other words,

$$Z_{hh}(dBz) = C_1 + C_2 \log(IWC) \tag{4.12}$$

where C_1 is a constant, and C_2 the slope. From most used equation (4.2), $C_2 = 10\frac{m+7}{m+4}$; but $C_2 = 10$ from equation (4.7). At first look, equation (4.7) seems not to explain why $C_2 \neq 10$ for most empircal rules. However, this deviation of C_2 from 10 is due to the uncertainty introduced by D_0^3 and $\rho^{0.934}$. If we plot equation (4.7) on a Z_{hh} (dBz) and $\log(IWC)$ plane, we would get a linear relationship for a fixed D_0 and ρ. By changing D_0 and ρ, we will get a set of parallel lines with slope of 10. However, when we randomly sample the

relationship of equation (4.7), our sampling points will not stay on just one of the lines. As a result, an empirical fitted line usually has a slope different from 10. In other words, C_1 and C_2 of equation (4.12) depend on sampling technique or experiment data sets used to find the empircal relationship between Z_{hh} and IWC. To illustrate above, we took the radar reflectivity profile measured at 2000UTC, and plotted it against retrieved IWC from radar/radiometer method. We know that each point of this plot satisfyies equation (4.7). We then linearly fit this scatter plot. As shown in Figure 4.7, the fitted line has a slope of 10. Other published empirical rules were also plotted on Figure 4.7 for comparison. Good agreements are evident. To show how the fitted slope can change, we then fit the IWC and Z_h relationship using several retrieved IWC profile from different time period. The new fitted line, $Z_h = 7.3512 + 13.185 \log(IWC)$, has a slope of 13.185 as shown in Figure 4.8.

It is to be noted that published empircal $Z_h - IWC$ relationship is based on forward problems: calculations of radar reflectivities from known size distribution spectra [38]. In this dissertation, our regression $Z_h - IWC$ relationship is based on an inverse problem: retrievals of size distribution spectrum parameters using radar/radiometer method.

It is more interesting and straightforward to apply our radar/radiometer method to study the liquid clouds. First, retrieval of liquid water path using radiometer is an estabilished technique; the retrieval accuracy is widely accepted. Second, liquid cloud droplets are small in size and spherical in shape, Rayleigh approximation always holds.

On Feburary 7, 1994. NOAA's K-band radar observed clearly a layer of liquid between 1149 — 1329 UTC. Figure 4.9 shows a radar measurement example taken around 1149UTC. On this radar picture, there is no depolarization signature of ice cloud, and the radar reflectivities are in the range of -20 to -35 dBz. Figure 4.10 plots the cloud liquid retrieval from both 2-channel radiometer model and radar/radiometer method. As we can see, two methods agree exactly on the LWP retrievals. This is different from ice cloud case in Figure 4.5, where IWP retrievals by these two methods are not equal. Figure 4.11 depicts the retrieved microphysics profiles at 1149UTC. To get a regression $Z_h - LWC$ relationship, we selected four radar reflectivity and microphysics profiles at 1149-1216-1259-1309UTC, and plotted $Z_h - LWC$ scattergraph in Figure 4.12. The regression line of this scatter plot is $Z_h = -16.89 + 11.214 \log(LWC)$. For comparison, the $Z_h - LWC$ relationships from Atlas [1] and Sauvageot et al. [53] are also presented in Figure 4.12. Once again, all regression line are in general agreement.

4.3 Model validation using aircraft data

On 8 March 1994, a layer of homogeneous liquid cloud with all size droplets was formed between Erie and Fort Collins, Colorado. Around 0013UTC, the Kingair of the University of Wyoming overflew NOAA three-channel radiometer and K-band radar at Erie at an altitude of 900 M AGL. Several microphysics probes were on board measuring the size spectra of cloud droplets. The radar and radiometer were not, however, operated coordinately with this overflight of Kingair. Figure 4.13 shows closest RHI scan of radar at 0009UTC. Radar reflectivity was $-4.7109\ dBz$ at 925 M above the radar. Radiometer was pointed vertically at 0009UTC, and gives columnar water vapor and cloud water to 0.551 cm and 0.3449 mm, respectively. Figure 4.14 depicts the aircraft in situ measurements of cloud drop size spectra. The corresponding size spectra obtained from combined radar/radiometer method is plotted in Figure 4.15. Very good agreement between aircraft in situ measurement and combined radar/radiometer method is evident from these two plots.

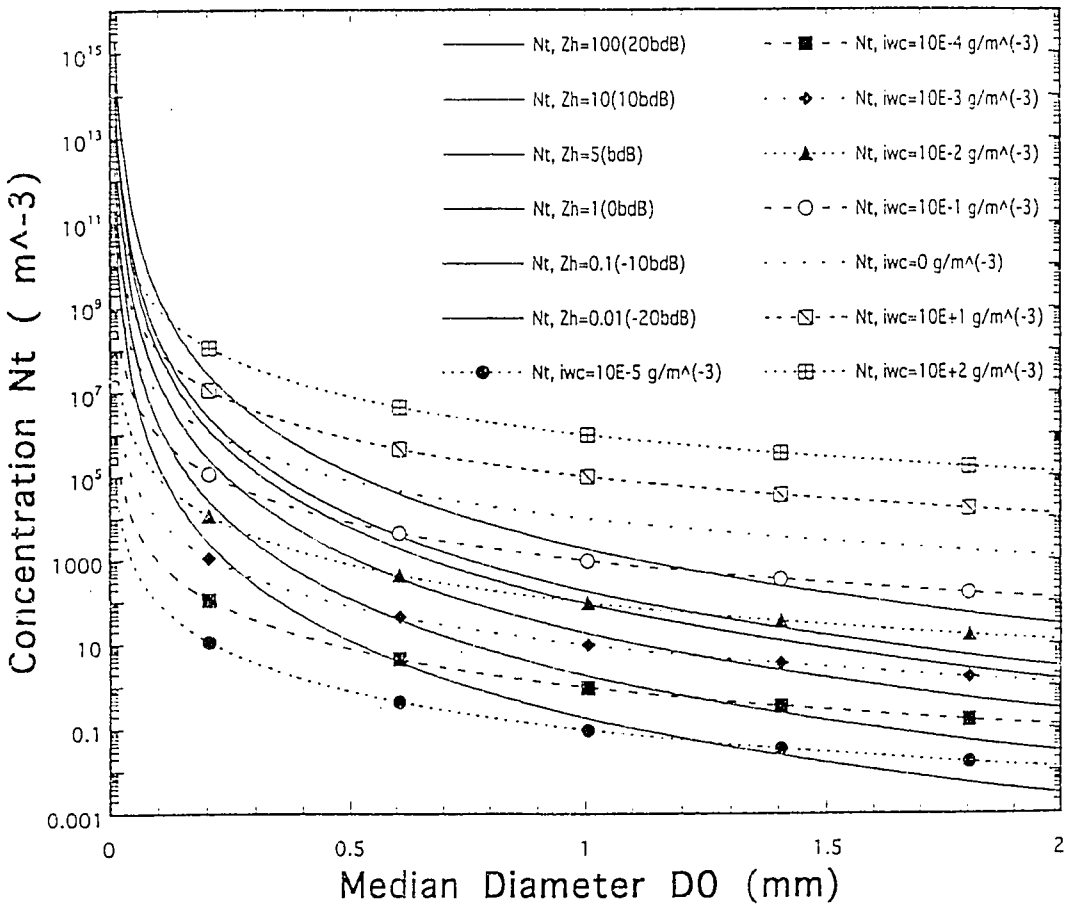

Figure 4.1: Contour plots of radar reflectivity of ice water content on the plane of particle concentration (N_t) and median diameter (D_0).

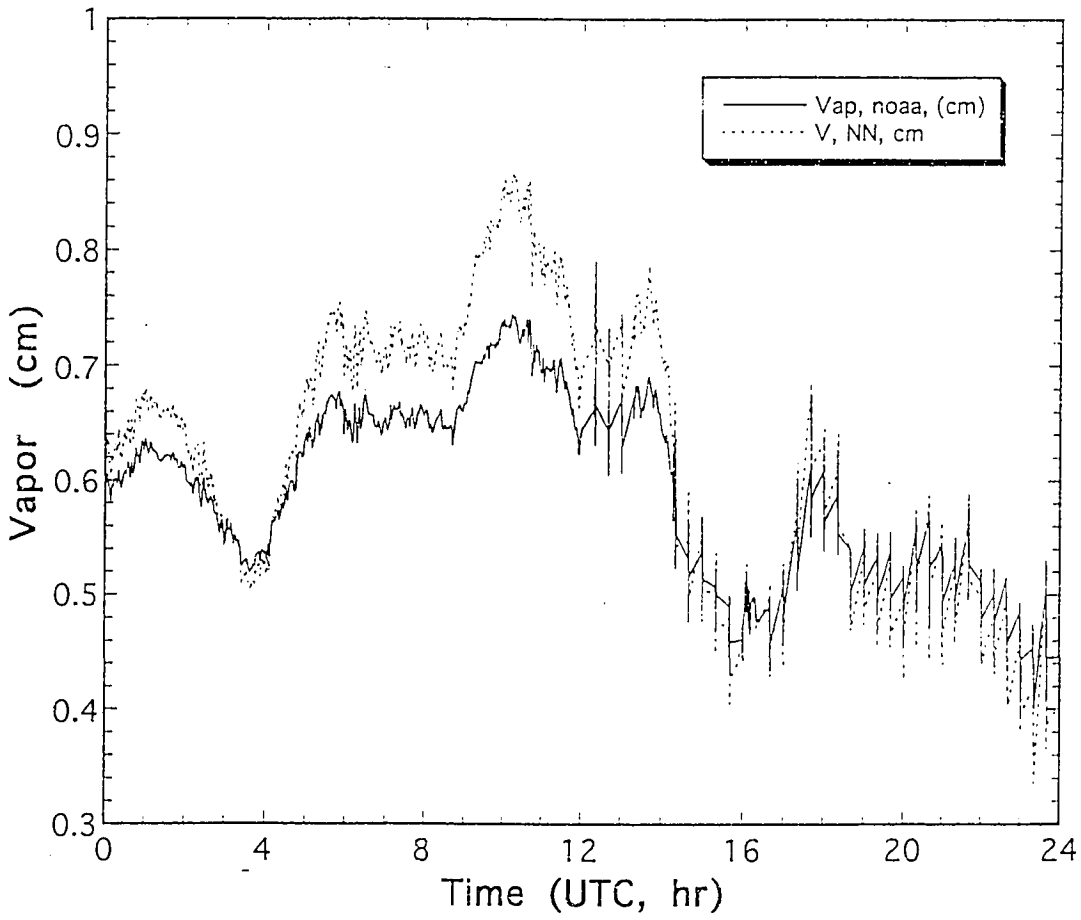

Figure 4.2: Comparison of water vapor retrieval from three-channel radiometer between physical inverse model and NOAA's statistical model. Radiometer data were taken on 8 February 1994 at Erie, Colorado.

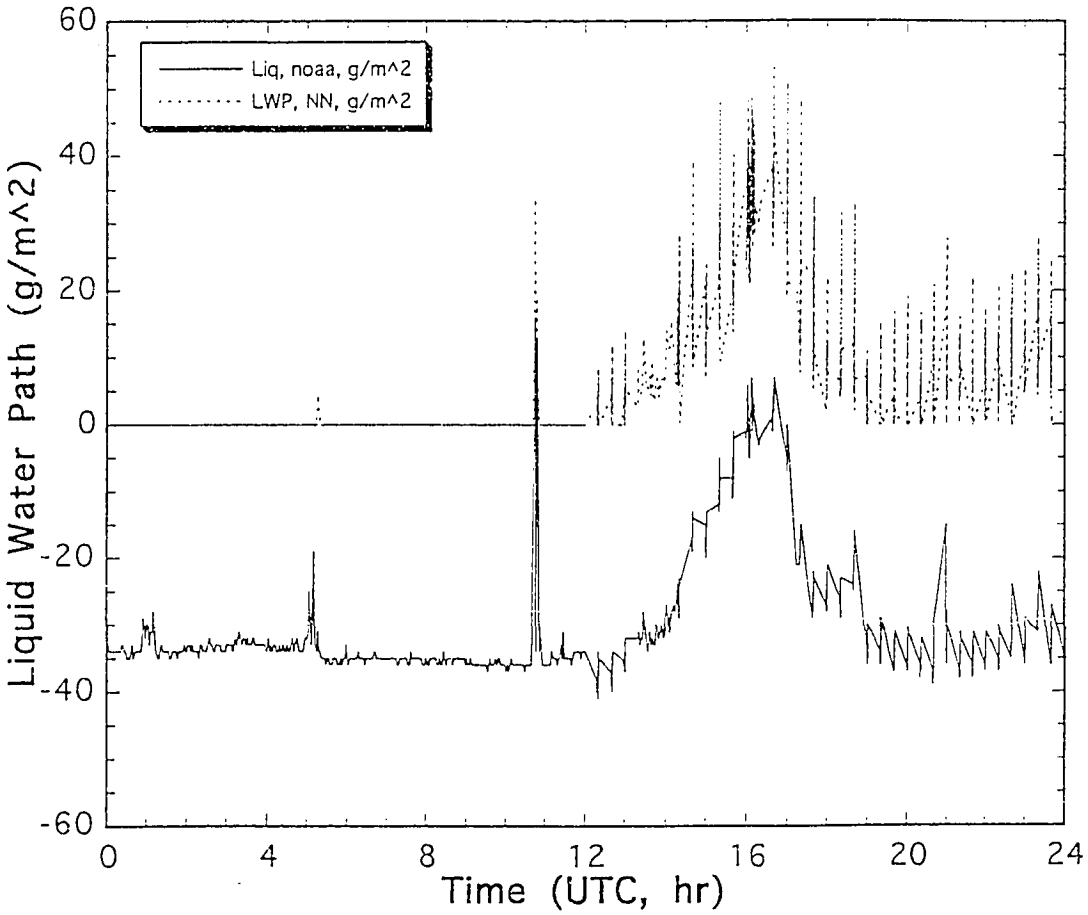

Figure 4.3: Comparison of cloud liquid water retrieval from three-channel radiometer between physical inverse model and NOAA's statistical model. Radiometer data were taken on 8 February 1994 at Erie, Colorado.

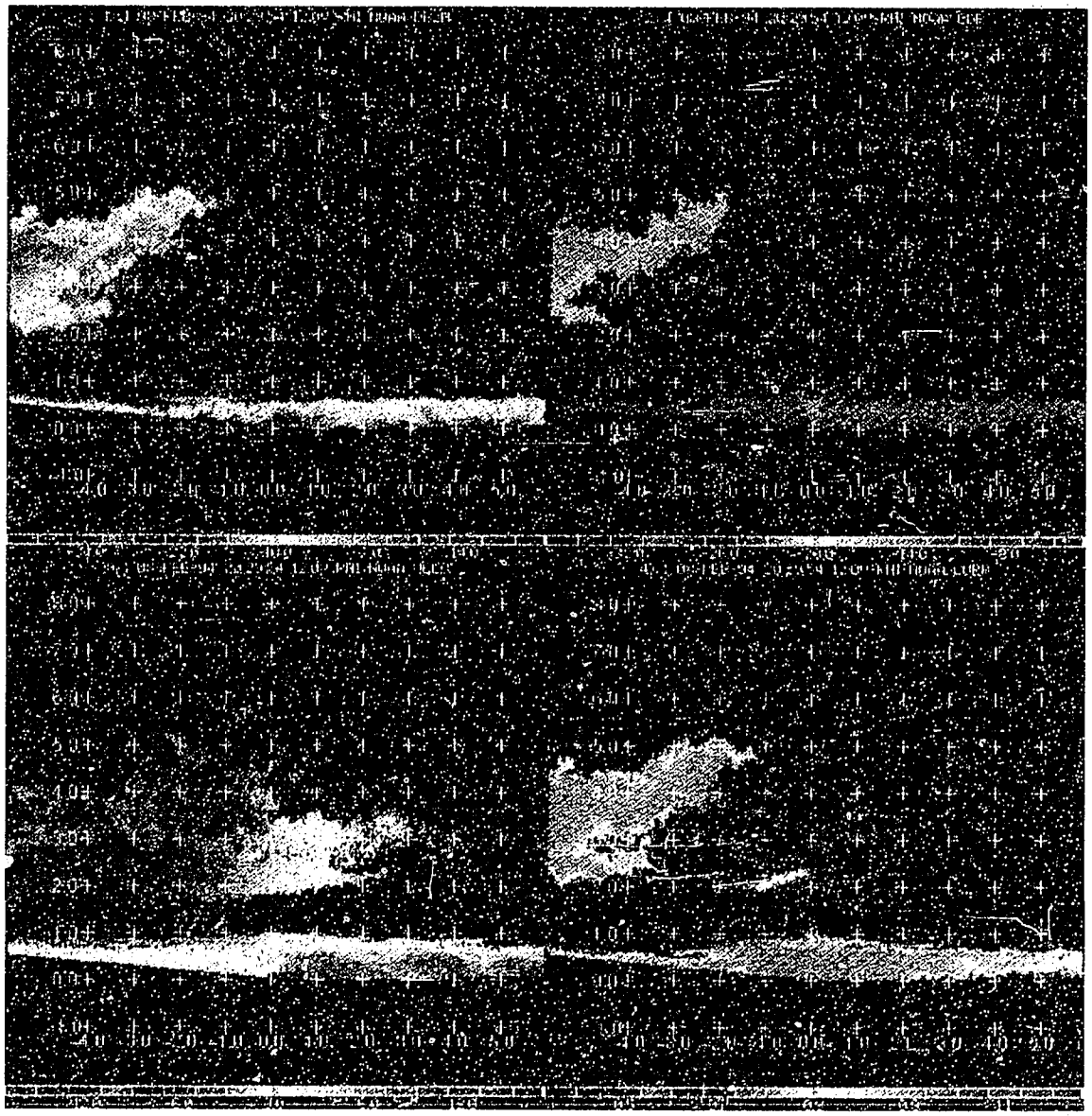

Figure 4.4: Radar observations of reflectivity, circular depolarization ratio, velocity and correlation by NOAA K-band radar on 2029UTC at 8 February 1994 at Erie, Colorado.

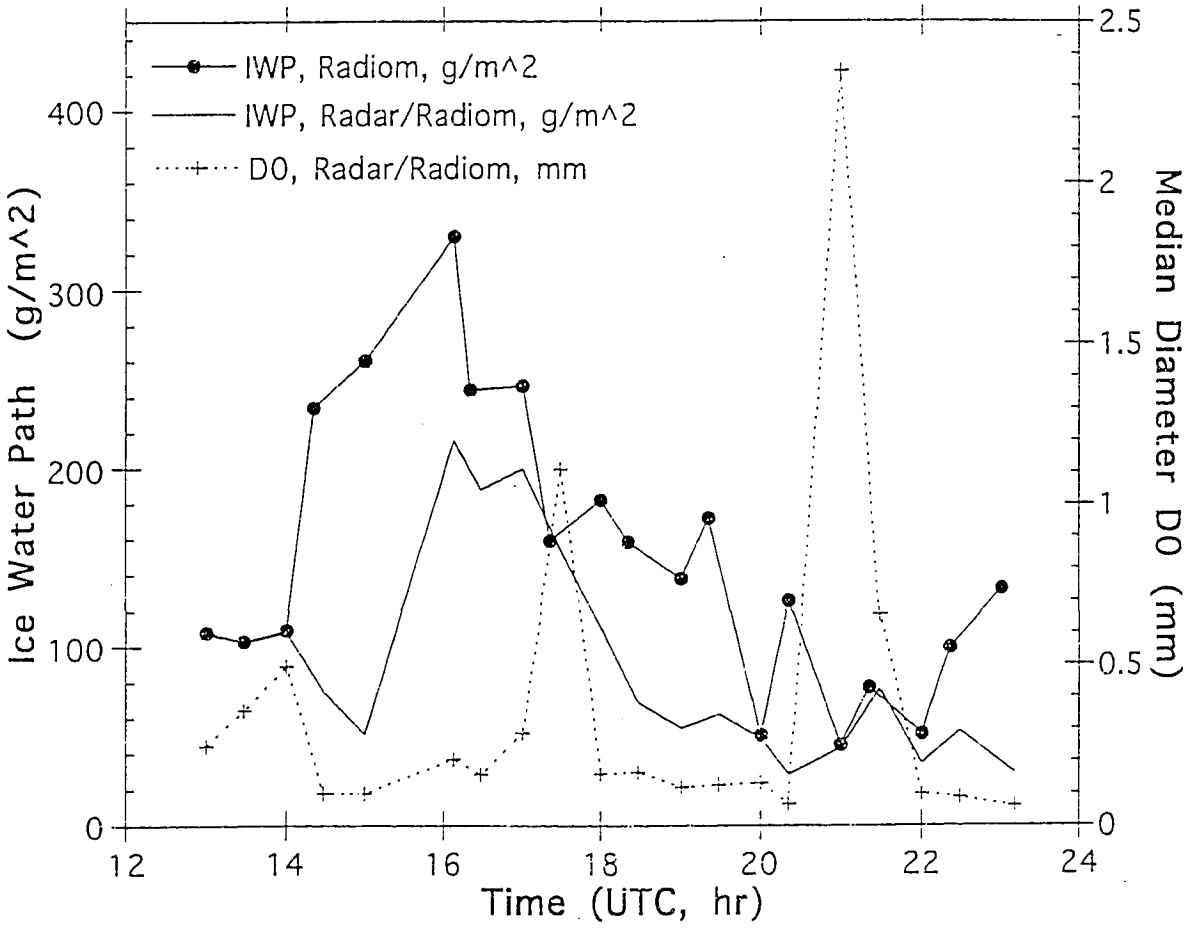

Figure 4.5: Ice water path and median diameter retrievals from three-channel radiometer and combined radar/radiometer method.

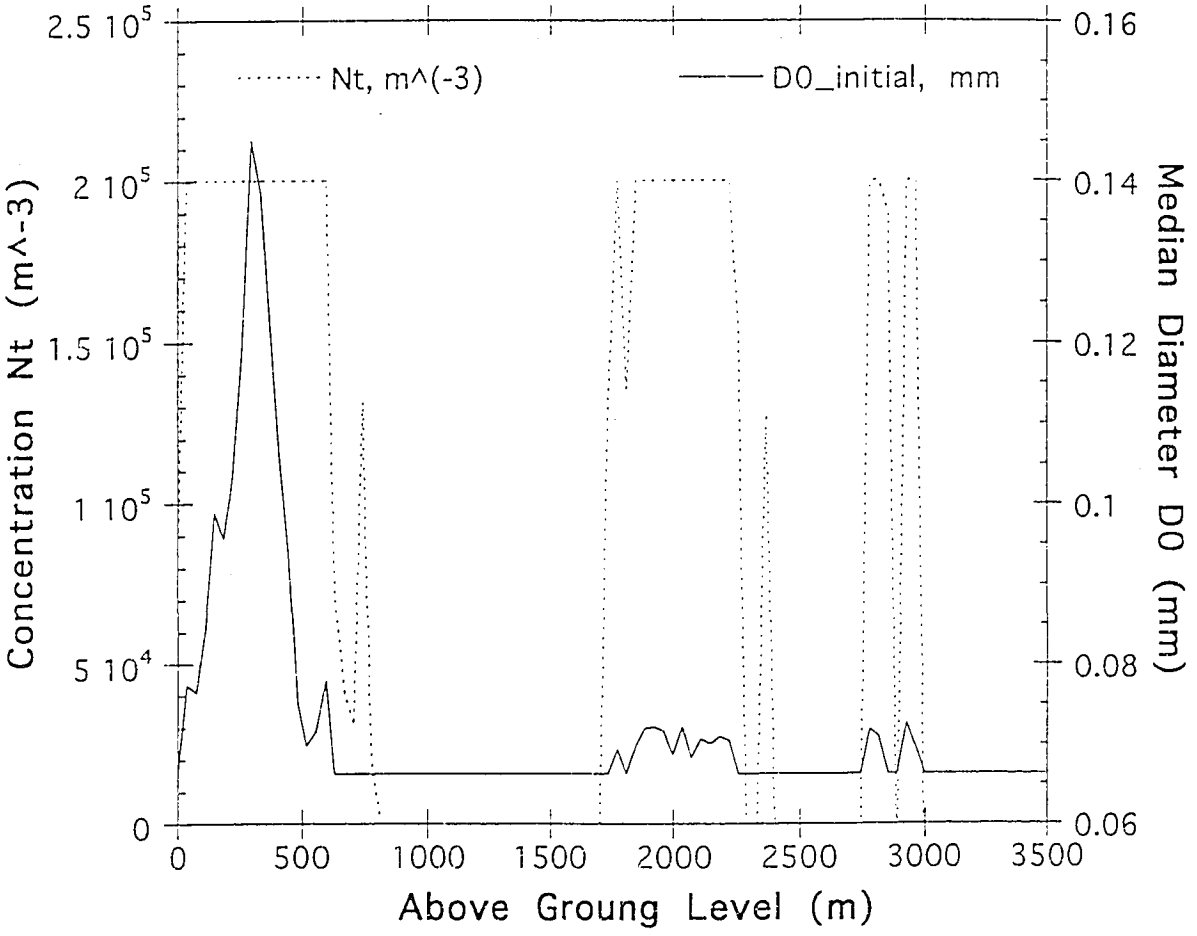

Figure 4.6: An example of retrieved profiles of ice particle concentration and median diameter.

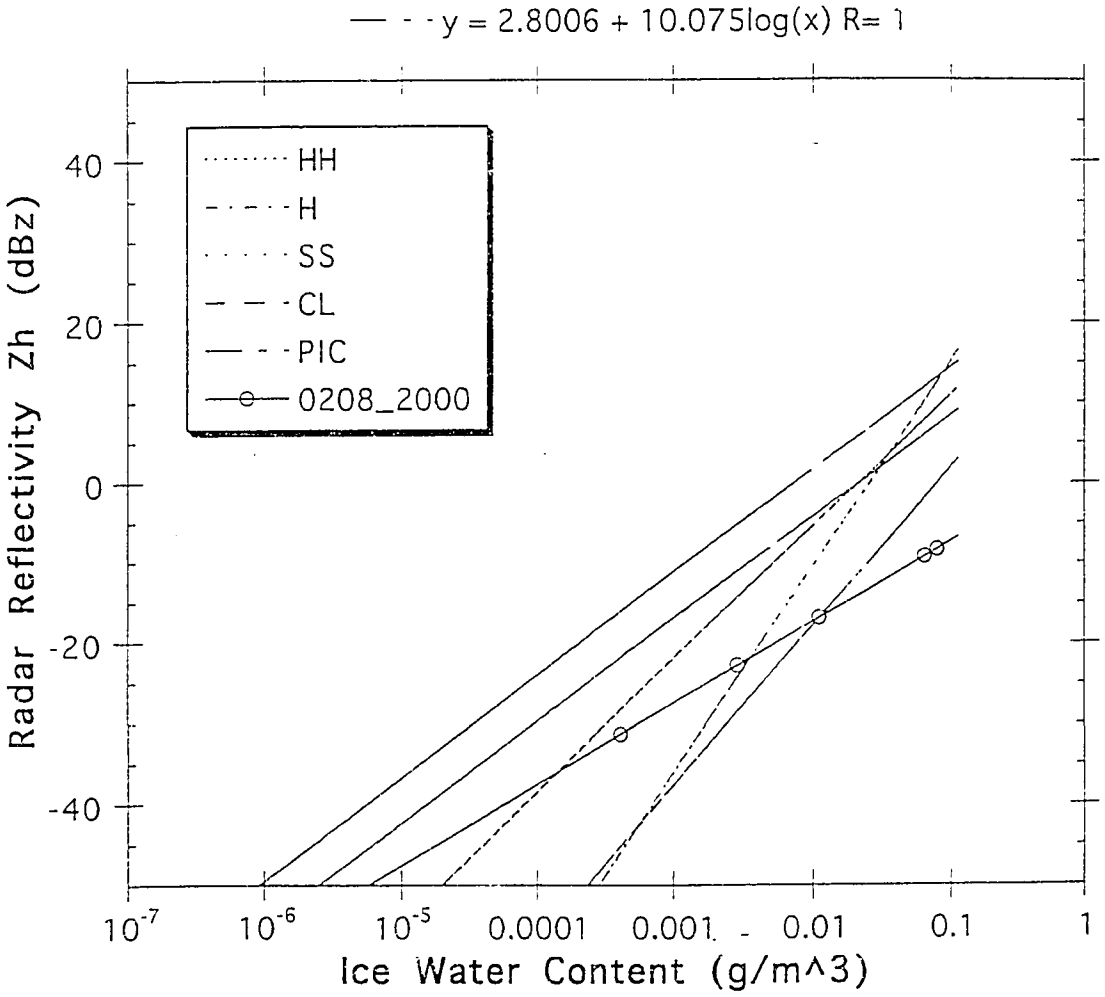

Figure 4.7: Empirical relationship between radar reflectivity and ice water content from vertical profiles of microphysics on 2000UTC 8 February 1994 by combined radar/radiometer method. Other published empirical relationship (HH, H, SS, CL, PIC) are presented for comparison.

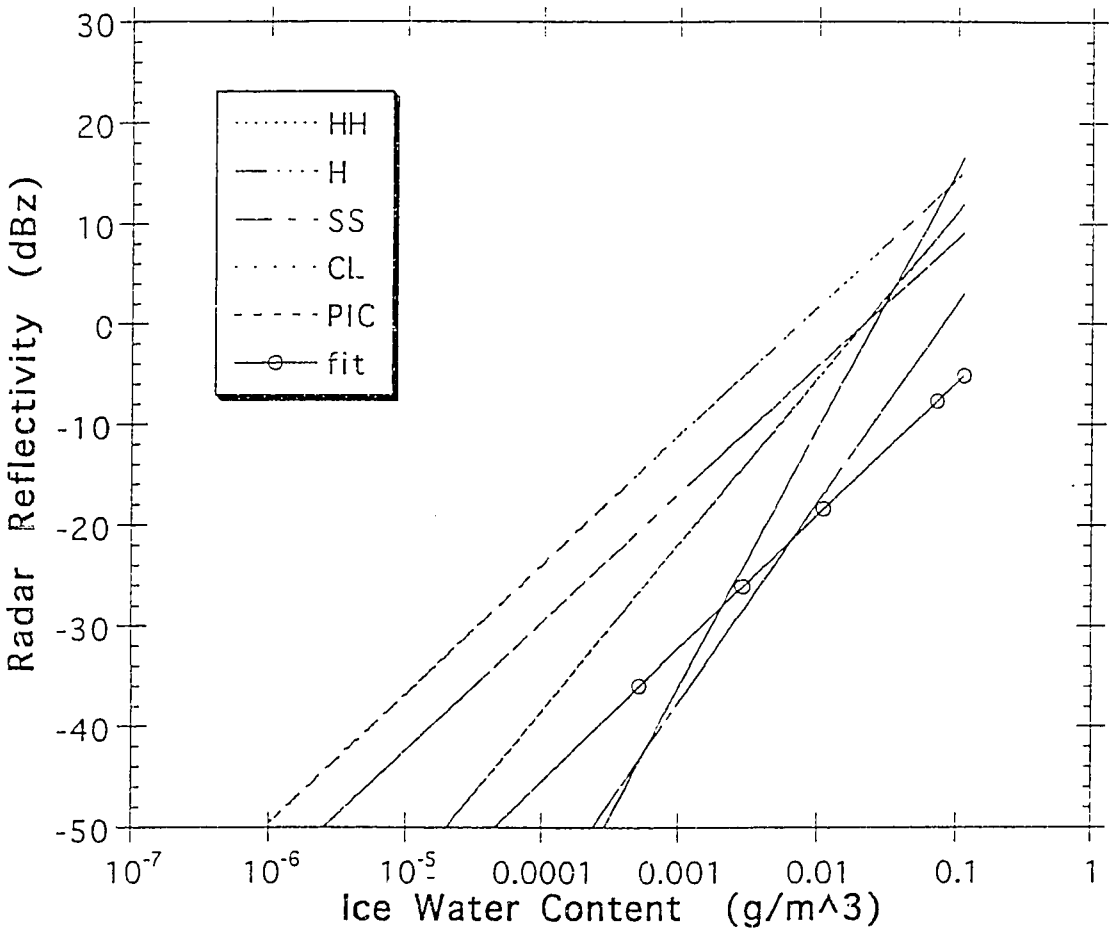

Figure 4.8: Empirical relationship between radar reflectivity and ice water content from several vertical profiles of microphysics on 8 February 1994 by combined radar/radiometer method. Other published empirical relationship (HH, H, SS, CL, PIC) are presented for comparison.

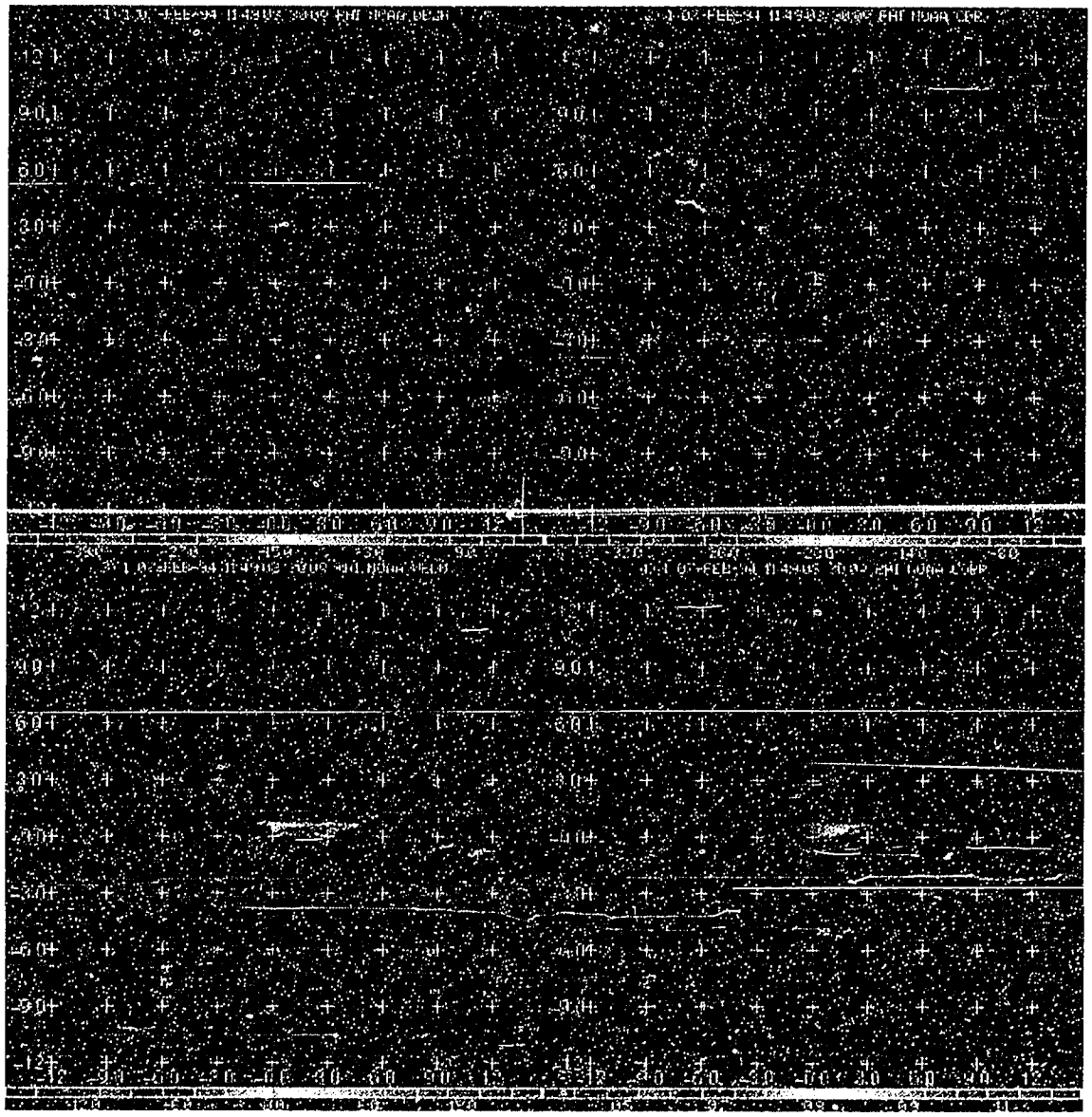

Figure 4.9: Radar observations of reflectivity, circular depolarization ratio, velocity and correlation by NOAA K-band radar on 1149UTC at 7 February 1994 at Erie, Colorado.

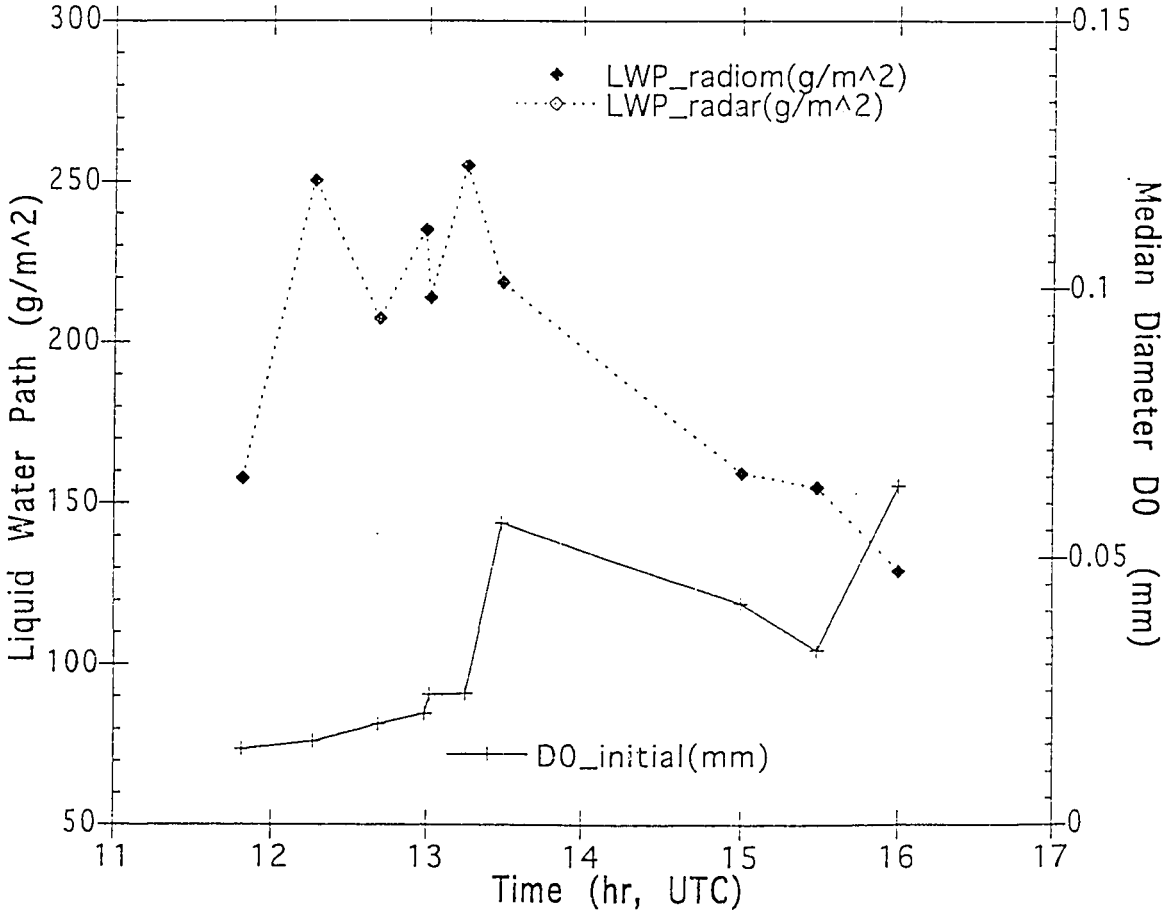

Figure 4.10: Liquid water path and median diameter retrievals from radiometer and combined radar/radiometer method.

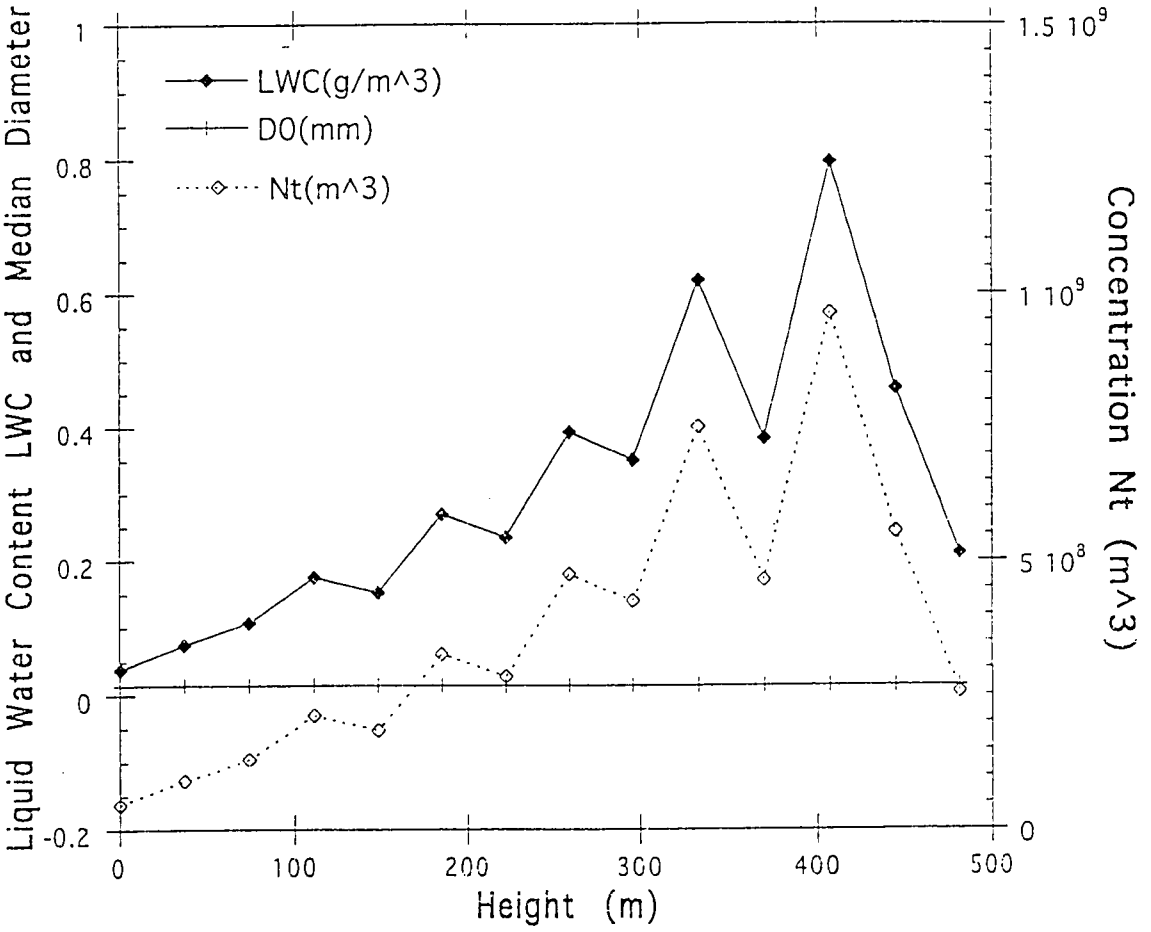

Figure 4.11: An example of retrieved profiles of liquid droplet concentration, median diameter, and cloud liquid water content.

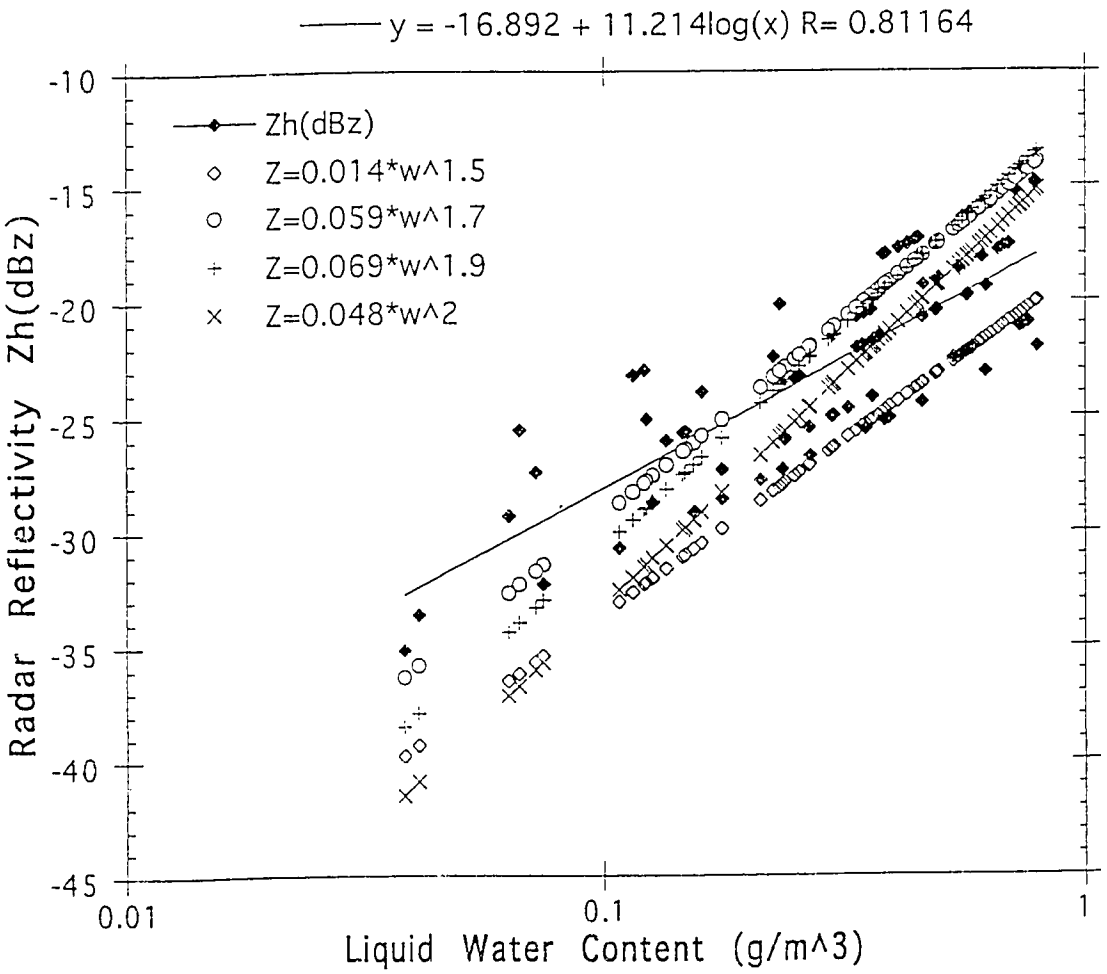

Figure 4.12: Empirical relationship between radar reflectivity and liquid water content from several vertical profiles of microphysics on 7 February 1994 by combined radar/radiometer method ($Z - h(fit)$). Other published empirical relationship are presented for comparison.

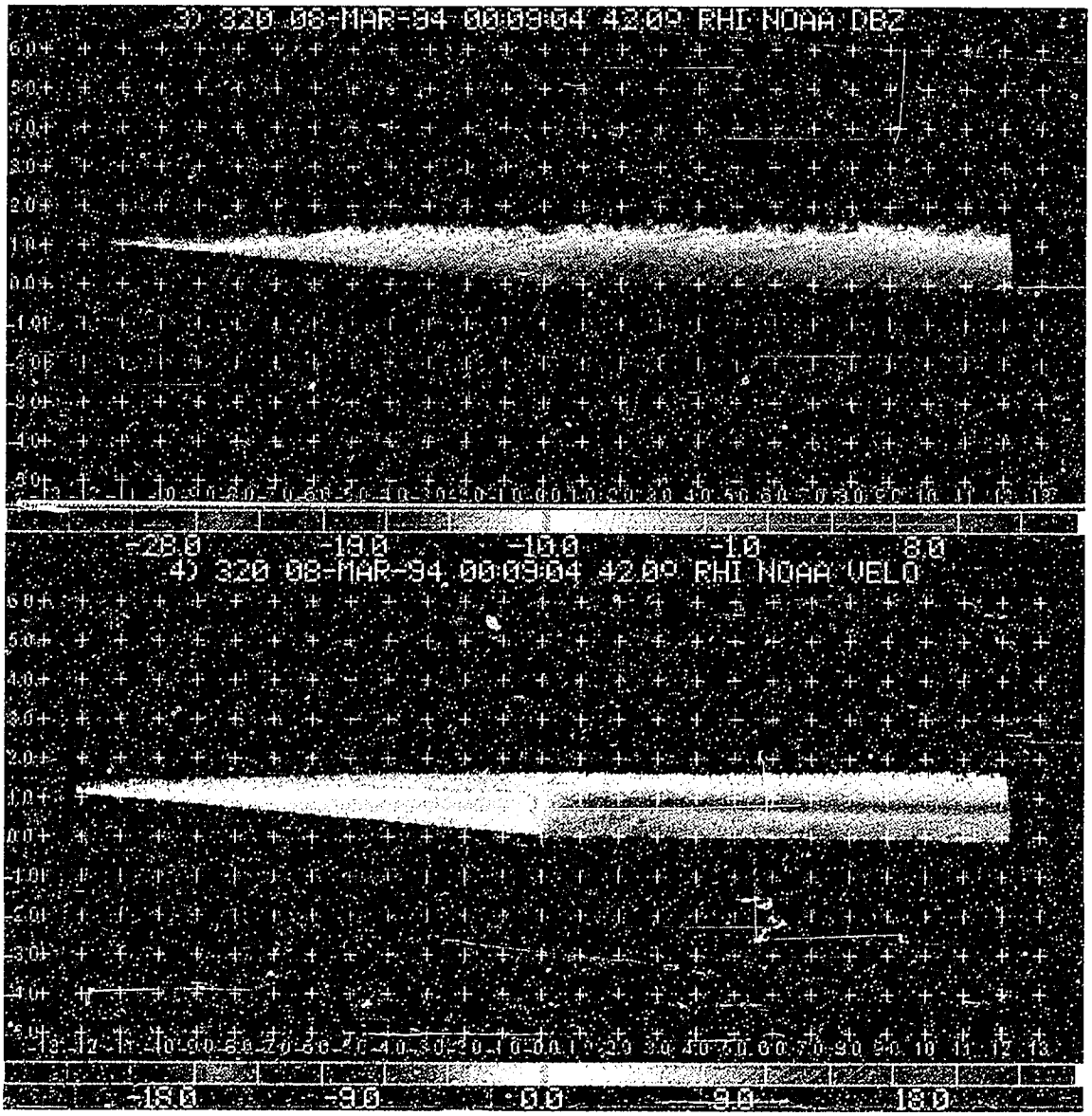

Figure 4.13: Radar observations of reflectivity and velocity by NOAA K-band radar on 0009UTC 8 March 1994 at Erie, Colorado.

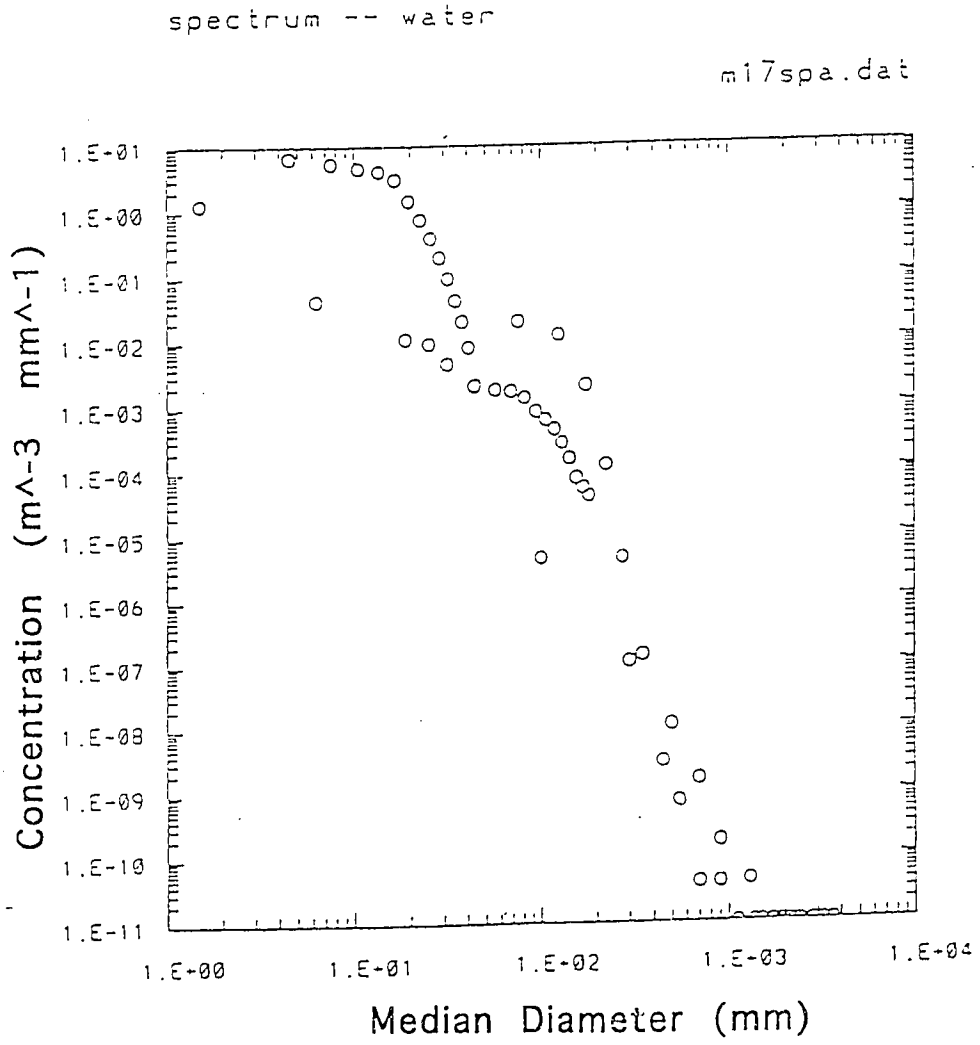

Figure 4.14: Aircraft in situ measurements of liquid cloud drop size spectra. Aircraft overflow 900 m above NOAA radar and radiometer at 0013UTC 8 March 1994.

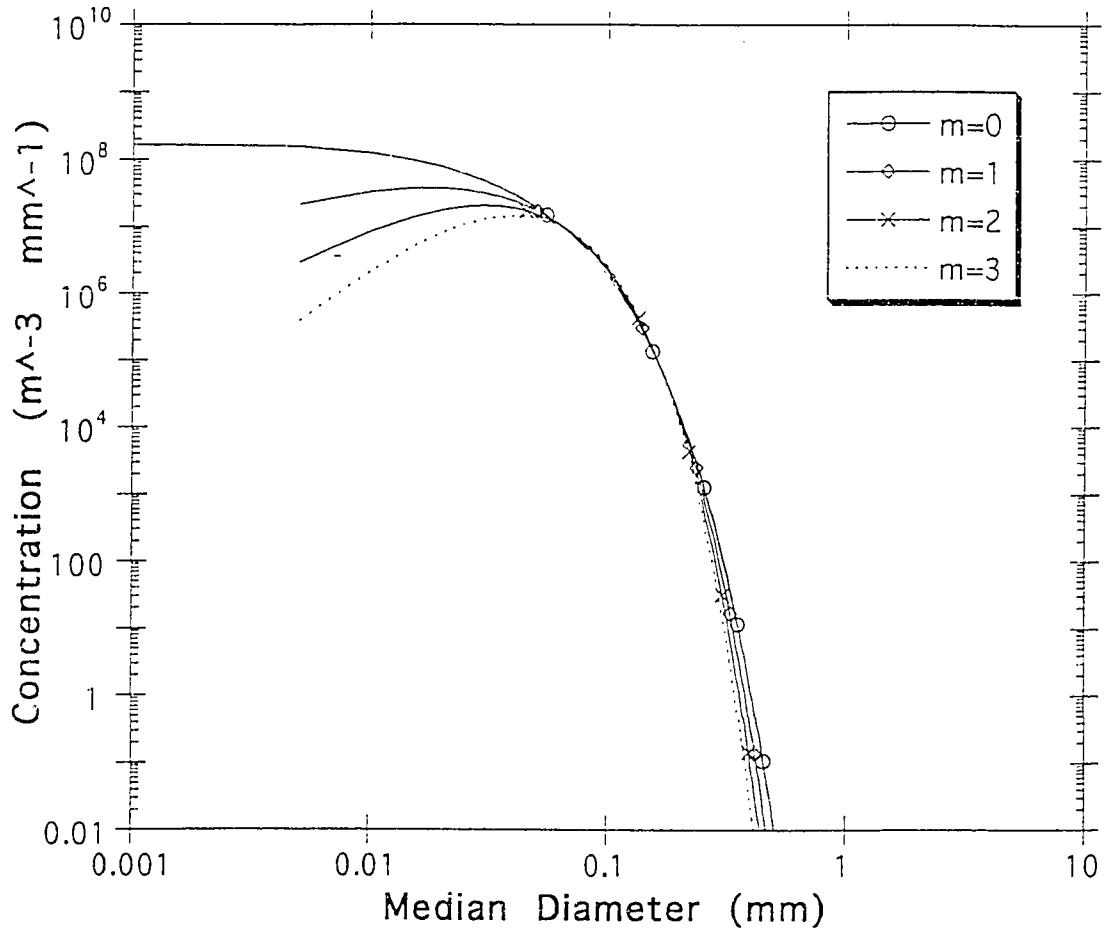

Figure 4.15: Drop size spectra retrieved from radar/radiometer method. The measured volume of liquid cloud is 925 m above the radar at 0009UTC 8 March 1994.

Chapter 5

CONCLUSION

In chapter 2, three techniques are used to solve the vector radiative transfer equations: the iterative method, the discrete ordinate-eigenanalysis method and the invariant imbedding method. Validation of these three methods are obtained by comparing them against each other and against published results on several different cases. The iterative method gives a closed form solution and physical insight into the emission and scattering processes, but it can be used only for cases of small albedo or optical depth. The discrete ordinate-eigenanalysis and invariant imbedding techniques divide the vertical structure of the media into a number of homogeneous layers. They can be used for general albedo and optical depths. Discrete ordinate-eigenanalysis method is applicable only for homogeneous temperature profile. For media with inhomogeneous temperature profiles, the invariant imbedding method is appropriate.

In chapter 3 of this dissertation, we present a neural network-based physical inverse approach and applied it to two- and three-channel ground-based radiometers (20.6, 31.65 and 90 GHz). Our inverse models retrieve vertically integrated water vapor, cloud liquid water and ice water content simultaneously. Excellent model validations on water vapor and liquid water paths are obtained based on NOAA's statistical inverse models. As a physical model, it can provide physical insight into the radiative transfer processes, hence, can be used as a simulation tool in enhancing our understanding of existing radiometer algorithms and designing new radiometers. Also, it does not require distinct microwave signatures and can incorporate ground truth and address the uniqueness of inversion. Most importantly, this approach does not depend on in situ measurements. In other words, a radiosonde data base is not required to develop an inverse model. Therefore, this method is very cheap and fast.

Although we are mainly focused on ground-based radiometer and radar in this work, it is straightforward to apply this method to airborne and/or spaceborne cases. Compared with other existing models, this new approach emphasize physical modeling while opening doors for integrations of different measurements and constraints of cloud physics. In

other words, this method offers a potential approach to combine physical inverse models with climatological statiscs, surface meteorology observable constraints and/or cloud microphysics.

We also proposed a combined radar/radiometer method to vertically profile cloud microphysics. We examined the $Z_h - IWC$ relationships on a $N_t - D_0$ plane and identified D_0^3 as an important source of ambiguity for the empirical $Z_h - IWC$ relationship. Retrievals of integrated ice water and liquid water content from radiometers are vertically distributed according to radar measurements to obtain cloud microphysics profiles. These profiles are then used as initial guess and adjusted iteratively to search desired microphysics profiles which are consistent with radar measurements. In a case study of liquid cloud, it is found that this radar/radiometer technique agrees very well with aircraft in situ measurement of cloud liquid drop size spectra. Case studies of both liquid and ice clouds also show that this combined method is consistent with other published studies on the $Z_h - LWC$ and $Z_h - IWC$ relationships. This consistency is very welcome especially when one considers that empirical relationships of this dissertation are based on inverse problem: retrievals of cloud microphysics from radar and radiometer measurements. On the other hand, complete consistency between radar and radiometer is achieved only for liquid, but not for ice, cloud. The consistency between radar and radiometer is necessary, but not sufficient, for any physical inversion by combined radar/radiometer method. Some airborne remote sensing projects, like TOGA COARE and TRMM, could provide a better platform to advance this method. Those projects are designed for combined radar/radiometer remote sensing of precipitation systems.

BIBLIOGRAPHY

[1] Atlas, D., the estimation of cloud parameters by radar, J. Meteoro., Vol. 11, 309-317, 1954.

[2] Askne, J.I.H., E.R.Westwater, A review of ground-based remote Sensing of temperature and moisture by passive microwave radiometry, IEEE Trans. Geosci. Remote Sensing, Vol. GE-24, 340-352,1986.

[3] Bauer, P.,P. Schluessel, Rainfall, total water, ice water, and water vapor over sea from polarized microwave simulations and Special Sensor Microwave/Imager data, J. Geophys Res. Vol.98, 20,737-20,759, 1993.

[4] Blaskovic, M., B. E. Sheppard, R. R. Rogers and T. C. Box, Radiometric observations during the Canadian Atlantic Stroms Program, J. Atmos. Oceanic Technol., 6 109-120, 1989.

[5] Clifford, S.F., J.C.Kaimal, R.J.Lataitis, and R.G.Strauch, Ground-based remote profiling in atmospheric studies: An overiew, Proc. IEEE, Vol.82, No3, 313-355,1994.

[6] Davis, D. T., Z. Chen, L. Tsang, J. H. Hwang, A. T. C. Chang, Retrieval of snow parameters by iterative inversion of a neural network, IEEE Trans. on Geoscience and Remote Sensing, vol. 31, no. 4, 842-852, 1993.

[7] Deirmendjian, D.,Electromagnetic Scattoring on spherical polydispersions, New York: American Elsevier Publishing Company, Inc., 1969.

[8] Doviak, R. J., and Dusan S. Zrnic, Doppler Radar and Weather Observations, Second Edition, Academic Press, Inc. 1993.

[9] Evans, K. F., some theoretical calculations concerning microwave remote sensing of cirrus, technique report, Department of Atmospheric Science, Colorado State University, May 12, 1989.

[10] Evans, K. F., Microwave remote sensing algorithm for cirrus clouds and precipitation, Ph.D dissertations, Colorado State University, 1993.

[11] Evans, K. F., and J. Vivekanandan, Multiparameter radar and microwave radiative transfer modeling of nonspherical atmospheric ice particles, IEEE Trans. Geosci. and Remote Sensing, vol. 28, no. 4, 423-437, 1990.

[12] Gasiewski, A. J., Microwave radiative transfer in hydrometeors, Ch. 3 of Atmospheric Remote Sensing by Microwave Radiometry, edited by M. A. Janssen, New York: John Wiley & Sons, 1993.

[13] Goedecke, G. H. and S. G. O'Brien, Scattering by irregular inhomogeneous particles via the digitized Green's function algorithm, Appl. Optics, vol. 27, n. 12, 2431-2437, 1988.

[14] Guiraud, F. O., J. Howard and D. C. Hogg, A dual-channel microwave radiometer for measurement of precipitable water vapor and liquid, *IEEE Trans. Geosci. Electron.*, 17, 129-136, 1979.

[15] Han, Y., J. B. Snider, E. R. Westwater, S. H. Melfi, and R. A. Ferrare, Observation of water vapor by ground-based microwave radiometers and Raman lidar, accepted by J. Geophys. Res., 1994.

[16] Heymsfield, A. J. and A. G. Palmer, Relationship for deriving Thunderstorm anvil ice mass for CCOPE storm water budget estimates, J. Climate and Applied Meteorology, Vol. 25, 691-702, 1986.

[17] Hill, G. E., Measurement of atmospheric liquid water by a ground-based single-frequency microwave radiometer, J. Atmos. Oceanic Technol., 8, 685-609, 1991.

[18] Hobbs, P.V., J.M. Wallance, Atmospheric Science: An introductory survey, New York: John Wiley & Sons, 1977.

[19] Hoehne, W., Precision of National Weather Service upper air measurements, NOAA Tech. Memo. NWS T & ED-16, Nat. Weather Service, Washington, DC, 1980.

[20] Hogg, D. C., F. O. Guiraud, J. B. Snider, M. T. Decker and E. R. Westwater, A steerable dual-channel microwave radiometer for measurement of water vapor and liquid in the troposphere, J. Climate Appl. Meteor., 22, 789-806, 1983.

[21] Hornik, K., Multilayer feedforward networks are universal approximators, Neural Networks, vol. 2, no. 5, 359-366, 1989.

[22] Ishimaru, A., Electromagnetic wave propogation, radiation, and scattering, Prentice Hall, 1991.

[23] Ishimaru, A., R. J. Marks, II, L. Tsang, C. M. Lam, and D. C. Park, Particle size distribution determination using optical sensing and neural networks, Opt. Lett., vol. 15, no. 21, 1221-1223, 1990.

[24] Ishimaru, A., Wave Propagation and Scattering in Random Media, Volumes 1 and 2, New York: Academic, 1978.

[25] Jordan, M. I., D. E. Rumelhart, Forward models: Supervised learning with a distal teacher, Cognitive Science,

[26] Kozu, T., K. Nakamura, R. Meneghini, W. C. Boncyk, Dual-parameter radar rainfall measurement from space: a test result from an aircraft experiment, *IEEE Trans. Geosci. Remote Sens.*, GE-29, 690-703, 1991.

[27] Kumagai, H., R. Meneghini, and J. R. Wang, Combined analysis of airborne single-frequency radar and multi-frequency radiometer observations in the TRMM-1 experiment, 26th Internat. Conf. on Radar Meteor., Norman, OK, 696-698, 1993.

[28] Kummerow, C. and L. Giglio, A passive microwave technique for estimating rainfall and vertical structure information from space. Part I: Algorithm, J. Applied Meteorology, Vol. 33, No. 1, 3-18, 1994.

[29] Kummerow, C., I. M. Hakkarinen, H. F. Pierce, and J. A. Weinman, Determination of precipitation profiles from airborne passive microwave radiometric measurements, J. Atmos. Ocean. Tech. Vol. 8 148-158, 1991.

[30] Li, L., J. Vivekanandan, C. Chan, and L. Tsang, Microwave radiometer technique to retrieve vapor, liquid and ice, Part I: Development of Neural Network based physical inversion method, submitted to IEEE Trans. on Geoscience and Remote Sensing, 1994.

[31] Li, L., J. Vivekanandan, C. H. Chan, and L. Tsang, Studies on passive remote sensing of ice and liquid water paths, IGARSS'94, Aug. 8-12, JPL, Pasadena, California, 1994.

[32] Li, L., C. H. Chan, and L. Tsang, Numerical simulation of conical diffraction of tapered electromagnetic waves from random rough surfaces and applications to passive remote sensing, Radio Sci., Vol. 29, No. 3, 587-598, 1994a

[33] Li, L., C. H. Chan, L. Tsang, K. Pak, P. Phu, S. H. Lou, Monte carlo simulation and backscattering enhancement of random metallic rough surface at optical frequencies, J. Electromagn. Wave Appl., Vol. 8, No. 3, 277-293, 1994b.

[34] Liao, L. and K. Sassen, Investigation of relationship between Ka-band radar reflectivity and ice and liquid water contents, Atmospheric Research, Vol. 34, 231-248, 1994.

[35] Liebe, H. J., MPM– An atmospheric millimeter-wave propagation model, Int. J. Infrared Millimeter Waves, 10, 631-650, 1989.

[36] Liu, G. and J. Curry, Retrieval of precipitation from satellite microwave measurement using both emission and scattering, J. Geophys. Res., Vol. 97, 9959-9974, 1992.

[37] Marzoug, M. and P. Amayenc, Improved range profiling algorithms of rainfall rate from a spaceborne radar with path-integrated attenuation constraint, *IEEE Trans. Geosci. Remote Sens.*, GE-29, 584-592, 1991.

[38] Matrosov, S. Y., radar reflectivity in snowfall, IEEE Trans. Geoscience Remote Sensing, Vol. 31, 451-461, 1992.

[39] Meneghini, R. and K. Nakamura, Range profiling of the rain rate by airborne weather radar, *Remote Sens. Environ.*, Vol. 31, 193-209, 1990.

[40] Meneghini, R., J. R. Wang, H. Kumagai, and T. Ighuchi, Description of a radar/radiometer method and its application to airborne measurements over stratiform rain, IGARSS'94, JPL, Pansadan, CA, 1773-1775, 1994.

[41] Mugnai, A., and E. A. Smith, Radiative teansfer to space through a precipitating cloud at multiple microwave frequencies. Part I: Model description, J. Appl. Meteor., Vol. 27, 1055-1073, 1988.

[42] Pak, K., L. Tsang, L. Li, C. H. Chan, Combined random rough surface and volume scattering based on Monte Carlo simulations of solutions of Maxwell's equations, Radio Sci., Vol. 28, No. 3, 331-338, 1993.

[43] Petty, G. W., K. B. Katsaros, The response of SSM/I to the marine environment. part I: an analytic model for the atmospheric component of observed brightness temperatures, J. Atmos. Oceanic Technol., 9, 746-761, 1992.

[44] Petty,G.W.,1990: On the response of the Special Sensor Microwave/Imager to the marine environment-Implications for atmospheric parametersity retrievals. Ph.D dissertations, University of washington, 291PP.[Available from University Microfilm, 305 N.Zeeb Rd., Ann Arbor, MI 48106].

[45] Politovich, M. K., B. B. Stankov, and B. E. Martner, Use of combined remote sensors for determination of aircraft icing altitudes, 11th Intentional conference on cloud and precipitation, Montreal, Canada, Aug. 17-21, 1992.

[46] Politovich, M.K., Aircraft icing caused by large Supercooled Droplets, J. Climate Appl. Meteor., Vol.28, No.9, 856-868,1989.

[47] Pruppacher, H.R., The microstructure of atmospheric clouds and precipitation. In clouds, their formation, optical properties and effects (P. V. Hobbs and A. Deepak, eds). Academic Press, New York, 1981.

[48] Pruppacher, H.R. and J.D. Klett, Microphysics of clouds and precipitation, D. Reidel Publishing Comapny, 1980.

[49] Rassmussen, R. M., M. K. Politovich, J. Marwitz, W. Sand, J. McGinely, J. Smart, R. Pielke, S. Rutedge, D. Wesley, G. Stossmeister, B. Stankov, and D. Burrows, Winter Icing and Strom Project, Bull. Amer. Meteor. Soc. vol. 73, no. 7, 951-974, 1992.

[50] Rasmussen, R. and M. Politovich, Winter icing and storms project (WISP): scientific overview, National Center for Atmospheric Research report, June 1990.

[51] Ray, P. S., Broadband complex refractive indices of ice and water, Applied Optics, vol 11, p 1836, 1972.

[52] Rumelhart, D. E., G. E. Hinton, and R. J. Williams, Learning internal representations by error propagation, in *Parallel Distributed Processing (PDP): Exploration in Microstructure of Coginition,* Vol. 1, Cambridge, MA: M.I.T. Press, ch. 8, 318-361, 1986.

[53] Sauvageot, H. and J. Omar, Radar reflectivity of cumulus, J. Atmos. Ocean. Tech. Vol. 4, 264-272, 1987.

[54] Schmidlin, F.J., Radiosonde measurements: How accurate are they? How accurate must they be? in Prepr. 8th symp. on Meteorological Observations and Instrumentation, 93-97, 1990.

[55] Smith, E. A., A. Mugnai, H. J. Cooper, G. Tripoli, and X. Xiang, Foundations for statistical-physical precipitation retrieval from passive microwave satellite measurements. Part 1: Brightness-temperature properties of a time-dependent cloud-radiation model, J. Appl. Meteorol., Vol. 31, 506-531, 1992.

[56] Smith, P. L., Equivalent radar reflectivity factors for snow and ice particles, J. Climate ans Applied Meteorology, Vol 23, 1258-1260, 1984.

[57] Staelin, D. H., Measurements and interpretation of the microwave spectrum of the terrestrial atmosphere near 1-centimeter wavelength, J. Geophys. Res., 71, 2857-2881, 1966.

[58] Stankov, B. B., B. E. Martner, J. A. Schroeder, M. K. Politovich, and J. A. Cole, Liquid water and water vapor profiling in multi-layered cloud using combined remote

sensors, 31st Aerospace Science Meeting and Exhibit, Reno, NV, AIAA 93-0395, January 11-14, 1993.

[59] Stankov, B. B., B. E. Martner, M. K. Politovich, Moisture profiling of the cloudy winter atmosphere using combined remote sensors, submitted to J. Atmos. Oceanic Technol., May, 1994.

[60] Stossmeister, G., Winter icing and storms project 1994: operations plan, National Center for Atmospheric Research report, February 1994.

[61] Tsang, L., Z. Chen, Seho Oh, R. J. Marks II, and A. T. C. Chang, Inversion of snow parameters from passive microwave remote sensing measurements by a neural network trained with a multiple scattering model, IEEE Trans. on Geoscience and Remote Sensing, vol. 30, no. 5, 1015-1024, 1992.

[62] Tsang, L., C. H. Chan, J. A. Kong, and J. Joseph, Polarimetric signature of a canopy of dielectric cylinders based on first and second order vector radiative transfer theory, J. Electromagn. Waves Appl., Vol. 6 No. 1, 19-51, 1992.

[63] Tsang, L., Polarimetric passive microwave remote sensing of random discrete scatterers and rough surfaces, J. Electromagn. Waves Appl., vol. 5, no. 4, 41-57, 1991.

[64] Tsang, L. and K. H. Ding, Polarimetric signature of a layer of random nonspherical discrete scatterers overlying a homogeneous half-space based on first- and second-order vector radiative transfer theory, IEEE Trans. on Geoscience and Remote Sensing, Vol. 29, No. 2, 242-253, 1991.

[65] Tsang, L., J. A. Kong, and R. T. Shin, Theory of microwave remote sensing, New York: John Wiley & Sons, 1985.

[66] Tsang, L., Thermal emission of nonspherical particles, Radio Sci., vol. 19, no. 4, 966-974, 1984.

[67] Ulbrich, C. W., National variations in the analytical form of the raindrop size distribution, *J. Atmos. Oceanic Tech.*, Vol. 22, 1764-1755, 1983.

[68] Vivekanandan, J., V. N. Bringim M. Hagen, and P. Meischner, Polarimetric radar studies of atmospheric ice particles, IEEE Trans. on Geoscience and Remote Sensing, Vol. 32, No. 1, 1-10, 1994.

[69] Vivekanandan, J., J. Turk, and V. N. Bringi, Comparison of precipition measurements by the advanced microwave precipitation radiometer and multiparameter radar, IEEE Trans. Geoscience Remote Sensing, Vol. 31, 860-870, 1993.

[70] Vivekanandan, J., J. Turk, and V. N. Bringi, Ice water Path estimation and characterization using passive microwave radiometry, J. Appl. Meteor., Vol. 30, No. 10, 1407-1421, 1991.

[71] Vivekanandan, J., J. Turk, G. L. stephens, and V. N. Bringi, Microwave radiative transfer using combined multiparameter radar and radiometer measurements during COHMEX, J. Applied Meteorology, Vol. 29, No. 7, 561-585, 1990.

[72] Waterman, P. C., New formulations of acoustic scattering, J. Acoust. Soc. Am., Vol. 45, 1417, 1996.

[73] Wei, C., H. G. Leighton, and R. R. Rogers, A comparison of several radiometric methods of deducing path-integrated cloud liquid water, J. Atmos. Oceanic Technol., 6, 1001-1012, 1989.

[74] Wentz, F.J., A model function for Ocean microwave brightness temperatures, J. Geophys. Res. Vol.88, 1892-1908,1983

[75] Westwater, E. R., Ground-based microwave remote sensing of meteorological variables, Ch. 4 of Atmospheric Remote Sensing by Microwave Radiometry, edited by M. A. Janssen, New York: John Wiley & Sons, 1993.

[76] Westwater, E. R., F. O. Guiraud, Ground-based microwave radiometric retrieval of preciptable water vapor in the presence of clouds with high liquid conten, Radio Sci., 15, 947-957, 1980.

[77] Westwater, E. R., 1978, The accuracy of water vapor and cloud liquid determination by dual-frequency ground-based microwave radiometry, Radio Sci., 13, 667-685, 1978.

[78] Zhao, H., Analysis of tropical cyclones using microwave data from the Special Sensor Microwave/Imager, M.S. thesis, University of Washington, 1994.

Appendix A

NUMERICAL SIMULATION OF CONICAL DIFFRACTION OF TAPERED ELECTROMAGNETIC WAVES FROM RANDOM ROUGH SURFACES AND APPLICATIONS TO PASSIVE REMOTE SENSING(ABSTRACT)

Li Li, Chi H. Chan, and Leung Tsang

Department of Electrical Engineering, FT-10
University of Washington, Seattle, WA 98195

Radio Sci., Vol. 29, No. 3, 587-598, 1994

ABSTRACT

A new tapered wave integral equation method was derived to simulate the conical diffraction of electromagnetic waves from rough surfaces. Both the full matrix inversion and the banded matrix iterative approaches are developed. By using the principle of reciprocity and energy conservation, all four Stokes parameters are calculated for polarimetric passive remote sensing of rough surfaces. We show in this paper that for a moderately rough surface, the third Stokes parameter can be as high as $\pm 20° K$. The tapered wave integral equation approach can deal with a rough surface with a large slope. The new method presented in this paper is compared with the previously published plane wave integral equation method and the extended boundary condition method. Very good agreement is obtained. Unlike the plane wave integral equation method and the extended boundary condition method, the tapered wave integral equation method does not have the kinks imposed by Floquet models and it requires a shorter surface length in most applications.

Appendix B

MONTE CARLO SIMULATIONS AND BACKSCATTERING ENHANCEMENT OF RANDOM METALLIC ROUGH SURFACES AT OPTICAL FREQUENCIES (ABSTRACT)

L. Li, C.H. Chan, L. Tsang, K. Pak and P. Phu
Electromagnetics and Remote Sensing Laboratory
Department of Electrical Engineering, FT-10
University of Washington, Seattle, WA 98195

S.H. Lou
Jet Propulsion Laboratory
4800 Oak Grove Drive, Pasadena, CA 91109

J. Electromagn. Wave Appl., Vol. 8, No. 3, 277-293, 1994

ABSTRACT

he finite element method of Monte Carlo simulations of random rough surface scattering is extended to plane and tapered wave scattering from random metallic surfaces at optical frequencies. The backscattering enhancement associated with these rough surfaces is studied for both TE and TM incident waves. Numerical results of the finite element method are presented and compared with those of the tapered wave integral equation method. In all the cases considered, both the TE and TM incident waves show backscattering enhancement. The lossy surfaces scatter more power for TE incident waves than those of TM due to the TM surface waves. No TE surface wave is supported by rough surfaces simulated in this paper.

BIOGRAPHICAL NOTE

Li Li was born in Henan, China. He received the B.S. degrees in Radio Physics from the Wuhan University, Wuhan, China, in 1984, and the M.S. degree in electrical engineering from Beijing University of Posts and Telecommunications, Beijing, in 1987. From 1987 to 1991, he worked in the area of microwave remote sensing for the *Center for Space Science and Applied Research, Chinese Academy of Sciences*, China.

In June 1991, he attended the University of Washington to further his graduate study. His current research interests include microwave remote sensing of atmospheric components and boundaries, wave propagation and scattering, and neural networks. He has the following papers and presentations, listed chronologically, to his credit:

Journal Articles

- L. Li, J. Vivekanandan, C. Chan, and L. Tsang "Microwave radiometer technique to retrieve vapor, liquid and ice, Part I: Development of Neural Network based physical inversion method. submitted to *IEEE Trans. on Geoscience and Remote Sensing.*

- L. Li, C. H. Chan, L. Tsang "Numerical simulation of conical diffraction of tapered electromagnetic waves from random rough surfaces and applications to passive remote sensing," *Radio Sci., Vol. 29, No. 3, 587-598, 1994.*

- L. Li, C. H. Chan, L. Tsang, K. Pak, P. Phu, S. H. Lou "Monte carlo simulation and backscattering enhancement of random metallic rough surface at optical frequencies," *J. Electromagn. Wave Appl., Vol. 8, No. 3, 277-293, 1994.*

- K. Pak, L. Tsang, L. Li, C. H. Chan "Combined random rough surface and volume scattering based on Monte Carlo simulations of solutions of Maxwell's equations," *Radio Sci., Vol. 28, No. 3, 331-338, 1993.*

- L. Li, Y. Yang, R. L. Li "Input impedance of microstrip antenna with thick multilayer substrate, *J. Electronics (China), Vol. 7, No. 3, 1990.*

- L. Li, Y. Yang "Analysis of circular microstrip disk antenna with an air gap using vector Hankel transform," *J. Beijing University of Posts and Telecommunications, Vol. 11, No. 1, 1988.*

Conference Presentations

- L. Li, J. Vivekanandan, C. H. Chan, and L. Tsang "Studies on Passive Remote Sensing of Ice and Liquid Water Paths," IGARSS'94, Aug. 8-12, JPL, Pasadena, California, 1994.

- L. Tsang, C. H. Chan, L. Li, K. Pak and H. Sangani "Monte Carlo simulations of large-scale random rough surface scattering based on a sparse matrix iterative approach," Progress In Electromagnetics Research Symposium(PIERS), JPL, Pasadena, California, 1993.

- C. H. Chan, L. Li, L. Tsang "A banded matrix iteration approach to Monte Carlo simulation of large-scale random rough surface scattering: penetrable case," The 9th Annual Review of Progress in Applied Computational Electromagnetics, Monterey, California, 1993.

- L. Li, C. H. Chan, L. Tsang, K. Pak, S. H. Lou "The application of finite element method to scattering of plane wave by random metallic rough surface at optical frequencies," IEEE APS/URSI/NEM International Joint Symposia, Chicago, IL 1992.

- C. H. Chan, J. T. Elson, L. Li, L. Tsang "A conformal finite-difference time-domain approach for Monte Carlo simulation of random rough surface scattering," IEEE APS/URSI/NEM International Joint Symposia, Chicago, IL 1992.

- L. Li, Y. Yang "Study on multilayer microstrip antenna," IEEE AP-S International Symposium, Syracuse, NY, 1988.